Spring 2014

Turbo equalization for multiple-input multiple-output (MIMO) wireless communication systems

Longbao Wang

Department: Electrical and Computer Engineering

TURBO EQUALIZATION FOR MULTIPLE-INPUT MULTIPLE-OUTPUT (MIMO) WIRELESS COMMUNICATION SYSTEMS

by

LONGBAO WANG

A DISSERTATION

Presented to the Faculty of the Graduate School of the

MISSOURI UNIVERSITY OF SCIENCE AND TECHNOLOGY

In Partial Fulfillment of the Requirements for the Degree

DOCTOR OF PHILOSOPHY

in

ELECTRICAL ENGINEERING

2014

Approved by

Chengshan Xiao, Advisor
Yiyu Shi
Kurt Kosbar
Steve Grant
Xiaoqing (Frank) Liu

PUBLICATION DISSERTATION OPTION

This dissertation consists of the following five published or submitted papers, formatted in the style used by the Missouri University of Science and Technology, listed as follows:

Paper I, L. Wang, J. Tao, C. Xiao and T. C. Yang, "Low-complexity turbo detection for single-carrier low-density parity-check-coded multiple-input multiple-output underwater acoustic communications," has been published in Wireless Communications and Mobile Computing., vol. 13, pp 439-450, March 2013. (pages 8-36)

Paper II, L. Wang, J. Tao and Y. R. Zheng, "Frequency-Domain Turbo Detection for No-CP Single-Carrier MIMO Underwater Acoustic Communications," has been published in MTS/IEEE OCEANS, Kona, Hawaii, Sep. 2011. (pages 37-53)

Paper III, L. Wang, J. Tao and Y. R. Zheng, "Single-carrier frequency-domain turbo equalization without cyclic prefix or zero padding for underwater acoustic communications," has been published in J. Acoustic Society of America , vol. 132, pp. 3809-3817, 2012. (pages 54-81)

Paper IV, J. Wu, L. Wang and C. Xiao, "Low Complexity Soft-Interference Cancelation Turbo Equalization for MIMO systems with Multilevel Modulations," has been published in Proc. IEEE GLOBECOM, Atlanta, GA, Dec. 2013. (pages 82-102)

Paper V, J. Wu, L. Wang and C. Xiao, "Low Complexity Soft-Interference Cancelation Turbo Equalization for MIMO systems with Multilevel Modulations," submitted to IEEE Trans. Veh. Technol., 2013. (pages 103-138)

ABSTRACT

This dissertation investigates both of the frequency domain and time domain turbo equalization with multiple-input multiple-output (MIMO) fading channels for radio frequency and underwater acoustic communications. First, a low complexity frequency domain turbo equalization (FDTE) is proposed for the MIMO systems with zero padding (ZP) or cyclic prefix (CP) inserted between the transmitted data blocks and its performance is tested on the real-world UWA communications experiments.

Second, as high speed communication system requires efficient bandwidth usage and power consumption, CP or ZP is not transmitted as auxiliary information. An inter-block interference cancelation and CP reconstruction algorithm is developed to re-arrange the channel matrix into a block diagonal one. This improvement makes the FDTE effectively detects the continuous data stream from the high speed UWA communications and its performance has been verified by processing data collected from the UWA communications experiment.

Finally, a low complexity soft interference cancelation (SIC) time domain turbo equalizer for MIMO systems with high level modulation is proposed. Compared with the conventional linear or nonlinear turbo equalizers, the proposed SIC turbo equalizer can theoretically reach the bound set up by the ideal match filter and its bit error rate (BER) performance from Monte Carlo simulation achieves a lower error floor as well as a more rapid convergence speed.

ACKNOWLEDGMENTS

I would like first to express my deepest gratitude to my advisor, Dr. Changshan Xiao, for his encouragement, support and guidance through the journey of my PhD study. I thank him for inspiring me the interests of scientific research and encouraging and teaching me independent thinking.

Secondly, I would like to thank Dr. Yahong Rosa Zheng for being a valuable source of ideas and motivation as well. Dr. Yahong Rosa Zheng has provided helpful advices to me to overcome the difficulty both in my course work and my research.

I would also like to thank the members of my advisory committee, including Dr. Yiyu Shi, Steve Grant, Kurt Kosbar and Xiaoqing Liu. They have provided, with kindness, their insight and suggestions, which are precious to me.

In addition, I would like to acknowledge both Dr. Jun Tao and Dr. Jinxian Wu, co-authors of my publications, for their guidance and help in the achievement of the work.

I also want to express my sincere gratitude to past and present members in the research lab. I thank for their kindly support and friendship.

Finally I would like to express my eternal gratitude to my parents and parents-in-law for their everlasting love and support. I would also like to offer my extraordinary thanks to my wife, Fan(Ann) Ke, for her generous love, constant encouragement, and full support. I dedicate this dissertation to my 10-month baby, who is the joy of our lives.

TABLE OF CONTENTS

LIST OF ILLUSTRATIONS

LIST OF TABLES

1 INTRODUCTION

1.1 BACKGROUND AND PROBLEM STATEMENT

Increasing the transmission rate and reliability is always one of the basic objects for the development of the wireless communication techniques. Recent studies have found that multiple-input multiple-output (MIMO) systems can achieve a significant capacity gain [1] without additional power consumption at the transmitter side. The MIMO system deploys multiple antenna elements at both the transmitter and receiver sides so that the communication capacity grows linearly with the minimum number of transmit and receive antennas. This significant improvement can be obtained by spatial multiplexing and diversity coding, thus improving the transmission rate and reliability of the wireless communication system.

In practical wireless communication systems, the transmitted signal is usually severely corrupted by the inter-symbol interference (ISI), which is introduced by the frequency selective fading wireless channels. For the MIMO systems, the transmit/receive antenna arrays also give rise to the reflection and scattering of the propagation radio wave, thus introducing other kind of interference whereas the single-input single-output (SISO) system does not have. Secondly, the time-varying nature or time selectivity, introduced by the relative movement of the transmitter and receiver, of the wireless channel can lead to Doppler shift, which imposes much difficulty on channel tracking. Also the carrier frequency offset (CFO), which is due to the mismatch of the local oscillator or instant Doppler shift, can degrade the performance of coherent receiver. Last, the co-channel interference (CCI) resulting uniquely from the multiple paths between the antenna arrays or space selectivity can further increase the difficulty in transceiver design to achieve capacity gain as well as accurate detection.

To overcome the unreliability transmission over the frequency-selective, time-selective and space-selective channels in MIMO communication systems, forward error correction coding (channel coding) is used at the transmitter by adding redundant bits. And the redundancy enables the receiver to detect a limited number of bits and may correct them without retransmission. Then it is the task of receiver to detect the transmitted data sequence by exploiting the structure of the transmitted symbol constellation and the coding scheme. And functions of exploiting the structure of symbol constellation and coding scheme are considered as equalization and decoding.

In a typical receiver, the equalizer first mitigates the ISI based on the channel state information. Utilizing the estimated transmitted symbols and the known coding scheme, the decoder extracts the information and makes hard decisions of each transmitted bits. With the advantage of low computation complexity, the equalizer is usually designed as finite impulse response (FIR) filter, which is considered as linear equalizer (LE) [2, 3]. Also, the previous estimated symbols can be used to further mitigate the ISI and this is considered as decision feedback equalizer (DFE) [2, 3]. The derivation of the coefficients of the LE or DFE is based on different optimization criteria, such as zero forcing (ZF) or MMSE criteria. Optimal equalization for recovering the transmitted symbols is designed based on the maximum likelihood (ML) estimation, which turns into maximum *a posterior* probability (MAP) estimation in presence of *a priori* information about the transmitted data. We refer to this method as MAP/ML equalization. The output of the equalizer is passed to the decoder and the hard decision will be made to each transmitted bit within the method of conventional one-time equalization receiver. In order to further reduce the BER, a number of iterative receiver algorithms have been proposed to achieve the near-optimal performance by repeating the equalization and decoding operation on the same group of received data, using the feedback information from the decoder to implement the equalization. This iterative equalization is referred as turbo equalization and was first

introduced in [4]. With the increase of the reliability of the soft information by the iterative equalization and decoding, turbo equalization can achieve significant performance gains over one-time equalization [5, 6, 7]. All these operation are implemented in time domain.

On the other hand, even with linear processing in the equalization part, the receiver suffers from high computational complexity and slow convergence if the channel length is long, because the complexity of the time domain equalization grows quadratically with the number of antenna elements and the number of channel taps. In high data-rate communication systems, the channel can span on the order of ten or even hundred of symbol duration. And underwater acoustic (UWA) channels impose more challenges than radio frequency environment with its excessive delay spread, frequency-dependent attenuation and significant time-varying Doppler shift. Hence frequency domain method has to be used to overcome this computational complexity. Orthogonal frequency division multiplexing (OFDM) and single carrier with frequency domain equalizer (SC-FDE) are considered as the two main frequency domain methods for modern high data rate wireless communications. The major difference between these two methods is the replacement of the inverse fast Fourier transform (IFFT): IFFT is finished at transmitter in OFDM while at the receiver in SC-FDE.

1.2 PROBLEM STATEMENT

Specifically, this dissertation investigates technical challenges associated with frequency domain turbo equalization (FDTE) on and its practical applications on UWA MIMO communications. In the single-carrier (SC) MIMO communication systems, the data bits after encoding are mapped into symbols based on the specified modulation type. In some system, these modulated symbols will be grouped into blocks with cyclic prefix (CPs) or zero padding (ZPs) inserted between adjacent blocks. So that at the receiver, CPs are removed or overlap-add is performed with ZPs used in one block, and fast Fourier Transform (FFT) is calculated to convert the

time-domain signal to frequency domain. So that the equalization can be carried out on each frequency tone, and finally the equalized frequency domain signal is transformed to time domain with IFFT. Whereas in other systems, no CPs or ZPs are utilized in order to gain high spectrum usage. And this will introduce the inter-block interference which can be removed with CPs or ZPs employed.

1. How to extend the FDTE of SC SISO system to the MIMO system is the key step to utilize the FDTE to the real world data processing. In the UWA communication experiments, antenna array are deployed both at the transmitter and receiver. For SISO system, the system can be described as $Y_k = H_k X_k + N_k$, where X_k and Y_k are the scalar representing the kth frequency tone of the transmitted/received signals respectively, and H_k is the kth frequency tone of the frequency selective channel. While for the MIMO system, the superposition of signal from different transmitting antennas will make the received the signal in frequency domain the summation of the transmitted signal with corresponding weights being the channel responses at the same frequency tone. So how to exploit the transmission diversity of the MIMO system to separate the signals from different antennas within the FDTE methods is to be solved.

2. The appliance of the FDE method mostly requires the CPs or ZPs are inserted between adjacent blocks at the transmitter. In this way, the inter-block interference can be removed by cutting of the CPs segment at the receiver, or overlap-add operation with ZPs used. Either way will make the channel matrix in time domain representation into a circulant matrix and it can be transformed to a block diagonal matrix. So the system can be approximated as uncorrelated transmissions of different frequency tone signals, which can significantly reduce the detection complexity by using the FDE. However, the appended CPs or ZPs do not carry any useful information, thus bringing down the spectrum efficiency especially for the valuable available bandwidth for UWA communications. If

FDTE can be applied within the transmission system without adding CPs or ZPs, then we can improve the performance of detection without sacrificing the bandwidth to transmit auxiliary information.

3. FDTE is used to combat the ISI and CCI for the real world data received from the UWA communications employing the estimated channels. For MIMO architecture, all the sub-channels corresponding to all transmitter and receiver pairs have to be estimated. Pilots were inserted in the transmitted symbol streams to assist the channel estimation. However for the rapid time-varying UWA channels, channel tracking purely based on the inserted pilots is insufficient. How to effect and promptly track the channel is another important information before we process the data using FDTE.

The developed FDTE methods along with the channel estimation are applied to UWA communication systems. Underwater acoustic channels are characterized by excessive delay spread, frequency-dependent attenuation and significant time-varying Doppler shift. The attenuation of the sound wave traveling through water is proportional to the square of frequency, resulting in a much lower carrier frequency, smaller communication distance and narrower bandwidth to support the transmission than the RF system. In medium range UWA communication system, which means the transmission distance is between as 1 and 10 kilometers, the available bandwidth is on the level of several KHz. The dynamic movement of the water media leads to rapid time varying Doppler shift, and the ratio of Doppler shift to the carrier frequency is on the order of 10^{-4} to 10^{-3}, much higher comparing with that of the RF system which is on the order of $10^{-7} \sim 10^{-9}$. These features of UWA channel make it one of the worst physical links for communications and obtaining reliable MIMO UWA communications has been a challenging topic for decades. The proposed FDTE

methods and channel estimation are used at the receiver to achieve highly reliable UWA communications.

1.3 SUMMARY OF CONTRIBUTIONS

This dissertation consists of three journal publications and a couple of conference papers as detailed in the publication list. My contributions that are published or under review are:

1. *Low-Complexity Turbo Detection for Single-Carrier MIMO Underwater Acoustic Communications*: In the turbo equalization, the extrinsic information in the form of log-likelihood ratio (LLR) is exchanged between the equalizer and decoder via interleaver or de-interleaver. And the calculation of the LLR is prohibitively complex if following the closed form expression. In this paper an approximation method is proposed to calculate the LLR from the equalizer, which significantly reduce the computation complexity especially for the high level modulation. The proposed FDTE is applied to process real-world data collected in two different undersea trials: WHOI09 and ACOMM09. The BER output of the FDTE decreases as the iteration increase and converges within only a few iterations. Experimental results show that the FDTE can achieve robust detection combining with the LDPC decoding scheme for MIMO UWA communication systems with different modulations and different symbol rate, at different transmission ranges.

2. *Single-carrier frequency-domain turbo equalization without cyclic prefix or zero padding for underwater acoustic communications*: In order to achieve high efficient spectrum usage for the UWA communications, no CPs or ZPs are inserted to split a continuous symbol stream into blocks. The received data stream is divided into consecutive blocks with size determined according to the channel condition. The inter-block-interference (IBI) cancelation and CP reconstruction are applied on each partitioned block, so that the channel matrix is block diagonalized in the frequency

domain and frequency-domain equalization can be operated for symbol detection at a very low complexity. The IBI is removed from the current block by using the estimated channel and the detected symbols from a previous block. The CP reconstruction is obtained by utilizing the soft symbol estimation from previous iteration. In the first iteration, the frequency-domain equalization is performed in an overlapped way with a bearable loss in detection efficiency and performance. Also during the processing of the real-world data, it shows that the constellation of the equalized symbols is rotated due to CFO. A novel and robust method is proposed to estimate the rotated phases and remove the phase bias for the equalized symbol. The experiment results of ACOMM09 has shown that the proposed FDTE can support high data-rate UWA communications with low bit error rate, even without CPs or ZPs inserted.

3. *Low Complexity Soft-Interference cancellation Turbo Equalization for MIMO Systems with Multilevel Modulations* : Although the soft decision feedback turbo equalization (SDFE) converges faster and has low SNR threshold, it cannot reach the bound of matched filter even after large number of iterations. By adding a anti-causal feedback filter to the SDFE structure, Soft-interference cancelation equalization can further remove the residual interference caused by the symbols transmitted after the symbol under detection. The performance of the proposed SICE is verified through both extrinsic information transfer chart (EXIT) analysis and computer simulations. The analytical and simulation results demonstrated that the inclusion of the anti-causal soft decision during SICE is critical to the system performance. The EXIT chart analysis indicates the SICE approaches the ideal matched filter bound as the iteration progresses.

PAPER

I. Low-Complexity Turbo Detection for Single-Carrier MIMO Underwater Acoustic Communications

Longbao Wang, Jun Tao, Chengshan Xiao *Fellow, IEEE* and T. C. Yang,

ABSTRACT—A low-complexity turbo detection scheme is proposed for single-carrier multiple-input multiple-output (MIMO) underwater acoustic (UWA) communications, which employ low-density parity-checking (LDPC) channel coding. The low complexity of the proposed detection algorithm is achieved in two aspects: first, the frequency-domain equalization technique is adopted, and it maintains a low complexity irrespective of the highly-dispersive UWA channels; second, the computation of the soft equalizer output, in the form of extrinsic log-likelihood ratio (LLR), is performed with an approximating method, which further reduces the complexity. Moreover, attributed to the near-capacity LDPC decoding, the turbo detection converges within only a few iterations. The proposed turbo detection scheme has been used for processing real-world data collected in two different undersea trials: WHOI09 and ACOMM09. Experimental results show that it provides robust detection for MIMO UWA communications with different modulations and different symbol rates, at different transmission ranges.

Keywords: Turbo detection, frequency-domain equalization, underwater acoustic communication

1 INTRODUCTION

Underwater acoustic (UWA) communication is very challenging due to the severe condition of the UWA channel: first, the length of the equivalent discrete-time channel is extremely long due to the highly-dispersive channel impulse response (CIR); second, the time variation of the UWA channel is very fast due to the rapid dynamic variation of the oceans especially in shallow water; third, the Doppler effect of the underwater channel is significantly large due to the relatively low propagation speed of sound. Besides, the achievable transmission rate in UWA communications is usually low because of the limited available bandwidth.

Coherent detection using conventional equalization methods have been proposed in the literature [1]– [12]. With the advent of turbo equalization [6], [7], turbo detection for UWA communications is receiving more attention recently [6]– [9]. Compared with conventional one-time equalization, turbo equalization has a much more powerful detection capability, attributed to the iterative extrinsic soft information exchanges between a soft-decision equalizer and a soft-decision decoder. In [6], the soft-decision decision-feedback equalizer (DFE) together with the turbo decoder, has been applied to UWA communication. In [8], the turbo linear equalizer (LE) was proposed for long-term UWA communication testing. The convolutional decoder implemented with the classic BCJR algorithm [19], has been adopted. In [13], turbo detection using block decision-feedback equalization (BDFE) has also been proposed for single-carrier UWA communications. The BDFE leads to a better detection performance compared with the conventional DFE. Iterative decoding and turbo detection for orthogonal frequency-division multiplexing (OFDM) UWA systems has also been proposed in [11] and [9].

The equalization methods used in [6] and [8] are designed in the time domain, and the detection complexity increases with the channel length. On the other hand,

the equalization for OFDM systems [9] is performed in the frequency domain, and it has the advantage of low complexity. However, OFDM systems are very sensitive to the carrier frequency offset (CFO), thus it is very challenging to achieve reliable signal detection in UWA communication due to its significant Doppler effect. To avoid the drawback of OFDM while still achieve the advantage of low-complexity equalization, single-carrier frequency-domain equalizer (SC-FDE) has been proposed in [14] and [15].

In this paper, a low-complexity turbo detection scheme is proposed for single-carrier MIMO UWA communications using low-density parity-check (LDPC) channel coding. The proposed turbo detector has two main advantages. First, it has low equalization complexity even with the highly-dispersive UWA channels, by adopting the SC-FDE technique; Second, it has a fast convergence speed, which is enabled by the near-capability LDPC decoding [16]. The proposed detection scheme has been tested by extensive undersea trial data collected in two medium-range undersea experiments named WHOI09 and ACOMM09, respectively. The WHOI09 experiment was conducted at Buzzard's Bay, MA, in December 2009. The transmission rate was 25 kilo-symbols per second (ksps) per transducer, at a transmission distance of $1 \sim 2$ km. The ACOMM09 experiment was launched at the coastline of New Jersey in May 2009, with a transmission rate of 5 ksps per transducer at a transmission distance of $2 \sim 3$ km. Experimental results show that in both experiments, error-free detection can be achieved for two-transducer MIMO transmissions with a QPSK modulation. With an 8PSK modulation, the WHOI09 experiment achieves a bit error rate (BER) in the order of 10^{-4}, while error-free detection can still be achieved for the ACOMM09 experiment. With a 16QAM modulation, the achievable BERs for the two experiments are in the order of 10^{-3} and 10^{-5}, respectively.

The rest of this paper is organized as follows. In Section 2, the system model for a single-carrier MIMO UWA communication is described. The proposed low-complexity turbo detection scheme is presented in Section 3, and the experimental results are presented in Section 4. Finally, conclusions are drawn in Section 5.

Notations: Throughout this paper, $(\cdot)^T$ and $(\cdot)^H$ denote the transpose and the Hermitian, respectively. $\mathbb{E}(\cdot)$ and $\mathrm{cov}(\cdot)$ represent the expectation and covariance operations. The $\mathbf{I}_j$ is an identity matrix of size j, and $\mathbf{0}_{i\times j}$ denotes an $i \times j$ all-zero matrix. A $j \times j$ diagonal matrix with diagonal elements $d_1, d_2, \cdots, d_j$ is represented as $\mathrm{diag}\{d_1, d_2, \cdots, d_j\}$.

2 SYSTEM MODEL

Consider a MIMO UWA communication system with N transducers at the transmitter side and M hydrophones at the receiver side. On the m-th hydrophone, the baseband discrete-time samples can be represented as

$$y_{m,k} = \sum_{n=1}^{N} \sum_{l=0}^{L-1} h_{m,n}(k,l) x_{n,k-l} + v_{m,k} \tag{1}$$

where $x_{n,k}$ is the k-th transmitted symbol from the n-th transducer, $h_{m,n}(k,l)$ is the l-th tap of the subchannel between the n-th transducer and the m-th hydrophone at time k, and $v_{m,k}$ is the zero-mean additive white Gaussian noise with power σ^2. It has been assumed that all subchannels have the same channel length, L.

Block transmission using zero padding [4], is adopted throughout this paper. When the time duration of one block is less than the UWA channel coherence time, the time-varying channel tap $h_{m,n}(k,l)$ can be treated as quasi-static within one transmission block, and the model in (1) can be rewritten as

$$y_{m,k} = \sum_{n=1}^{N} \sum_{l=0}^{L-1} h_{m,n}(l) x_{n,k-l} + v_{m,k} \tag{2}$$

for $k = 1, 2, \cdots, N_b, N_b+1, \cdots, N_b+N_g$, where N_b and N_g are the block size and the zero-padding size, respectively. To avoid inter-block interference, $N_g \geq L-1$ has been adopted.

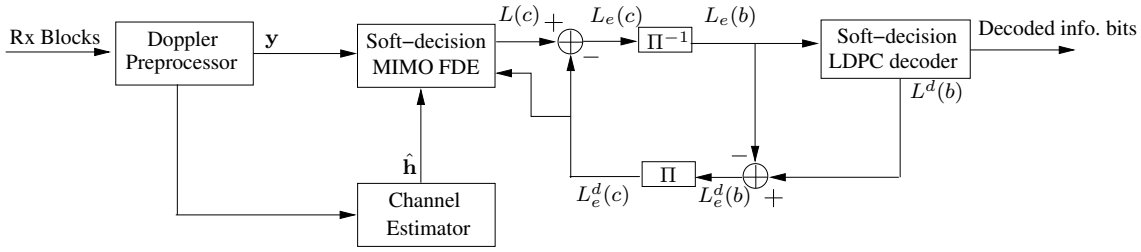

Figure 2.1. Block diagram of the turbo detector.

3 LOW-COMPLEXITY TURBO DETECTION SCHEME

The structure of the proposed turbo detection scheme is shown in Fig. 1.1, where the received signal is first passed through a Doppler preprocessing unit to remove any motion-induced Doppler effect [12]. The preprocessed signal is sent to the soft-decision MIMO FDE and the channel estimator unit. The channel estimator performs minimum mean square error (MMSE) channel estimation in the time domain. Details are referred to [13]. With the estimated channel knowledge, the frequency-domain equalization can be performed and the turbo detection is launched by exchanging extrinsic log-likelihood ratio (LLR) information between the FDE and the LDPC decoder in an iterative way, via the interleaver (Π) and de-interleaver (Π^{-1}). Within each iteration of the detection, the LDPC decoder performs multiple iterations for the decoding. In the rest of the paper, we call the iteration of detection as "detection iteration", and the iteration of LDPC decoding as "decoding iteration", respectively. Once the turbo detection converges, the LDPC decoder will output the hard decisions on the information bits. In the following two subsections, the soft-decision MIMO FDE and the soft-decision LDPC decoder are discussed, respectively.

3.1 SOFT-DECISION MIMO FDE

Define $\mathbf{x}_k = [x_{1,k}, \cdots, x_{N,k}]^T$, $\mathbf{y}_k = [y_{1,k}, \cdots, y_{M,k}]^T$, $\mathbf{v}_k = [v_{1,k}, \cdots, v_{M,k}]^T$ as the transmitted symbol vector, the received sample vector, and the noise vector at time k, respectively. A whole block of received samples can then be denoted as

$$\mathbf{y}^b = [\mathbf{y}_1^T, \cdots, \mathbf{y}_{N_b}^T, \mathbf{y}_{N_b+1}^T, \cdots, \mathbf{y}_{N_b+L-1}^T]^T \tag{3}$$

Performing the overlap-add operation as follows

$$\begin{aligned}\mathbf{y} &= [\mathbf{y}_1^T, \cdots, \mathbf{y}_{L-1}^T, \mathbf{y}_L^T, \cdots, \mathbf{y}_{N_b}^T]^T + \\ &\quad [\mathbf{y}_{N_b+1}^T, \cdots, \mathbf{y}_{N_b+L-1}^T, \mathbf{0}_{M\times 1}^T, \cdots, \mathbf{0}_{M\times 1}^T]^T \end{aligned} \tag{4}$$

we have

$$\mathbf{y} = \mathbf{H}_{td}\mathbf{x} + \mathbf{v} \tag{5}$$

where $\mathbf{x} = [\mathbf{x}_1^T, \mathbf{x}_2^T, \cdots, \mathbf{x}_{N_b}^T]^T$ and

$$\mathbf{H}_{td} = \begin{bmatrix} \mathbf{h}_0 & \mathbf{0} & \cdots & \mathbf{0} & \mathbf{h}_{L-1} & \mathbf{h}_{L-2} & \cdots & \mathbf{h}_1 \\ \mathbf{h}_1 & \mathbf{h}_0 & \mathbf{0} & \cdots & \mathbf{0} & \mathbf{h}_{L-1} & \cdots & \mathbf{h}_2 \\ \vdots & \ddots & \ddots & \ddots & \ddots & \ddots & \ddots & \vdots \\ \mathbf{h}_{L-1} & \mathbf{h}_{L-2} & \cdots & \mathbf{h}_0 & \mathbf{0} & \mathbf{0} & \cdots & \mathbf{0} \\ \mathbf{0} & \mathbf{h}_{L-1} & \cdots & \mathbf{h}_1 & \mathbf{h}_0 & \mathbf{0} & \cdots & \mathbf{0} \\ \vdots & \ddots & \ddots & \ddots & \ddots & \ddots & \ddots & \vdots \\ \mathbf{0} & \cdots & \mathbf{0} & \mathbf{0} & \mathbf{h}_{L-1} & \mathbf{h}_{L-2} & \cdots & \mathbf{h}_0 \end{bmatrix} \tag{6}$$

with $\mathbf{h}_l$ given as

$$\mathbf{h}_l = \begin{bmatrix} h_{1,1}(l) & \cdots & h_{1,N}(l) \\ h_{2,1}(l) & \cdots & h_{2,N}(l) \\ \vdots & \ddots & \vdots \\ h_{M,1}(l) & \cdots & h_{M,N}(l) \end{bmatrix} \tag{7}$$

The subscripts of the all-zero matrices $\mathbf{0}_{M\times N}$ in (6) has been omitted for brevity. Finally, the noise vector $\mathbf{v}$ is defined similar to $\mathbf{y}$ in (4). Due to the overlap-add operation, the variances of the first $M(L-1)$ samples in the noise vector $\mathbf{v}$ become

twice of those of other samples. For the convenience of mathematical analysis, we have assumed all samples in $\mathbf{v}$ have the same variance σ^2. In the real data processing, the difference in noise variances has been considered.

To perform frequency-domain equalization, the time-domain signals $\mathbf{x}$ and $\mathbf{y}$ need to be transformed into the frequency domain. Define two transform matrices

$$\mathbf{F}_x = \begin{bmatrix} \mathbf{F}_x(1,1) & \cdots & \mathbf{F}_x(N_b,1) \\ \mathbf{F}_x(1,2) & \cdots & \mathbf{F}_x(N_b,2) \\ \vdots & \ddots & \vdots \\ \mathbf{F}_x(1,N_b) & \cdots & \mathbf{F}_x(N_b,N_b) \end{bmatrix} \tag{8}$$

$$\mathbf{F}_y = \begin{bmatrix} \mathbf{F}_y(1,1) & \cdots & \mathbf{F}_y(N_b,1) \\ \mathbf{F}_y(1,2) & \cdots & \mathbf{F}_y(N_b,2) \\ \vdots & \ddots & \vdots \\ \mathbf{F}_y(1,N_b) & \cdots & \mathbf{F}_y(N_b,N_b) \end{bmatrix} \tag{9}$$

where $\mathbf{F}_x(l,p) = W_{N_b}^{l,p}\mathbf{I}_N$ and $\mathbf{F}_y(l,p) = W_{N_b}^{l,p}\mathbf{I}_M$, with $W_{N_b}^{l,p} = \frac{1}{\sqrt{N_b}}\exp(-\frac{j2\pi(l-1)(p-1)}{N_b})$ for $l,p = 1,2,\cdots,N_b$. Applying $\mathbf{F}_y$ on both sides of (5), leads to

$$\begin{aligned} \mathbf{Y} &= \mathbf{F}_y\mathbf{H}_{td}\mathbf{F}_x^H\mathbf{F}_x\mathbf{x} + \mathbf{F}_y\mathbf{v} \\ &= \mathbf{H}\mathbf{X} + \mathbf{V} \end{aligned} \tag{10}$$

where $\mathbf{Y} = \mathbf{F}_y\mathbf{y}$, $\mathbf{X} = \mathbf{F}_x\mathbf{x}$, $\mathbf{V} = \mathbf{F}_y\mathbf{v}$, and

$$\begin{aligned} \mathbf{H} &= \mathbf{F}_y\mathbf{H}_{td}\mathbf{F}_x^H \\ &= \mathrm{diag}\{\mathbf{H}_1, \mathbf{H}_2, \cdots, \mathbf{H}_{N_b}\} \end{aligned} \tag{11}$$

The submatrix $\mathbf{H}_k$ has the following form

$$\mathbf{H}_k = \begin{bmatrix} H_{1,1}(k) & \dots & H_{1,N}(k) \\ \vdots & \ddots & \vdots \\ H_{M,1}(k) & \dots & H_{M,N}(k) \end{bmatrix} \tag{12}$$

with $H_{m,n}(k) = \sum_{l=0}^{L-1} h_{m,n}(l)\exp(-\frac{j2\pi l(k-1)}{N_b})$.

The system model in (10) can be decomposed into N_b parallel subsystems as follows

$$\mathbf{Y}_k = \mathbf{H}_k\mathbf{X}_k + \mathbf{V}_k \ \ (k = 1, 2, \cdots, N_b) \tag{13}$$

where $\mathbf{X}_k = [X_{1,k}, X_{2,k}, \dots, X_{N,k}]^T$, $\mathbf{Y}_k = [Y_{1,k}, Y_{2,k}, \dots, Y_{M,k}]^T$, and $\mathbf{V}_k = [V_{1,k}, V_{2,k}, \dots, V_{M,k}]^T$ are subvectors extracted from $\mathbf{X}$, $\mathbf{Y}$ and $\mathbf{V}$, respectively.

For the k-th subsystem, the linear minimum mean square error (LMMSE) estimation of $\mathbf{X}_k$ is given as

$$\hat{\mathbf{X}}_k = \mathbf{A}_k^H(\mathbf{Y}_k - \mathbf{H}_k\bar{\mathbf{X}}_k) + \bar{\mathbf{X}}_k \tag{14}$$

where $\mathbf{A}_k^H$ is the equalizer matrix, and $\bar{\mathbf{X}}_k$ is the *a priori* mean of $\mathbf{X}_k$. The computation of $\mathbf{A}_k^H$ and $\bar{\mathbf{X}}_k$ requires the symbol *a priori* mean and variance, which are defined as follows

$$\bar{x}_{n,k} = \sum_{\alpha\in\mathcal{S}} \alpha \cdot P(x_{n,k} = \alpha) \tag{15}$$

$$\varrho_{n,k}^2 = \sum_{\alpha\in\mathcal{S}} |\alpha - \bar{x}_{n,k}|^2 P(x_{n,k} = \alpha) \tag{16}$$

where $\mathcal{S}$ is the constellation set of size 2^Q. The probability, $P(x_{n,k}=\alpha)$, is calculated from the *a priori* LLRs, $\{L_a(c_{n,k}^j)\}_{j=1}^Q$, of $x_{n,k}$'s demapping bits, $\{c_{n,k}^j\}_{j=1}^Q$, as follows

$$P(x_{n,k}=\alpha)=\prod_{j=1}^{Q}\frac{1+s_j\cdot\tanh(L_a(c_{n,k}^j))}{2} \tag{17}$$

where

$$s_j=\begin{cases}+1; & a^j=0\\ -1; & a^j=1\end{cases}$$

with $\{a^j\}_{j=1}^Q$ being the demapping bits of the symbol α. The function $\tanh(x)$ denotes hyperbolic tangent. The *a priori* LLR, $L_a(c_{n,k}^j)$, at the input of the FDE is equal to, $L_e^d(c_{n,k}^j)$, as shown in Fig. 1.1. In the first detection iteration, there is no *a priori* information available thus the bit LLR is set as $L_a(c_{n,k}^j)=0$.

Let $\bar{\mathbf{x}}=[\bar{x}_{1,1},\cdots,\bar{x}_{N,1},\cdots,\bar{x}_{1,N_b},\cdots,\bar{x}_{N,N_b}]^T$, then we have $\bar{\mathbf{X}}=\mathbf{F}_x\bar{\mathbf{x}}$ from which $\bar{\mathbf{X}}_k$ can be extracted. The equalizer matrix $\mathbf{A}_k$ is solved as

$$\begin{aligned}\mathbf{A}_k &= \mathrm{cov}(\mathbf{Y}_k,\mathbf{Y}_k)^{-1}\mathrm{cov}(\mathbf{Y}_k,\mathbf{X}_k)\\ &= (\mathbf{H}_k\bar{\mathbf{\Psi}}\mathbf{H}_k^H+\sigma^2\mathbf{I}_M)^{-1}\mathbf{H}_k\bar{\mathbf{\Psi}}\end{aligned} \tag{18}$$

where $\bar{\mathbf{\Psi}}=\mathrm{diag}\{\bar{\varrho}_1^2,\cdots,\bar{\varrho}_N^2\}$ with $\bar{\varrho}_n^2=\frac{1}{N_b}\sum_{k=1}^{N_b}\varrho_{n,k}^2$.

The computation of the equalizer matrix $\mathbf{A}_k$ in (18) only requires the inversion of a small square matrix of size M. For the N_b subsystems, the incurred complexity is in the order of $\mathcal{O}(N_bM^3)$. Obviously, the overall complexity only increases linearly in N_b, thus is low. It is noted that the low-complexity operation of the FDE is independent of the channel length L, whereas the time-domain equalization (TDE) methods [6,8] have their complexity increase in the cubic of L. For a highly-dispersive UWA channel, the value of L amounts to several tens or even over one hundred, and

the complexity of the time-domain equalization will get very high. Therefore, the FDE is a better choice than the TDE from the point view of complexity, especially for UWA communications.

With the estimated frequency-domain symbols, $\{\hat{\mathbf{X}}_k\}_{k=1}^{N_b}$, of all N_b subsystems, the time-domain symbol estimations, $\hat{\mathbf{x}}$, can be obtained as

$$\hat{\mathbf{x}} \quad = \quad \mathbf{F}_x^H \hat{\mathbf{X}} \tag{19}$$

where $\hat{\mathbf{X}} = [\hat{\mathbf{X}}_1, \hat{\mathbf{X}}_2, \cdots, \hat{\mathbf{X}}_{N_b}]^T$. In conventional one-time equalization, symbol detection will be made based on the estimated vector $\hat{\mathbf{x}}$. In turbo equalization, instead, the extrinsic bit LLRs will be calculated based on $\hat{\mathbf{x}}$. For the estimated symbol $\hat{x}_{n,k}$, the extrinsic LLR of its j-th demapping bit is evaluated as follows [17]

$$L_e(c_{n,k}^j|\hat{x}_{n,k}) \quad = \quad \ln \frac{\sum_{\forall \alpha \in \mathcal{S}, a^j=0} p(\hat{x}_{n,k}|x_{n,k}=\alpha) \prod\limits_{j' \neq j} P(c_{n,k}^{j'} = a^{j'})}{\sum_{\forall \alpha \in \mathcal{S}, a^j=1} p(\hat{x}_{n,k}|x_{n,k}=\alpha) \prod\limits_{j' \neq j} P(c_{n,k}^{j'} = a^{j'})} \tag{20}$$

According to (8), the conditional probability density function (PDF) $p(\hat{x}_{n,k}|x_{n,k}=\alpha)$ needs to be determined. By using the common assumption of Gaussian distribution [17], the determination of the PDF is equivalent to fining the conditional mean, $\mu_{n,k} \triangleq \mathbb{E}\{\hat{x}_{n,k}|x_{n,k}=\alpha\}$, and the conditional variance, $\eta_{n,k}^2 \triangleq \mathrm{cov}(\hat{x}_{n,k}, \hat{x}_{n,k}|x_{n,k}=\alpha)$.

The computation of the conditional mean and variance requires extra complexity. During the undersea data processing, however, we adopt an approximate approach for computing $\mu_{n,k}$ and $\eta_{n,k}^2$ to further reduce the detection complexity. The approximating method is based on the fact that an estimated symbol $\hat{x}_{n,k}$ can be written as follows

$$\hat{x}_{n,k} \quad = \quad \rho x_{n,k} + \zeta \tag{21}$$

where $x_{n,k}$ is the actually transmitted symbol, ρ is a scale factor, and ζ is the additive estimation noise. Based on (21), the parameter ρ is first estimated as

$$\hat{\rho} = \sqrt{\frac{1}{N_b}\sum_{k=1}^{N_b}\frac{|\hat{x}_{n,k}|^2}{|\breve{x}_{n,k}|^2}} \tag{22}$$

where $\breve{x}_{n,k}$ denotes the hard decision of $\hat{x}_{n,k}$. The conditional mean and variance can then be approximately computed as

$$\mu_{n,k} \approx \hat{\rho}\alpha \tag{23}$$

$$\eta_{n,k}^2 \approx \mathbb{E}\{\zeta^2\} \approx \frac{\sum_{k=1}^{N_b}(|\hat{x}_{n,k} - \mu_{n,k}|^2)}{N_b} \tag{24}$$

Once $\mu_{n,k}$ and $\eta_{n,k}^2$ are determined, the conditional PDF $p(\hat{x}_{n,k}|x_{n,k} = \alpha)$ and the extrinsic bit LLR $L_e(c_{n,k}^j|\hat{x}_{n,k})$ are obtained. The extrinsic bit LLRs of the FDE will then be de-interleaved and delivered to the LDPC decoder for decoding.

3.2 SOFT-DECISION LDPC DECODER

The Column-Weight-Three binary LDPC codes [18], [19] with code word length 2048, 3072 and 4096 have been adopted in both experiments. The code rate is $\frac{1}{2}$. The LDPC decoding has been extensively studied in the literature, and we adopt the sum-product algorithm proposed in [10]. Details are omitted for brevity.

The extrinsic LLR generated by the LDPC decoder will be interleaved and fed back to the FDE for launching the next iteration of the turbo equalization. When the turbo detection converges, the LDPC decoder outputs the hard decisions of the information bits and this completes the turbo detection.

4 EXPERIMENTAL RESULTS

The proposed low-complexity turbo detector has been tested by real-world data collected in two undersea experiments. The first experiment named WHOI09, was conducted at Buzzard's Bay, MA, in December 2009. The second experiment named ACOMM09, was launched at the coastline of New Jersey in May 2009. Results for the two experiments are presented in the following two subsections, respectively.

4.1 RESULTS OF WHOI09 EXPERIMENT

In this experiment, the symbol period was 0.04 ms and the carrier frequency was 32.5 kHz. Modulation schemes included QPSK, 8PSK and 16QAM, resulting transmission rates of 50 kilo-bits per second (kbps), 75 kbps, and 100 kbps, respectively, for a single transducer. The transmit equipment, consisting of two transducers, was located about 6 m below the sea surface. The water depth was about 14 m. Two receive hydrophone arrays named R1 and R2 were deployed, and their distances to the transmitter were 2 km and 1 km, respectively. Each receive array consisted of four hydrophones.

The zero-padded blocks were organized into packets for transmission during the experiment, with the packet structure shown in Fig. 4.1. From the figure, auxiliary signal including two linear frequency modulation (LFM) sequences named LFMb and LFMe, and one m-sequence, are also transmitted. The LFM sequences serve multiple purposes like packet coarse synchronization, Doppler shift estimation, and channel length measurement. The m-sequence can be used to evaluate the channel scattering function. Details are referred to [12]. The data payload consists of multiple blocks separated by padded zeros. The zero-padding length has been chosen as $N_g = 300$ to avoid inter-block interference under highly-dispersive UWA channels. Each block contains N_b modulation symbols, out of which the N_p ones at the head are used

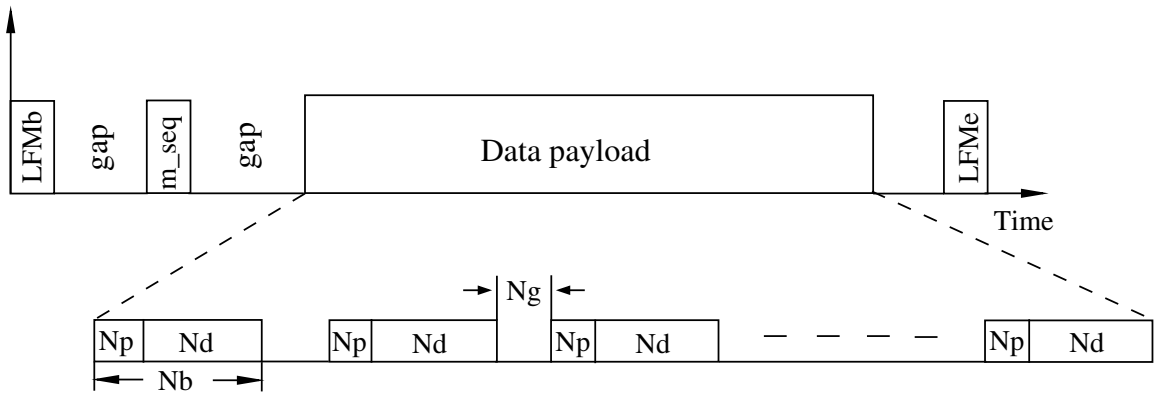

Figure 4.1. Packet structure in WHOI09 experiment.

as pilots for channel estimation and the remaining $N_d = N_b - N_p$ symbols convey information. The block size N_b has three choices: 1024, 2048 and 4096. For a given packet, the block size N_b is fixed while the three modulations are all used. For a given block, it carries one or more LDPC code words depending on the modulation adopted.

In Fig. 4.2, an example of the normalized correlation between the received signal and the local LFMb signal is demonstrated. In the left subfigure, two correlation peaks are observed due to the two-transducer transmission. Either peak indicates the coarse synchronization point. To measure the length of the practical channel, the right correlation ridge in the left subfigure, is zoomed in in the right subfigure. From the subfigure, it is obvious that most of the correlation energy is concentrated inside a time window of size about 2.4 ms, which corresponds to a symbol-spaced channel length of $L = 60$. For such a channel length, the pilot length is chosen as $N_p = 220$. An example of the estimated UWA channels between the transmit array and the receive array R2 is illustrated in Fig. 4.3, where 'T' and 'H' denote transducer and hydrophone, respectively. The subchannels corresponding to the fourth hydrophone are not shown because during the data processing, it was found that hydrophone failed to function. The same problem happened with R1, thus the detection has been

performed with the three normal hydrophones for both R1 and R2. From the figure, the channel impulse responses are non-minimum phase.

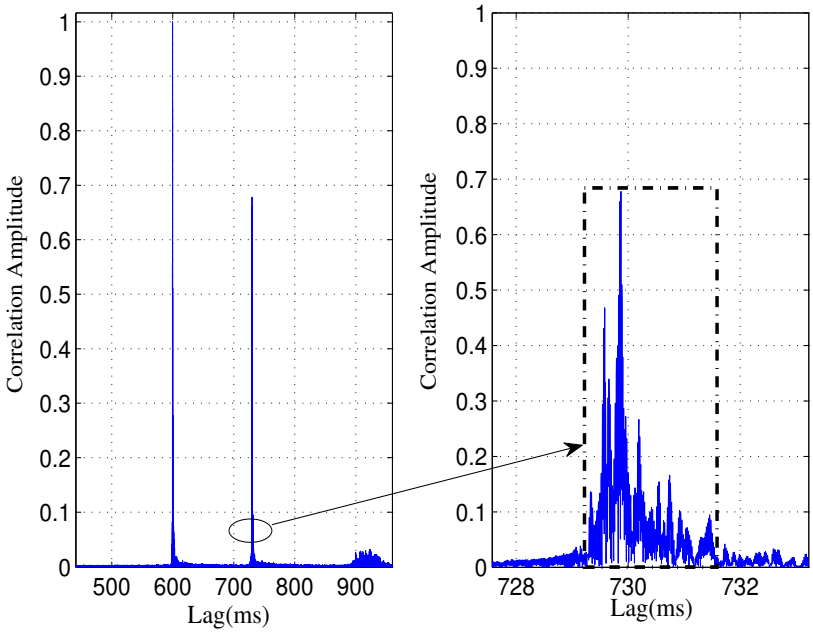

Figure 4.2. Correlation between the received signal and the local LFMb signal.

With the estimated channel knowledge, turbo equalization can be performed. To demonstrate the progress of equalization, Fig. 4.4 shows the estimated symbols at the output of the FDE and the soft-decision symbols at the output of the LDPC decoder, respectively, over multiple iterations. The modulation is 16QAM. From the figure, the performance improvement attributed to the iterative operations is intuitively observed.

Detection results for this experiment are next presented. Five packets have been detected for both R1 and R2. Each packet contains twelve $N_b = 1024$ blocks for each of the three modulations QPSK, 8PSK and 16QAM. The number of LDPC decoding iterations has been fixed as 15. The detection performance metric is chosen

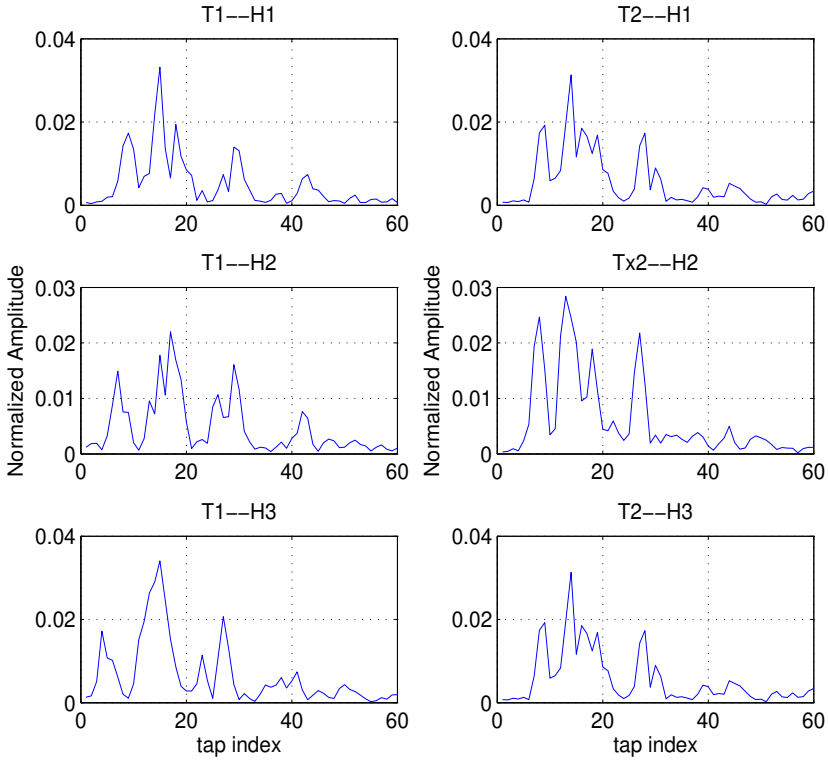

Figure 4.3. Estimated channels in WHOI09 experiment.

as the bit error rate (BER), which is defined as the ratio between the total number of error bits and the total number of information bits. The BERs are listed in Table 4.1, where N_{det} denotes the number of detection iterations.

From the table, it is obvious that error-free detection has been achieved for QPSK modulation with only two detection iterations. The BERs for the 8PSK and 16QAM modulations are in the order of 10^{-4} and 10^{-3} on both hydrophone arrays, with four detection iterations. It is expected that better performance can be achieved if all four hydrophones are used for detection.

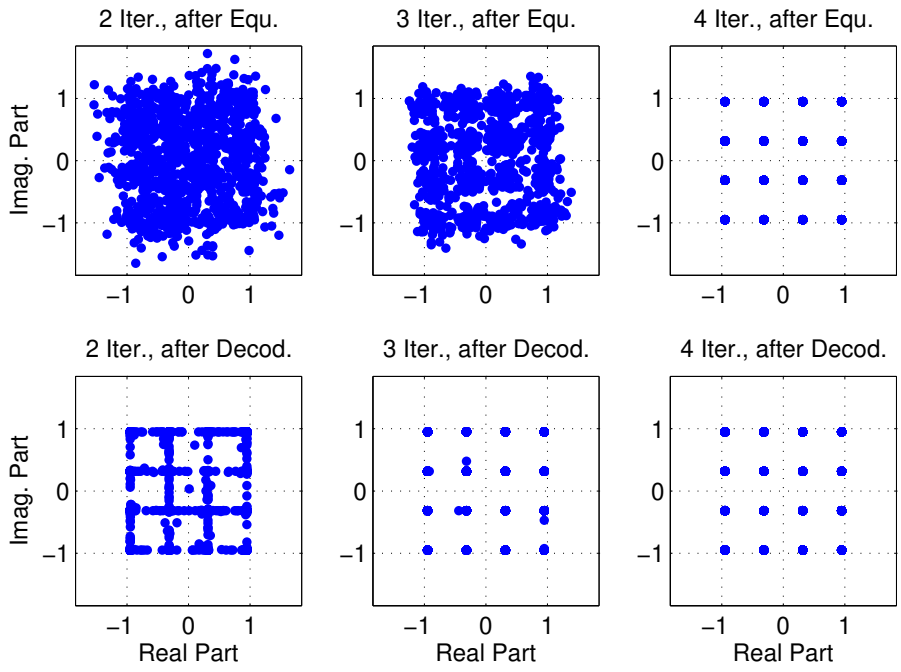

Figure 4.4. Demonstration of the turbo equalization process (16QAM)

Table 4.1. BER Results for 2×3 MIMO in WHOI09 experiment

Mod. \ N_{det}		1	2	3	4
R1	QPSK	2.3×10^{-4}	0	0	0
	8PSK	1.5×10^{-2}	2.8×10^{-4}	9.8×10^{-5}	9.8×10^{-5}
	16QAM	5.8×10^{-2}	4.2×10^{-3}	2.0×10^{-3}	1.9×10^{-3}
R2	QPSK	2.1×10^{-4}	0	0	0
	8PSK	1.3×10^{-2}	2.1×10^{-4}	8.1×10^{-5}	8.1×10^{-5}
	16QAM	5.3×10^{-2}	4.1×10^{-3}	1.2×10^{-3}	1.1×10^{-3}

4.2 RESULTS OF ACOMM09 EXPERIMENT

In this experiment, the symbol period was 0.2 ms and the carrier frequency was 17 kHz. Three modulation schemes including QPSK, 8PSK and 16QAM, were used.

The transmit equipment was a four-transducer array, for which the number of active transducers was flexibly configured to implement different MIMO transmission during the experiment. Two hydrophone arrays named ACDS2 and ACDS3 were deployed, and each of them consisted of eight elements. The inter-hydrophone spacing was 2.06 m on both arrays. The distances between ACDS2 and ACDS3 to the transmit equipment were 2 km and 3 km, respectively.

The data blocks were again encapsulated into packets for transmission, similar to the WHOI09 experiment. The block size had two choices: $N_b = 1024$ and $N_b = 2048$, and each block carried one or more LDPC code words. Different from the WHOI09 experiment, each packet only used one instead of all three modulation schemes.

The channel length was measured as $L = 100$ in this trial, and the pilot block length was selected as $N_p = 350$. In Fig. 4.5, the estimated undersea channels between the transmit array and the receive array ACDS2 are demonstrated. Clearly, the CIRs are non-minimum phase and sparse, and have several distinct spikes.

Four packets have been detected for each of the three modulations, for both ACDS2 and ACDS3. Each packet contains 50 blocks with a block size $N_b = 1024$. The detection results of the two-transducer transmission, are shown in Table 4.2 through Table 4.4 for the three different modulations. The parameter N_{dec} in all tables denotes the number of LDPC decoding iterations. From the tables, the BER results corresponding to different combinations of detection iteration number, N_{det}, and decoding iteration number, N_{dec}, have been provided for comparison. We make the following observations for the results. First, for a fixed number of detection iterations, N_{det}, the system performance increases with the number of decoding iterations, N_{dec}. Similarly, when the number of decoding iterations, N_{dec}, is fixed, the performance improves with the number of detection iterations, N_{det}, as we already observed in the WHOI09 result. Second, for QPSK and 8PSK modulations, error-free

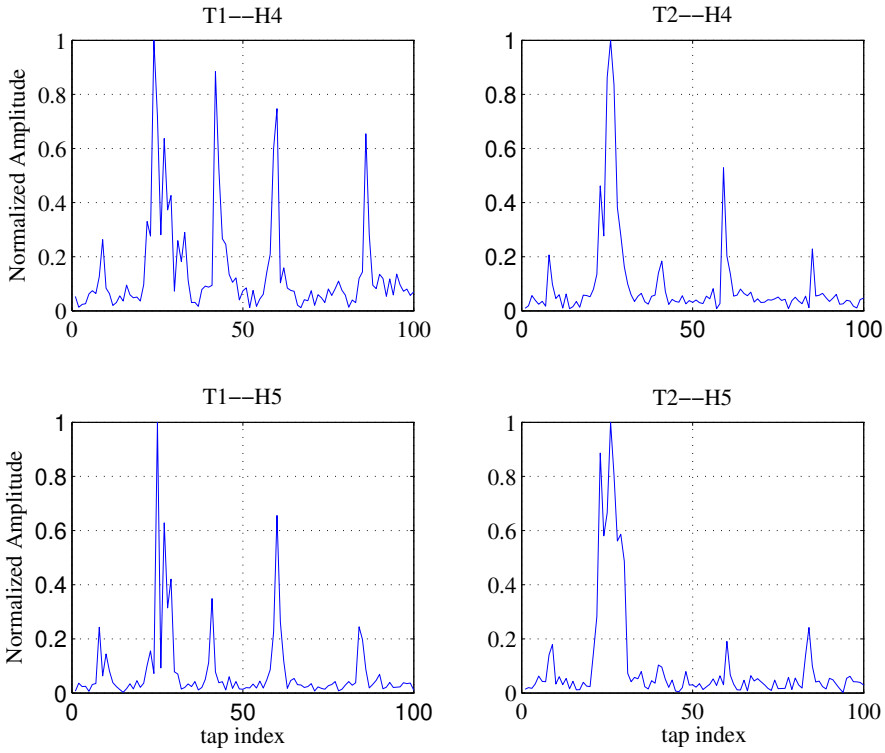

Figure 4.5. Estimated channels in ACOMM09 experiment.

detection has been achieved on both ACDS2 and ACDS3. As expected, the 8PSK modulation requires more iterations than the QPSK modulation to reach zero BER. Third, in Table 4.4, performance bound has been observed for ACDS3. Particularly, when $(N_{\text{det}}, N_{\text{dec}}) = (2, 7)$, the BER stops decreasing even both iteration numbers are increasing. This phenomena is explained by the convergence behavior of turbo detection [21]. This observation provides us the hint to select a proper combination of $(N_{\text{det}}, N_{\text{dec}})$, which leads to the best performance-complexity tradeoff. Last, with a 16QAM modulation, a BER on the order of 10^{-5} can be achieved for both ACDS2 and ACDS3.

Table 4.2. BER for 2×8 MIMO in ACOMM09 experiment (QPSK)

	N_{det} \ N_{dec}	1	2	3
ACDS2	1	1.8×10^{-4}	0	0
	2	4.8×10^{-5}	0	0
	3	4.0×10^{-5}	0	0
	4	3.9×10^{-5}	0	0
ACDS3	1	3.7×10^{-6}	0	0
	2	0	0	0

For the results shown in Table 4.2 through Table 4.4, all eight hydrophone elements have been used for detection. Attributed to the spatial diversity provided by all eight hydrophones, the turbo detection converges very fast. For example, in Table 4.2, perfect detection can be achieved with only one detection iteration and two decoding iterations. More hydrophones provides more diversity gain, however, also incurs higher detection complexity. As a result, hydrophone selection becomes another degree of freedom to balance the performance-complexity tradeoff. To demonstrate that, we re-detect all the packets by using only four hydrophones with indices $1, 3, 5, 7$. The new results are given through Table 4.5 to Table 4.7. From Table 4.5, the detection performance for ACDS3 almost does not degrade compared with that in Table 4.2. For ACDS2, performance degradation is observed by comparing with Table 4.2. However, perfect detection can still be achieved with only one detection iteration when the number of decoding iteration increases to 9. For 8PSK and 16QAM modulations, the results for both ACDS2 and ACDS3 degrade compared with those

Table 4.3. BER for 2×8 MIMO in ACOMM09 experiment (8PSK)

	N_{det} \ N_{dec}	1	3	5	7	9
ACDS2	1	6.7×10^{-3}	7.5×10^{-4}	9.2×10^{-5}	2.4×10^{-6}	0
	2	4.8×10^{-3}	2.5×10^{-4}	7.2×10^{-6}	0	0
	3	4.2×10^{-3}	1.6×10^{-4}	2.4×10^{-6}	0	0
	4	4.0×10^{-3}	1.5×10^{-4}	2.4×10^{-6}	0	0
	N_{det} \ N_{dec}	1	3	5	7	9
ACDS3	1	1.3×10^{-3}	3.9×10^{-4}	9.3×10^{-5}	1.1×10^{-5}	0
	2	1.1×10^{-3}	3.0×10^{-4}	3.5×10^{-5}	0	0
	3	1.1×10^{-3}	3.0×10^{-4}	1.5×10^{-5}	0	0
	4	1.0×10^{-3}	1.4×10^{-4}	9.9×10^{-6}	0	0

obtained using all eight hydrophones. Nevertheless, the achievable BERs on the order of 10^{-5} and 10^{-4} are still satisfactory.

Finally, we briefly discussed the signal detection for MIMO transmission with more than two transducers. Due to the increased number of transducers, the pilot block size N_p has to be enlarged so as to achieve accurate channel estimations. The resulting pilot overhead will be very large for each transmission block. To maintain an acceptable pilot percentage, we have adopted a different channel estimation scheme. In the new scheme, transmission blocks within a packet are classified into two categories: pilot blocks and information blocks. The pilot blocks are used specifically for channel estimation, while the detected information blocks are used for channel tracking. For example, we select blocks with indices 1, 11, 21, 31 and 41 as pilot blocks for channel estimation, and use each detected information block to re-estimate

Table 4.4. BER for 2×8 MIMO in ACOMM09 experiment (16QAM)

	N_{det} \ N_{dec}	3	5	7	9	11
ACDS2	1	4.4×10^{-3}	1.4×10^{-3}	4.6×10^{-4}	1.2×10^{-4}	3.3×10^{-5}
	2	3.0×10^{-3}	7.3×10^{-4}	1.4×10^{-4}	1.6×10^{-5}	1.5×10^{-5}
	3	2.7×10^{-3}	5.6×10^{-4}	1.0×10^{-4}	1.6×10^{-5}	1.3×10^{-5}
	4	2.6×10^{-3}	5.4×10^{-4}	1.0×10^{-4}	1.6×10^{-5}	1.3×10^{-5}
	N_{det} \ N_{dec}	1	3	5	7	9
ACDS3	1	3.8×10^{-3}	5.4×10^{-4}	6.4×10^{-5}	1.2×10^{-5}	1.2×10^{-5}
	2	2.9×10^{-3}	2.4×10^{-4}	1.5×10^{-5}	1.0×10^{-5}	1.0×10^{-5}
	3	2.6×10^{-3}	1.2×10^{-4}	1.2×10^{-5}	1.0×10^{-5}	1.0×10^{-5}
	4	2.6×10^{-3}	1.2×10^{-4}	1.1×10^{-5}	1.0×10^{-5}	1.0×10^{-5}

the channel for detecting the next adjacent information block. In this case, only 5 out of 50 blocks are used as pilot blocks and the pilot overhead is only 10%. With the modified channel estimation mechanism, perfect detection has been achieved with some QPSK packets measured under 4×8 MIMO transmission. As to 8PSK and 16QAM modulations, the detection becomes much more challenging due to the error propagation in the decision-directed channel tracking. To provide an effective channel tracking in the case of high modulations, will be the focus of our future work.

Table 4.5. BER for 2×4 MIMO in ACOMM09 experiment (QPSK)

	N_{dec} / N_{det}	1	3	5	7	9
ACDS2	1	3.0×10^{-3}	3.2×10^{-4}	3.0×10^{-5}	3.7×10^{-6}	0
	2	2.2×10^{-3}	1.6×10^{-4}	9.8×10^{-6}	0	0
	3	2.1×10^{-3}	1.5×10^{-4}	7.4×10^{-6}	0	0
	4	2.0×10^{-3}	1.4×10^{-4}	7.4×10^{-6}	0	0
ACDS3	N_{dec} / N_{det}	1	3	5	7	9
	1	5.3×10^{-5}	0	0	0	0
	2	0	0	0	0	0
	3	0	0	0	0	0
	4	0	0	0	0	0

Table 4.6. BER for 2×4 MIMO in ACOMM09 experiment (8PSK)

	N_{dec} / N_{det}	1	3	5	7	9
ACDS2	1	8.0×10^{-3}	6.9×10^{-4}	3.5×10^{-4}	2.3×10^{-4}	2.0×10^{-4}
	2	7.4×10^{-3}	5.3×10^{-4}	2.6×10^{-4}	1.3×10^{-4}	1.2×10^{-4}
	3	7.1×10^{-3}	4.8×10^{-4}	2.1×10^{-4}	1.0×10^{-4}	3.8×10^{-5}
	4	6.7×10^{-3}	4.3×10^{-4}	1.7×10^{-4}	8.8×10^{-5}	2.9×10^{-5}
ACDS3	N_{dec} / N_{det}	1	3	5	7	9
	1	1.5×10^{-3}	6.1×10^{-4}	2.9×10^{-4}	2.1×10^{-4}	1.8×10^{-4}
	2	1.4×10^{-3}	4.6×10^{-4}	2.1×10^{-4}	1.2×10^{-4}	1.1×10^{-4}
	3	1.4×10^{-3}	4.1×10^{-4}	1.8×10^{-4}	8.8×10^{-5}	2.9×10^{-5}
	4	1.3×10^{-3}	4.0×10^{-4}	1.6×10^{-4}	6.8×10^{-5}	1.7×10^{-5}

Table 4.7. BER for 2×4 MIMO in ACOMM09 experiment (16QAM)

	N_{det} \ N_{dec}	3	5	7	9	11
ACDS2	1	2.3×10^{-2}	2.0×10^{-2}	1.9×10^{-2}	1.8×10^{-2}	1.8×10^{-2}
	2	9.0×10^{-3}	6.0×10^{-3}	5.0×10^{-3}	4.6×10^{-3}	4.3×10^{-3}
	3	5.8×10^{-3}	3.5×10^{-3}	2.4×10^{-3}	1.5×10^{-3}	9.6×10^{-4}
	4	4.8×10^{-3}	2.8×10^{-3}	2.0×10^{-3}	1.2×10^{-3}	7.6×10^{-4}
	N_{det} \ N_{dec}	1	3	5	7	9
ACDS3	1	1.9×10^{-2}	5.6×10^{-3}	2.9×10^{-3}	1.8×10^{-3}	1.4×10^{-3}
	2	1.4×10^{-2}	2.9×10^{-3}	1.2×10^{-3}	9.1×10^{-4}	6.3×10^{-4}
	3	1.1×10^{-2}	2.0×10^{-3}	8.5×10^{-4}	6.5×10^{-4}	5.1×10^{-4}
	4	1.0×10^{-2}	1.6×10^{-3}	7.8×10^{-4}	5.9×10^{-4}	4.4×10^{-4}

5 CONCLUSION

A low-complexity turbo detection scheme was proposed for single-carrier LDPC-coded MIMO UWA communications. The new detector achieved the low-complexity advantage by using the frequency-domain equalization technology combined with the computationally-efficient LDPC decoding. The performance of the proposed detection scheme was tested by real-world data measured in the WHOI09 undersea experiment and the ACOMM09 undersea experiment. With QPSK modulation, it was shown that error-free detection could be achieved under two-transducer transmission for both experiments. With 8PSK modulation, the achievable BERs were in the order of 10^{-4} at a symbol rate of 25 ksps for WHOI09 experiment, while error-free detection can still be achieved at a symbol rate of 5 ksps for ACOMM09 experiment. With 16QAM modulation, achievable BERs were in the order of 10^{-3} and 10^{-5}, respectively, for the two experiments. Furthermore, the performance-complexity tradeoff issue was also investigated from two perspectives, *i.e.*, the combination of detection and decoding iteration numbers and the hydrophone selection. In summary, the proposed turbo detection scheme is a promising candidate for high data rate UWA communications.

ACKNOWLEDGMENTS

This work was supported in part by the Office of Naval Research under Grant N00014-10-1-0174 and the National Science Foundation under Grant CCF-0915846. The authors thank Mr. Lee Freitag and Mr. Keenan Ball and their team for conducting the WHOI09 experiment. L. Wang is grateful to Mr. Jian Zhang for his helpful discussion.

6 REFERENCES

[1] M. Stojanovic, J. Catipovic, and J. Proakis, "Phase-coherent digital communicaitons for underwater acoustic channels," *IEEE J. Ocean Eng.*, vol. 19, pp. 100-111, Jan. 1994.

[2] D. B. Kilfoyle and A. B. Baggeroer, "The state of the art in underwater acoustic telemetry," *IEEE J. Ocean Eng.*, vol. 25, pp. 4-27, Jan. 2000.

[3] T. C. Yang, "Correlation-based decision-feedback equalizer for underwater acoustic communications," *IEEE J. Ocean Eng.*, vol. 30, pp. 865-880, Oct. 2005.

[4] Y. R. Zheng, C. Xiao, T. C. Yang, and W. B. Yang , "Frequency-domain channel estimation and equalization for shallow-water acoustic communications," *Elsevier Journal of Physical Communi.*, vol. 3, pp. 48-63, March 2010.

[5] J. Tao, Y. R. Zheng, C. Xiao, T. C. Yang, and W. B. Yang, "Channel equalization for single carrier MIMO underwater acoustic communications," *EURASIP Journal on Advances in Signal Processing*, vol. 2010, Article ID 281769, 17 pages, 2010. doi:10.1155/2010/281769

[6] X. Wang and H. V. Poor, "Iterative (turbo) soft interference cancellation and decoding for coded CDMA," *IEEE Trans. Commun.*, vol. 47, pp. 1046-1061, July 1999.

[7] E. Biglieri, A. Nordio, and G. Taricco, "Iterative receivers for coded MIMO signaling," *Wirel. Commun. Mob. Comput.*, No. 4, pp. 697-710, 2004

[8] S. Roy, T. M. Duman, V. McDonald, and J. G. Proakis, "High rate communication for underwater acoustic channels using multiple transmitters and space-time coding: receiver structures and experimental results," *IEEE J. Ocean. Eng.*, vol. 32, pp. 663-688, July 2007.

[9] R. Otnes and T. H. Eggen, "Underwater acoustic communications: long-term test of turbo equalization in shallow water," *IEEE J. Ocean Eng.*, vol. 33, no. 3, pp. 321-334, July 2008

[10] J. Tao, Y. R. Zheng, C. Xiao, T. C. Yang, "Robust MIMO underwater acoustic communications using turbo block decision-feedback equalization," *IEEE J. Ocean. Eng.*, vol. 35, no. 4, pp. 948-960, Oct. 2010

[11] J. Huang, S. Zhou, and P. Willett, "Nonbinary LDPC coding for multicarrier underwater acoustic communication," *IEEE JSAC Special Issue on Underwater Wireless Communications and Networks*, vol. 26, no. 9, pp. 1684-1696, Dec. 2008.

[12] B. Li, J. Huang, S. Zhou, K. Ball, M. Stojanovic, L. Freitag, and P. Willett, "MIMO-OFDM for high rate underwater acoustic communications," *IEEE J. Ocean. Eng.*, vol. 34, pp. 634-644, Oct. 2009.

[13] L. Bahl, J. Cocke, F. Jelinek, and J. Raviv, "Optimal decoding of linear codes for minimizing symbol error rate," *IEEE Trans. Inform. Theory*, vol. 20, pp. 284-287, March 1974.

[14] L. Dong and Y. Zhao, "Frequency-domain turbo equalization for signal carrier mobile broadband systems," in *Proc. IEEE Military Communications Conference*, Oct. 2006

[15] Y. R. Zheng and C. Xiao, "Channel estimation for frequency-domain equalization of single carrier broadband wireless communications," *IEEE Trans. Veh. Technol.*, vol. 58, pp. 815-823, Feb. 2009.

[16] M. Sabbaghian and D. Falconer, "Comparison between convolutional and LDPC code-based turbo frequency domain equalization," in *Proc. ICC'06*, vol. 12, pp. 5432-5437, June 2006

[17] M. Tüchler, A. C. Singer, and R. Koetter, "Minimum mean squared error equalization using a priori information," *IEEE Trans. Signal Processing*, vol. 50, no. 3, pp. 673-683, March 2002.

[18] S. K. Chilappagari and B. Vasic, "Error-correction capability of column-weight-three LDPC codes," *IEEE Trans. Info. Theory*, vol. 55, no. 5, pp. 2055-2061, May 2009

[19] T. J. Richardson and R. Urbanke, "Efficient encoding of low-density parity-check codes," *IEEE Trans. Info. Theory*, vol. 47, pp. 638-656, Feb. 2001.

[20] W. E. Ryan, "An Introduction to LDPC Codes," in *CRC Handbook for Coding and Signal Processing for Recording Systems* (B. Vasic, ed.), CRC Press, 2004.

[21] S. ten Brink, "Convergence behavior of iteratively decoded parallel concatenated codes," *IEEE Trans. Commun.*, vol. 49, no. 10, pp. 17271737, Oct. 2001.

II. Frequency Domain Turbo Equalization for No-CP Single-Carrier MIMO Underwater Acoustic Communications

Longbao Wang, Jun Tao, and Yahong Rosa Zheng

ABSTRACT—This paper proposes a frequency-domain turbo detection scheme for single-carrier, multiple-input, multiple output (MIMO) underwater acoustic (UWA) transmission without using cyclic prefix (CP), aiming to achieve a low detection complexity and a high transmission efficiency simultaneously. The received data stream is divided into consecutive blocks, and each block is equalized in the frequency domain. To enable the frequency-domain equalization, inter-block-interference (IBI) cancelation and CP reconstruction are necessary for each block. The IBI is removed by using the currently estimated channel and the detected symbols from the previous block. The CP reconstruction for the current iteration of the turbo equalization is obtained with the soft symbol estimation from the previous iteration. In the first iteration, there is no *a priori* soft symbol estimation available, thus the frequency-domain equalizer (FDE) is performed in an approximating style. The detection performance improves over iterations. The proposed scheme has been tested by field trial data measured in the ACOMM09 underwater communication experiment.

1 INTRODUCTION

Fast progress has been achieved in underwater acoustic (UWA) communication recently [1]- [11]. Basically, the signal detection can be classified into two main categories: time-domain detection [1]– [14] and frequency-domain detection [5]– [11]. In [1], decision-feedback equalizer (DFE) coupled with a digital phase-locked loop (PLL) has been adopted. In [12], turbo block DFE (BDFE) is proposed for UWA communications, and the BDFE provides better performance than the conventional DFE. In [8, 14], turbo linear equalizer (LE) and an enhanced turbo LE have also been proposed. Frequency-domain detection for single-carrier systems and for the multi-carrier orthogonal frequency division multiplexing (OFDM) systems are found in [5, 6] and [9, 11], respectively.

For the time-domain detection, it achieves a high transmission efficiency since there is no need to divide the transmission stream into blocks separated by guard interval like cyclic prefix (CP) or zero padding (ZP). However, the equalization complexity is usually high especially under the UWA channels. In contrast, the frequency-domain detection used in either OFDM or single-carrier systems, incurs a very low equalization complexity which is independent of the channel length L. To achieve the low-complexity equalization, however, the data stream has to be partitioned into blocks separated by guard intervals, and the data transmission efficiency is thus decreased.

In this paper, we aims to perform frequency-domain detection for single-carrier multiple-input, multiple output (MIMO) UWA transmission without using CP, such that the advantage of low detection complexity and high transmission efficiency can be achieved simultaneously. This goal is made possible under the framework of turbo equalization [14, 6, 2]. Without CP, inter-block-interference (IBI) arises and the circular channel structure is unavailable. The IBI existing in the current block can be

removed by utilizing the estimated channel and the estimated symbols of a previous block. As to the circular channel structure, it can be obtained by reconstructing the signal component which would have been contributed by CP, with the estimated symbols obtained from the previous iteration. During the first iteration of the turbo equalization, there is no previous symbol estimations available, so the frequency-domain equalizer (FDE) is performed in an approximating style. When the iteration progresses, the previous soft estimations become more and more reliable, and the detection performance approaches that with CP. Additionally, to deal with the fast time variations in the UWA channel, a decision-directed channel tracking mechanism is adopted, for which a previously estimated block is used to update the channel knowledge for equalizing the current block. In this way, the pilot overhead is reduced and the transmission efficiency can be further increased.

The proposed detection scheme has been tested by the real-world data measured during the ACOMM09 underwater experiment conducted off the coastline of New Jersey in May 2009. The transmission rate was 5 kilo symbols per second (ksps) per transducer at a transmission distance of $2 \sim 3$ km. Experimental results show that the proposed scheme is viable for high-efficiency, low-complexity UWA communications.

Throughout this paper, $(\cdot)^T$ represents the matrix transpose.

2 SYSTEM MODEL

Consider a single-carrier MIMO UWA communication system with N_t transducers and N_r hydrophones. The k-th received sample on the m-th hydrophone is given as follows

$$y_{m,k} = \sum_{n=1}^{N_t} \sum_{l=0}^{L-1} h_{m,n}(k,l) x_{n,k-l} + v_{m,k}, \tag{1}$$

where $x_{n,k-l}$, $h_{m,n}(k,l)$, and $v_{m,k}$ are the transmitted symbol from the n-th transducer, the time-varying subchannel between the n-th transducer and the m-th hydrophone, and the additive noise with variance σ^2, respectively. All subchannels are assumed to have the same length L.

The block diagram of the proposed detection scheme is shown in Fig. 1.1. From the figure, the received data stream is first passed to the block partition unit. The output blocks are then send to the next unit for IBI cancelation and CP reconstruction. After that, the blocks are ready to be equalized in the frequency domain. The equalizer exchanges extrinsic soft log-likelihood ratio (LLR) information with the soft channel decoder in an iterative way. During the experiment, the low-density parity-check (LDPC) coding was adopted, so the channel decoder is a LDPC decoder which is inherently iterative. In the last iteration of the turbo equalization, hard

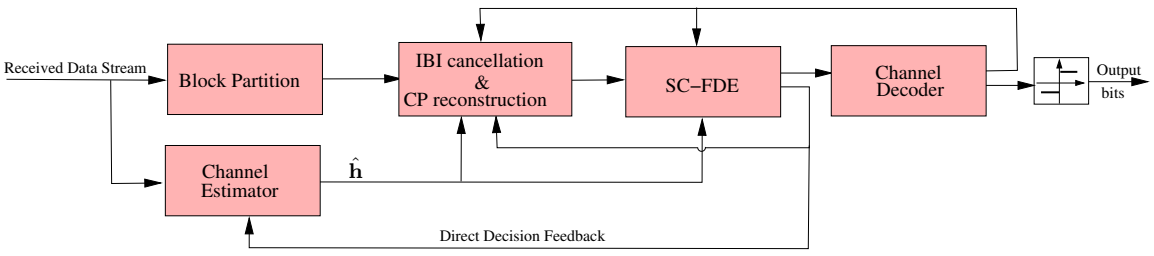

Figure 2.1. Block diagram of the proposed turbo detection scheme.

decisions are made for the information bits. During the detection, the output of the equalizer will be used for channel tracking. Channel estimation and tracking is referred to [12]. The output of the LDPC decoder will be used for IBI cancelation and CP reconstruction. Details are presented in the next section.

3 FREQUENCY-DOMAIN EQUALIZATION WITHOUT CP

In a no-CP transmission, the data is transmitted in the form of continuous stream of a large size. As mentioned before, the received stream is partitioned into blocks for processing. Due to the absence of guard interval, IBI arises between adjacent blocks and the channel matrix is not circular. To enable frequency-domain equalization, IBI has to be canceled. The cancelation of IBI relies on the estimated channel for the current block and the estimated symbols from the previous block, as in [12]. After IBI cancelation, mechanism is devised to make the channel matrix circular. The method to make a circular channel matrix in the first iteration of the turbo equalization is different from that used in the second iteration and beyond. We will discuss the two different methods separately in the following.

3.1 FIRST ITERATION

Define $\mathbf{x}_k^i = [x_{1,k}^i, x_{2,k}^i, \ldots, x_{N_t,k}^i]^T$ and $\mathbf{y}_k^i = [y_{1,k}^i, y_{2,k}^i, \ldots, y_{N_r,k}^i]^T$ as the k-th transmitted vector and the k-th received vector of the i-th block, respectively. The IBI cancelation is performed as follows

$$\hat{\mathbf{y}}_k^i = \begin{cases} \mathbf{y}_k^i - \sum_{l=k}^{L-1} \mathbf{h}^{i-1}(l)\check{\mathbf{x}}_{N_b-L+1+l}^{i-1} & k = 1, \ldots, L-1, \\ \mathbf{y}_k^i & k = L, \ldots, N. \end{cases} \tag{2}$$

where $\mathbf{h}^{i-1}(l)$ is the l-th channel tap matrix of size $N_r \times N_t$ corresponding to the $(i-1)$-th block. The time index k has been dropped from the channel tap, considering that within one block, the channel can be treated as quasi-static [12]. $\check{\mathbf{x}}_k^{i-1}$ is the detected symbol vector of the previous block, and the parameter N is the size of a partitioned block.

Define

$$\mathbf{x}^i = [(\mathbf{x}_1^i)^T, (\mathbf{x}_2^i)^T, \ldots, (\mathbf{x}_N^i)^T]^T \tag{3}$$

$$\hat{\mathbf{y}}^i = [(\hat{\mathbf{y}}_1^i)^T, (\hat{\mathbf{y}}_2^i)^T, \ldots, (\hat{\mathbf{y}}_N^i)^T]^T. \tag{4}$$

Assuming a perfect IBI cancelation, then $\hat{\mathbf{y}}^i$ can be expressed as follows

$$\hat{\mathbf{y}}^i = \mathbf{h}^i \mathbf{x}^i + \mathbf{v}^i \tag{5}$$

where $\mathbf{h}^i$ is a block Toeplitz matrix with the first column being $\mathbf{h}_{:,1}^i = [(\mathbf{h}^i(0))^T, (\mathbf{h}^i(1))^T$ $, \cdots, (\mathbf{h}^i(L-1))^T, \mathbf{0}^T, \cdots, \mathbf{0}^T]^T$, with each zero matrix having a size of $N_r \times N_t$. The matrix $\mathbf{h}^i$ does not possess a circular structure, thus is not convenient for frequency-domain processing. To proceed, we rewrite (7) as (9), which is shown at the top of the next page.

From Eqn. (9), a circular channel matrix $\mathbf{h}_{\text{cir}}^i$ has been constructed, and it is desirable for frequency-domain processing. For convenience, the block index i has been dropped for each tap matrix in $\mathbf{h}_{cir}^i$. In this case, the signal vector to be detected becomes $\tilde{\mathbf{x}}^i$ which contains $\mathbf{x}_1^i, \cdots, \mathbf{x}_{N_b}^i$ with $N_b = N - L + 1$, and the vector $\mathbf{w}^i$ consists of both additive noise and the interference from the other $L-1$ symbols $\mathbf{x}_{N_b+1}^i, \cdots, \mathbf{x}_N^i$. In summary, only first N_b symbols are actually detected for a block size of N in the first iteration. Therefore, the block partition for the first iteration is performed in an overlapped way as shown in Fig.3.1.

To proceed, a size-N normalized discrete Fourier transform (DFT) matrix is applied on both sides of (9), leading to

$$\hat{\mathbf{Y}}^i = \mathbf{H}^i \tilde{\mathbf{X}}^i + \mathbf{W}^i, \tag{7}$$

where $\mathbf{H}^i$ is a block diagonal matrix. Details on the estimation of $\tilde{\mathbf{X}}^i$ (or equivalently, $\tilde{\mathbf{x}}^i$) based on (11), is referred to [6].

$$\underbrace{\begin{bmatrix} \hat{\mathbf{y}}_1^i \\ \hat{\mathbf{y}}_2^i \\ \vdots \\ \hat{\mathbf{y}}_N^i \end{bmatrix}}_{\hat{\mathbf{y}}^i} = \underbrace{\begin{bmatrix} \mathbf{h}(0) & 0 & \dots & \mathbf{h}(L-1) & \dots & \dots & \mathbf{h}(1) \\ \mathbf{h}(1) & \mathbf{h}(0) & 0 & \dots & \mathbf{h}(L-1) & \dots & \mathbf{h}(2) \\ \vdots & \ddots & \ddots & \ddots & \ddots & \ddots & \vdots \\ \mathbf{h}(L-1) & \dots & \mathbf{h}(0) & 0 & 0 & \dots & 0 \\ \vdots & \ddots & \ddots & \ddots & \ddots & \ddots & \vdots \\ 0 & \dots & 0 & \mathbf{h}(L-1) & \dots & \mathbf{h}(1) & \mathbf{h}(0) \end{bmatrix}}_{\mathbf{h}_{\text{cir}}^i} \times \underbrace{\begin{bmatrix} \mathbf{x}_1^i \\ \mathbf{x}_2^i \\ \vdots \\ \mathbf{x}_{N_b}^i \\ \mathbf{0}_{(L-1)\times 1} \end{bmatrix}}_{\tilde{\mathbf{x}}^i} + \mathbf{h}^i \underbrace{\begin{bmatrix} \mathbf{0}_{N_b\times 1} \\ \mathbf{x}_{N_b+1}^i \\ \mathbf{x}_{N_b+2}^i \\ \vdots \\ \mathbf{x}_N^i \end{bmatrix}}_{\mathbf{w}^i} + \mathbf{v}^i. \tag{6}$$

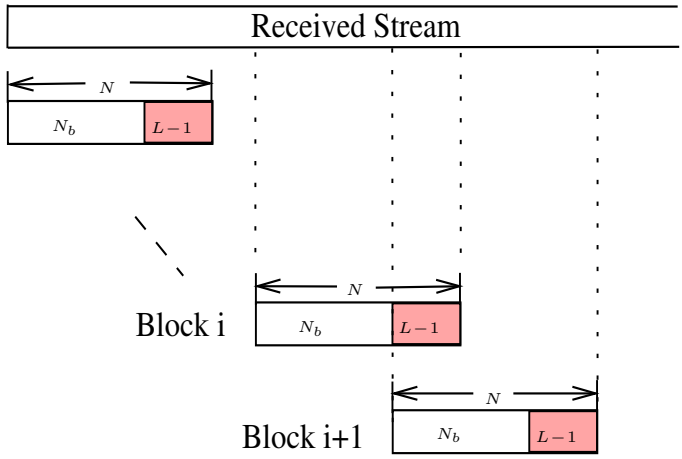

Figure 3.1. Block partition in the first iteration.

In turbo equalization, the bit extrinsic LLRs for each estimated symbol $\hat{x}_{n,k}^i$ is calculated as follows

$$L_e(c_{n,k}^{i,j}|\hat{x}_{n,k}^i) = \ln \frac{\sum_{\forall \alpha \in \mathcal{S}, a^j=0} p(\hat{x}_{n,k}^i | x_{n,k}^i = \alpha) \prod_{j' \neq j} P(c_{n,k}^{i,j'} = a^{j'})}{\sum_{\forall \alpha \in \mathcal{S}, a^j=1} p(\hat{x}_{n,k}^i | x_{n,k}^i = \alpha) \prod_{j' \neq j} P(c_{n,k}^{i,j'} = a^{j'})} \tag{8}$$

where $j = 1, \cdots, q$ for a constellation $\mathcal{S}$ of size 2^q. The groups of bits $\{a^j\}_{j=1}^q$ are mapped to α. The details for the calculation of $L_e(c_{n,k}^{i,j}|\hat{x}_{n,k}^i)$ is referred to [6, 2]. The extrinsic bit LLRs will be passed to the LDPC decoder for channel decoding.

3.2 SECOND ITERATION AND BEYOND

During the second iteration and beyond, soft symbol decisions are available from a previous iteration. In this case, after IBI cancelation, we can reconstruct the signal component for $\hat{\mathbf{y}}^i$ to obtain $\tilde{\mathbf{y}}^i$ as follows

$$\tilde{\mathbf{y}}_k^i = \begin{cases} \hat{\mathbf{y}}_k^i + \sum_{l=k}^{L-1} \mathbf{h}^i(l)\bar{\mathbf{x}}_{N+1-l}^i & k = 1, 2, \ldots, L-1, \\ \hat{\mathbf{y}}_k^i & k = L, \ldots, N. \end{cases} \tag{9}$$

where $\bar{\mathbf{x}}_k^i$ is the soft decision vector, with its element is calculated as follows

$$\bar{x}_{n,k}^i = \sum_{\alpha \in \mathcal{S}} \alpha \cdot P(x_{n,k}^i = \alpha), \tag{10}$$

The probability $P(x_{n,k}^i = \alpha)$ is calculated with the extrinsic information from the LDPC decoder in a previous iteration [2]. After CP reconstruction, the new signal vector $\tilde{\mathbf{y}}^i$ can be expressed as follows

$$\tilde{\mathbf{y}}^i = \mathbf{h}_{\text{cir}}^i \mathbf{x}^i + \mathbf{v}^i \tag{11}$$

which is ready to be processed in the frequency domain directly. When the iteration progresses, the soft decision $\bar{x}_{n,k}^i$ approaches its true value and the CP reconstruction gets more accurate, thus the detection performance also approaches that of a system using CP. Finally, attributed to the CP reconstruction, there is no need for overlapped

block partition since the second iteration. For each block of size N, N symbols are detected and the detection efficiency is higher than that of the first iteration.

3.3 LDPC DECODER

In the ACOMM09 experiment, Column-Weight-Three LDPC channel coding with coding rate 1/2 has been used. The codeword length can be 1024, 2048, or 4096. Each transmitted stream carries multiple LDPC codewords. For the LDPC decoding, the log-domain Sum-Product Algorithm (SPA) proposed in [10] has been adopted. Details are omitted here for brevity.

4 EXPERIMENTAL RESULTS

The proposed turbo detection scheme has been tested by field trial data measured in the ACOMM09 underwater experiment, which was conducted off the coastline of New Jersey in May 2009. The symbol period was 0.2 ms and the carrier frequency was 17 kHz. Modulations included QPSK, 8PSK, and 16QAM. The transmit array consisted of two transducers. Two receive arrays, ACDS2 and ACDS3, were deployed with their distances to the transmitter being 2 km and 3 km, respectively. Each receive array consisted of eight hydrophones with inter-hydrophone spacing being 2.06 m. During the experiment, both the transmit array and the two receive arrays were fixed.

The data stream was transmitted in packets, with the packet structure shown in Fig. 4.1. From the figure, each packet consists of two frames, and each frame carries $N_f = 25,600$ symbols. It is noted that this frame size N_f is much larger than the block size used in systems using CP [6, 9, 11]. Auxiliary signallings including two linear frequency modulated (LFM) sequences and one m-sequence, have also been transmitted. The usage of the auxiliary signals are referred to [12]. For the fixed transmission, the LFMb sequence is used for packet synchronization and the channel length measurement. The synchronization is achieved by correlating the received LFM signal with the local reference LFM sequence, and then detecting the correlation peak. Example of the normalized LFMb correlations for the ACDS2 and ACDS3 are depicted in Fig. 4.3. From the two subfigures, correlation peaks are clearly shown. Also, it is observed that both correlation ridges span about 20 ms, indicating an equivalent symbol-spaced channel length of $L \approx \frac{20 \text{ ms}}{T_s} = 100$.

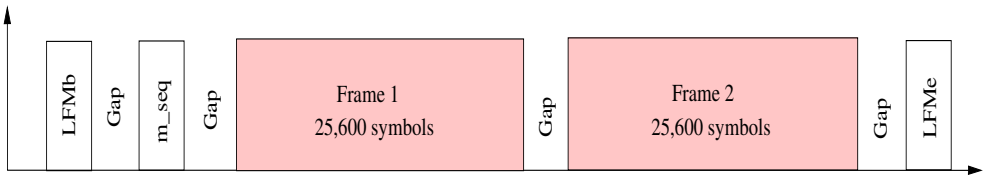

Figure 4.1. Packet structure for ACOMM09.

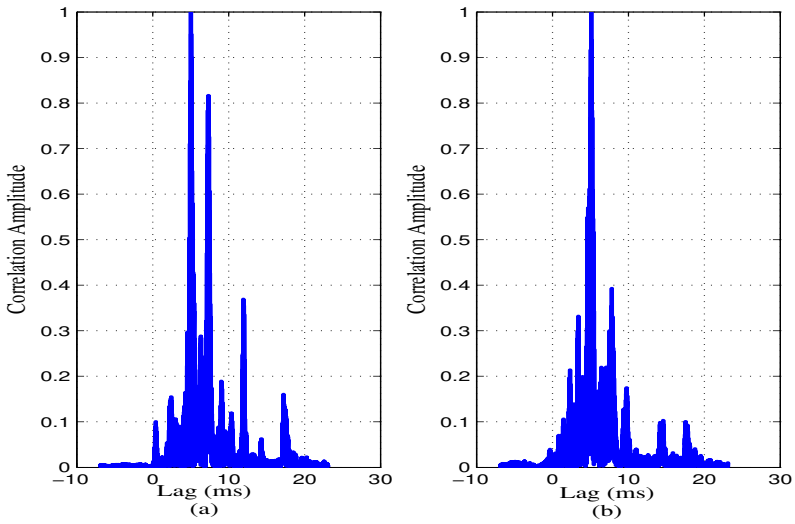

Figure 4.2. Example of normalized LFMb correlation: (a). ACDS2, (b). ACDS3.

The estimated channel impulse responses (CIRs) on ACDS2 are shown in Fig. 4.4, where the energy of each subchannel has been normalized to one. The notations 'Tx' and 'Rx' denote a transducer and a hydrophone, respectively. Obviously, the subchannels are sparse and non-minimum phase.

To demonstrate the process of turbo equalization, the estimated 8PSK symbols at the output of the FDE and the soft symbol decisions at the output of the LDPC decoder, are demonstrated in Fig. 4, where the subfigure (a) corresponds to ACDS2 and the subfigure (b) corresponds to ACDS3. Three iterations have been included for both cases. From both figures, the convergence behavior of the turbo equalization is clearly shown.

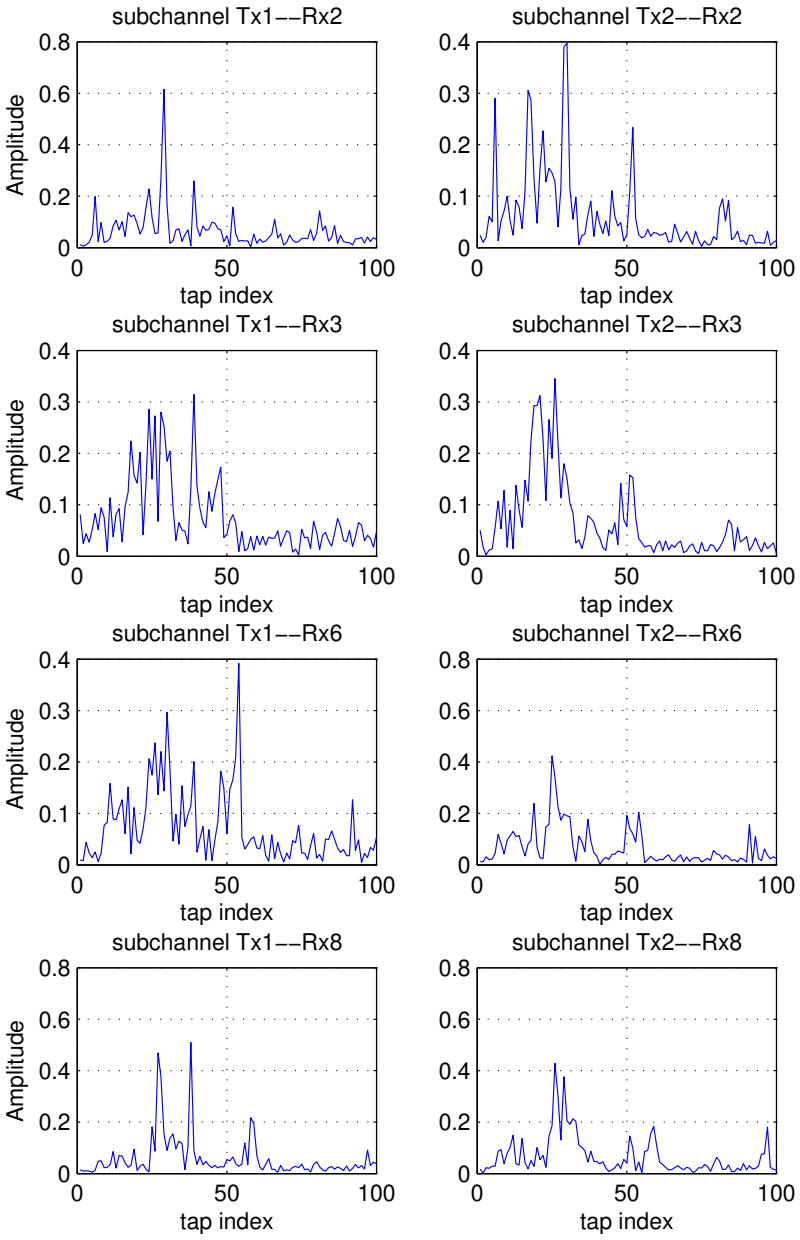

Figure 4.3. Estimated MIMO channel (ACDS2).

During the detection of each frame, the channel was periodically re-estimated with the pilot blocks of size 512 for every 5120 symbols, incurring an pilot overhead of 10%. Between two pilot blocks, the channel was updated using the decision-directed

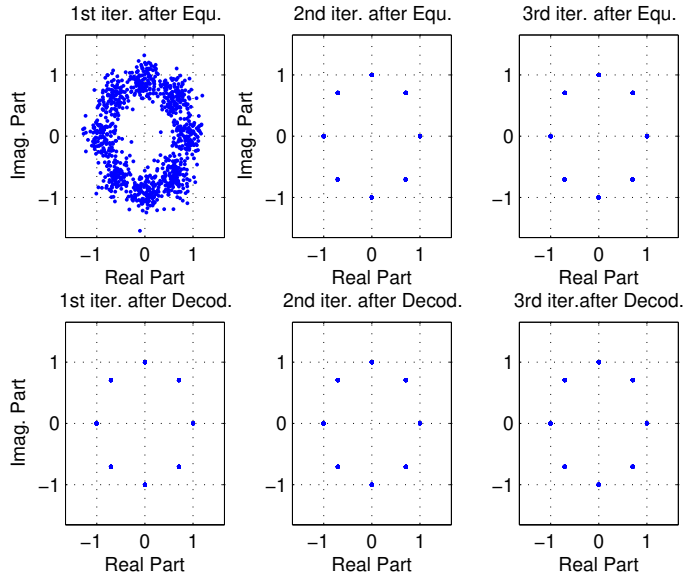

(a)

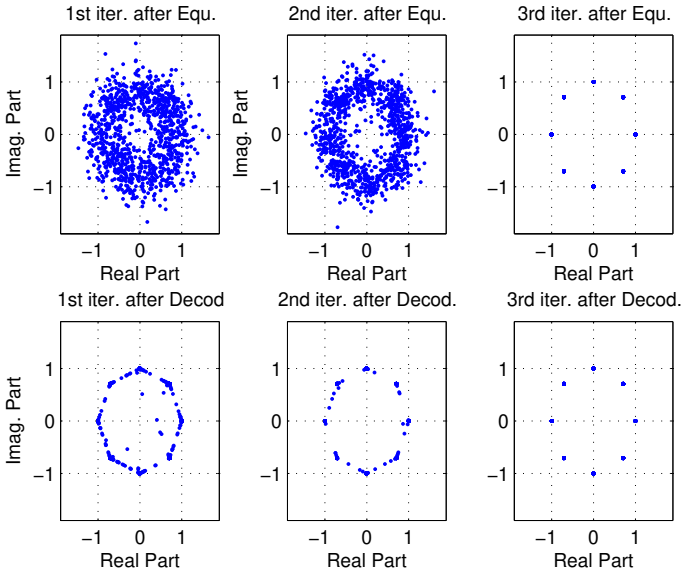

(b)

Figure 4.4. Demonstration of turbo equalization process with 8PSK modulation: (a). ACDS2, (b). ACDS3.

method. For the block partition, $N_b = 256$ or $N = 355$ (noticing $L = 100$) has been chosen for the first iteration, and $N = 256$ has been selected since the second iteration,

during the detection of all packets. The number of LDPC decoding iterations have been chosen as 15. Detection results in the form of bit error rate (BER) for ACDS2 and ACDS3, are listed in Table 4.2, where N_{iter} denotes the number of iterations for the turbo equalization. For ACDS2, 11 packets with QPSK modulation, 8 packets with 8PSK modulation, and 5 packets with 16QAM modulation are processed. For ACDS3, the number of packets are 11, 7, and 4, for the three modulations. From the table, error-free detection is achieved for two-transducer MIMO transmission with QPSK modulation. The required numbers of iterations to achieve errorless detection for ACDS2 and ACDS3 are 2 and 3, respectively. For 8PSK modulation, error-free detection and a BER as low as 10^{-6}, are obtained for ACDS2 and ACDS3, respectively, with four iterations. With a higher modulation of 16QAM, the achieved BER in the level of 10^{-4}, is still decent.

Table 4.1. Detection Results for 2×8 MIMO

Mod. \ N_{iter}		1	2	3	4
ACDS2	QPSK	1.6×10^{-4}	0	0	0
	8PSK	1.8×10^{-3}	3.1×10^{-4}	4.9×10^{-5}	0
	16QAM	3.2×10^{-3}	7.1×10^{-4}	1.7×10^{-4}	7.1×10^{-5}
ACDS3	QPSK	2.2×10^{-4}	4.4×10^{-6}	0	0
	8PSK	1.8×10^{-3}	3.9×10^{-4}	8.1×10^{-5}	2.3×10^{-6}
	16QAM	4.9×10^{-3}	6.7×10^{-4}	2.9×10^{-4}	1.1×10^{-4}

5 CONCLUSION

A frequency-domain turbo equalization scheme was proposed for no-CP single-carrier LDPC-coded MIMO UWA communications. It achieved both the low-complexity advantage of the frequency-domain equalization and the high transmission efficiency without using CP. The feasibility and the performance of the proposed scheme was tested by the field trial data measured in the ACOMM09 undersea experiment. The processing results showed that error-free detection was achieved for two-transducer MIMO transmission with QPSK modulation regardless of the different transmission ranges. With 8PSK modulation, the performance at different transmission ranges were excellent. With a 16QAM modulation, the result was still promising. In summary, the proposed scheme is a good choice for high-efficiency MIMO UWA communications.

ACKNOWLEDGMENTS

This work was supported in part by the Office of Naval Research under Grant N00014-10-1-0174 and the National Science Foundation under Grant ECCS-0846486. L. Wang is grateful to Dr. Chengshan Xiao for his helpful advice.

6 REFERENCES

[1] S. Roy, T. M. Duman, V. McDonald, and J. Proakis, "High rate communication for underwater acoustic channels using multiple transmitters and space-time coding: receiver structures and experimental results," *IEEE J. Ocean. Eng.*, vol. 32, no. 3, pp. 663-688, July, 2007.

[2] J. Tao, Y. R. Zheng, C. Xiao, T. C. Yang, "Robust MIMO underwater acoustic communications using turbo block decision-feedback equalization," *IEEE J. Ocean. Eng.*, vol. 35, no. 4, pp. 948-960, Oct. 2010.

[3] R. Otnes, T. H. Eggen, "Underwater acoustic communications: long-term test of turbo equalization in shallow water," *IEEE J. Ocean Eng.*, vol. 33, no. 3, pp. 321-334, July 2008.

[4] J. Tao, J. Wu, Y. R. Zheng, and C. Xiao, "Enhanced MIMO LMMSE turbo equalization: algorithm, simulations, and undersea experimental results," *IEEE Trans. Signal Process.*, vol. 59, no. 8, pp. 3813-3823, Aug. 2011.

[5] J. Zhang and Y. R. Zheng, "Bandwidth-efficient frequency-domain equalization for single carrier multiple-input multiple-output underwater acoustic communications," *J. Acoust. Soc. Am.*, vol. 128, pp. 2910-2919, July 2010.

[6] L. Wang, J. Tao, C. Xiao and T. C. Yang, "Low-Complexity Turbo detection for Single-Carrier MIMO Underwater Acoustic Communications," *Wireless Communications and Mobile Computing*, in press.

[7] B. Li, J. Huang, S. Zhou, K. Ball, M. Stojanovic, L. Freitag, and P. Willett, "MIMO-OFDM for high rate underwater acoustic communications," *IEEE J. Ocean Eng.*, vol. 34, no. 4, pp. 634-644, Oct. 2009.

[8] J. Huang, J.-Z. Huang, C. R. Berger, S. Zhou, and P. Willett, "Iterative sparse channel estimation and decoding for underwater MIMO-OFDM," *EURASIP Journal on Advances in Signal Processing*, vol. 2010, Article ID 460379, 11 pages, 2010.

[9] M. Tüchler, A. C. Singer, and R. Koetter, "Minimum mean squared error equalization using a priori information," *IEEE Trans. Signal Process.*, vol. 50, no. 3, pp. 673-683, March 2002.

[10] W. E. Ryan, "An Introduction to LDPC Codes," in *CRC Handbook for Coding and Signal Processing for Recording Systems* (B. Vasic, ed.), CRC Press, 2004.

III. Single-carrier frequency-domain turbo equalization without cyclic prefix or zero padding for underwater acoustic communications

Longbao Wang, Jun Tao, and Yahong Rosa Zheng

ABSTRACT—A low-complexity turbo detection scheme is proposed for single-carrier, multiple-input, multiple output (MIMO) underwater acoustic (UWA) transmission with no need to split a continuous symbol stream into blocks guarded by cyclic prefix (CP) or zero padding (ZP). The received continuous data stream is divided into consecutive blocks, with the block size determined according to the channel condition. Inter-block-interference (IBI) cancelation and CP reconstruction are applied on each partitioned block, so that the channel matrix is diagonalized in the frequency domain and the single-carrier, frequency-domain equalization technique can be used for symbol detection at a very low complexity. The IBI is removed from the current block by using the estimated channel and the detected symbols from a previous block. The CP reconstruction aims to reconstruct the signal component which would have been contributed by the CP in the received signal. Within the framework of turbo equalization, CP reconstruction is possible for a current iteration by utilizing the soft symbol estimation from a previous iteration. In the first iteration, there is no previous symbol estimation available. The frequency-domain equalization, however, can be performed in an overlapped way with a bearable loss in detection efficiency and performance. The proposed scheme achieves a high transmission efficiency without the overhead of CP, and its feasibility has been tested by field trial data measured in the ACOMM09 underwater communication experiment.

1 INTRODUCTION

High-rate underwater acoustic (UWA) communications are challenging for two main reasons [1]– [4]: first, the available channel bandwidth is very limited; second, the channel condition is very harsh. Specifically, the channel variation is rapid and the equivalent discrete-time channel length, L, is in the order of tens or even hundreds imposing high equalization complexity. Besides, Doppler effect including the Doppler shift caused by transceiver relative motion and the Doppler spread due to the water dynamics, is significant [5]. The Doppler-induced non-uniform carrier frequency offset (CFO) is undesirable for orthogonal frequency division multiplexing (OFDM) systems and must be mitigated for reliable detection.

Rapid progress has been made in different aspects for UWA communications recently [6]- [15]. In [6], [9]- [15], multiple-input, multiple output (MIMO) technology is adopted to fundamentally improve the transmission rate. In [9]- [11], frequency-domain detection techniques are used to avoid high equalization complexity. In [6]- [9], [11]- [15] turbo detection techniques are adopted to significantly improve the detection performance. In [6], turbo decision-feedback equalizer (DFE) coupled with a digital phase-locked loop (PLL) has been adopted. Turbo block DFE (BDFE) is proposed in [12], where it is shown that the BDFE outperforms the conventional DFE. In [8,14], turbo linear equalizer (LE) and an enhanced turbo LE have also been proposed. Frequency-domain turbo equalization is found in [9, 11, 15].

Transmission efficiency and detection complexity is on the opposite side of each other in conventional UWA communications. As mentioned, equalization in the time domain has a very high complexity for UWA communications. On the contrary, the frequency-domain detection has a much lower complexity which is independent of the channel length. The frequency-domain detection, however, requires a block transmission with guarding cyclic prefix (CP) or zero padding (ZP) [9, 11, 15]. CP

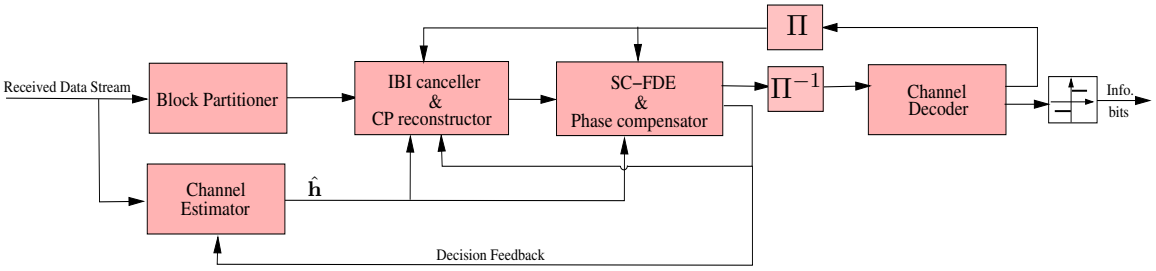

Figure 1.1. Block diagram of the proposed turbo detection scheme.

is used to avoid inter-block interference (IBI) on one hand and to make the channel matrix circular on the other hand. A circular channel matrix, once transformed into the frequency domain, will become a diagonal matrix thus the detection complexity is kept low. Since CP is a copy of the end part of a block and does not carry extra information bits, it reduces the transmission efficiency, which is critical for UWA communication due to the limited bandwidth.

In this paper, we propose to perform frequency-domain detection for UWA communications with no need to use a block transmission. Instead, the data is transmitted in continuous stream. On the receiver side, we partition the received continuous stream into consecutive blocks, and then detect each block independently. The block size, N, is determined according to the channel coherence time. Since there is no CP available, IBI arises and CP reconstruction is necessary. The IBI in a current block can be removed by utilizing the estimated channel and the estimated symbols of a previous block. The CP reconstruction is possible due to the adoption of turbo detection, for which multiple iterations are performed to detect the symbols. In the current iteration, the CP can be reconstructed with soft symbol estimations from a previous iteration. In the first iteration, there is no previous symbol estimations available. However, the frequency-domain equalization can still be performed with an overlapped block partition. In the overlapped block partition, the first $N_b = N - L + 1$ symbol vectors are actually detected while the remaining

$L-1$ symbol vectors are treated as interference and will be detected in the next block. The overlapped block partition enables frequency-domain equalization while suffers performance degradation since part of the symbols in a block are treated as interference of the remaining symbols. The performance degradation in the first iteration, however, will not affect the operation of turbo detection much since the overall detection performance will increase with the iterations. During the data processing, we notice that phase rotations exist in the equalized symbols. The phase rotation, if not properly compensated, causes a more severe problem than the loss in single-to-noise (SNR). A phase estimation and compensation operation is thus applied on the equalized symbols. Channel estimation plays a critical role for the turbo detection. We combine pilot-aided and decision-directed channel estimation methods, so as to effectively track the time variation of the UWA channel with a low training overhead.

The proposed turbo detection scheme is successfully tested by field trial data measured during an underwater acoustic communication experiment named ACOMM09, which was conducted off the coastline of New Jersey in May 2009.

Throughout this paper, $(\cdot)^T$ and $(\cdot)^H$ represent the matrix transpose and Hermitian, respectively.

2 SYSTEM DESCRIPTION

Single-carrier MIMO UWA communication with N_t transducers and N_r hydrophones, is considered. To achieve a high transmission efficiency, the data is organized in the form of frames, with a very large frame size N_f in the order of 10^4.

The k-th received sample within a frame on the m-th hydrophone is represented as follows

$$y_{m,k} = \sum_{n=1}^{N_t} \sum_{l=0}^{L-1} h_{m,n}(k,l) x_{n,k-l} + v_{m,k} \tag{1}$$

for $k = 1, 2, \cdots, N_f, N_f + 1, \cdots, N_f + L - 1$, where $x_{n,k}$ is the k-th symbol emitted from the n-th transducer, and $v_{m,k}$ is the additive noise with variance σ_v^2. The subchannel, $\{h_{m,n}(k,l)\}_{l=0}^{L-1}$, between the n-th transducer and the m-th hydrophone is treated time-varying due to the long time duration of each frame. All subchannels are assumed to have the same length L, which can be easily implemented by appending zeros at the end of the channel impulse response (CIR) if necessary.

Conventionally, the transmitted symbols, $\{x_{n,k}\ (1 \le k \le N_f)\}_{n=1}^{N_t}$, of the N_t transducers are detected from the received samples, $\{y_{m,k}\ (1 \le k \le N_f + L - 1)\}_{m=1}^{N_r}$, in the time domain. The drawback of the time-domain symbol detection technique is that its complexity increases with the channel length L. To develop a low-complexity detection scheme, we propose to divide the received frame into multiple blocks, and then detect each block independently with frequency-domain equalization technique.

The diagram of the proposed detection scheme is shown in Fig. 1.1. From the figure, a module performing IBI cancelation and CP reconstruction is inserted between the block partition module and the single-carrier, frequency-domain equalizer (SC-FDE) module. The FDE may perform phase rotation estimation and compensation for the equalized symbol. The IBI cancelation and CP reconstruction module is

critical for the proposed turbo detection scheme and will be detailed in the next section. For turbo detection, the SC-FDE is a soft-in, soft-out module which interacts with the channel decoder in an iterative way via the de-interleaver (Π^{-1})and the interleaver (Π). The outputs of the SC-FDE, the decoder, and the channel estimator, are used for IBI cancelation and CP reconstruction. The FDE output is also feedback to the channel estimator to perform decision-directed (DD) channel estimation [12,13]. In the last iteration of the turbo detection, the decision unit at the last stage of the diagram outputs the hard decisions on transmitted information bits. Details on the proposed turbo detection scheme are provided in the next section.

3 PROPOSED LOW-COMPLEXITY TURBO DETECTION

In this section, details on the low-complexity turbo detection scheme shown in Fig. 1.1 is presented. As shown in the figure, the received data stream is partitioned into blocks for detection. The choice of the block size is important for balancing the detection complexity and detection performance. If the block size is too large and its time duration exceeds the channel coherence time, the detection performance is degraded due to the channel variation. On the other hand, if the block size is too small, the overhead with IBI cancelation and CP reconstruction increases and the detection complexity is high. We select the block size based on the channel coherence time.

Block partition by itself, however, can not guarantee a low-complexity frequency-domain detection, due to the existence of IBI and the missing of CP reconstruction. The post-cursor interference of a previous block can be removed from a current block with the previously estimated symbols and the current channel knowledge. CP reconstruction is made possible in a turbo detection scheme, where the estimated symbols from a previous iteration can be used for the reconstruction. In the first iteration, there is no previous estimation available. In this case, we propose to partition the stream into overlapped blocks, so that the low-complexity detection can still be performed even without CP reconstruction, at the cost of degraded performance. The performance loss, however, does not affect the operation of the turbo detection much.

In the next two subsection, we discuss the IBI cancelation and CP reconstruction. To facilitate the discussion, we express (1) in vector form as follows

$$\mathbf{y}_k = \sum_{l=0}^{L-1} \mathbf{h}(k,l)\mathbf{x}_{k-l} + \mathbf{v}_k \tag{2}$$

where $\mathbf{y}_k = [y_{1,k}, y_{2,k}, \ldots, y_{N_r,k}]^T$, $\mathbf{x}_{k-l} = [x_{1,k-l}, x_{2,k-l}, \ldots, x_{N_t,k-l}]^T$, $\mathbf{v}_k = [v_{1,k}, v_{2,k}, \ldots, v_{N_r,k}]^T$, and

$$\mathbf{h}(k,l) = \begin{bmatrix} h_{1,1}(k,l) & \cdots & h_{1,N_t}(k,l) \\ \vdots & \ddots & \vdots \\ h_{N_r,1}(k,l) & \cdots & h_{N_r,N_t}(k,l) \end{bmatrix}. \tag{3}$$

3.1 EQUALIZATION IN THE FIRST ITERATION

For the partitioned block with index i, define

$$\mathbf{x}^i = [(\mathbf{x}_1^i)^T, (\mathbf{x}_2^i)^T, \ldots, (\mathbf{x}_N^i)^T]^T, \tag{4}$$

$$\hat{\mathbf{y}}^i = [(\hat{\mathbf{y}}_1^i)^T, (\hat{\mathbf{y}}_2^i)^T, \ldots, (\hat{\mathbf{y}}_N^i)^T]^T, \tag{5}$$

$$\hat{\mathbf{v}}^i = [(\hat{\mathbf{v}}_1^i)^T, (\hat{\mathbf{v}}_2^i)^T, \ldots, (\hat{\mathbf{v}}_N^i)^T]^T. \tag{6}$$

where it is temporarily assumed that the IBI-canceled signal $\hat{\mathbf{y}}^i$ is available. We introduce the method which enables the frequency-domain equalization without CP reconstruction. In this case, $\hat{\mathbf{y}}^i$ can be expressed as follows

$$\hat{\mathbf{y}}^i = \mathbf{h}^i \mathbf{x}^i + \mathbf{v}^i \tag{7}$$

where $\mathbf{h}^i$ is the channel matrix corresponding to the i-th block. Since the time duration of a block is short, the channel matrix is treated as time invariant over a block. The channel matrix, $\mathbf{h}^i$, possesses a block Toeplitz structure with the first column (each element is a $N_r \times N_t$ matrix) given as follows

$$\mathbf{h}_{:,1}^i = [(\mathbf{h}^i(0))^T, \cdots, (\mathbf{h}^i(L-1))^T, \mathbf{0}^T, \cdots, \mathbf{0}^T]^T \tag{8}$$

$$\underbrace{\begin{bmatrix} \hat{\mathbf{y}}_1^i \\ \hat{\mathbf{y}}_2^i \\ \vdots \\ \hat{\mathbf{y}}_N^i \end{bmatrix}}_{\hat{\mathbf{y}}^i} = \underbrace{\begin{bmatrix} \mathbf{h}(0) & 0 & \dots & \mathbf{h}(L-1) & \dots & \dots & \mathbf{h}(1) \\ \mathbf{h}(1) & \mathbf{h}(0) & 0 & \dots & \mathbf{h}(L-1) & \dots & \mathbf{h}(2) \\ \vdots & \ddots & \ddots & \ddots & \ddots & \ddots & \vdots \\ \mathbf{h}(L-1) & \dots & \mathbf{h}(0) & 0 & 0 & \dots & 0 \\ \vdots & \ddots & \ddots & \ddots & \ddots & \ddots & \vdots \\ 0 & \dots & 0 & \mathbf{h}(L-1) & \dots & \mathbf{h}(1) & \mathbf{h}(0) \end{bmatrix}}_{\mathbf{h}_{\text{cir}}^i} \times \underbrace{\begin{bmatrix} \mathbf{x}_1^i \\ \mathbf{x}_2^i \\ \vdots \\ \mathbf{x}_{N_b}^i \\ \mathbf{0}_{N_r(L-1)\times 1} \end{bmatrix}}_{\tilde{\mathbf{x}}^i} + \mathbf{h}^i \underbrace{\begin{bmatrix} \mathbf{0}_{N_r N_b \times 1} \\ \mathbf{x}_{N_b+1}^i \\ \mathbf{x}_{N_b+2}^i \\ \vdots \\ \mathbf{x}_N^i \end{bmatrix}}_{\mathbf{w}^i} + \mathbf{v}^i. \tag{9}$$

where the time index k has been dropped and each zero matrix having a size of $N_r \times N_t$.

Without CP reconstruction, the channel matrix $\mathbf{h}^i$ is not circular, thus can not be diagonalized via discrete Fourier transform (DFT). To achieve a low-complexity detection, we decompose $\mathbf{h}^i\mathbf{x}^i$ in (7) into two parts: $\mathbf{h}_{\text{cir}}^i\tilde{\mathbf{x}}^i$ and $\mathbf{h}^i\breve{\mathbf{x}}^i$, and rewrite (7) as (9) at the top of the next page. The block index i has been dropped from the elements in $\mathbf{h}_{cir}^i$ for concise purpose. From (9), when $\mathbf{h}^i\breve{\mathbf{x}}^i$ is treated as an interference term, we are able to detect $\tilde{\mathbf{x}}^i$ via low-complexity frequency-domain equalization since $\mathbf{h}_{\text{cir}}^i$ is a block circular channel matrix.

Based on (9), $\tilde{\mathbf{x}}^i$ is detected. In other words, the first $N_b = N - L + 1$ symbol vectors of $\mathbf{x}^i$ is actually detected. The remaining $L-1$ symbol vectors $\mathbf{x}_{N_b+1}^i, \cdots, \mathbf{x}_N^i$ have been treated as interference component in $\mathbf{w}^i$. Therefore, low-complexity detection without CP reconstruction at the first iteration is achieved at the cost of detection efficiency and also some performance degradation. The block partition in

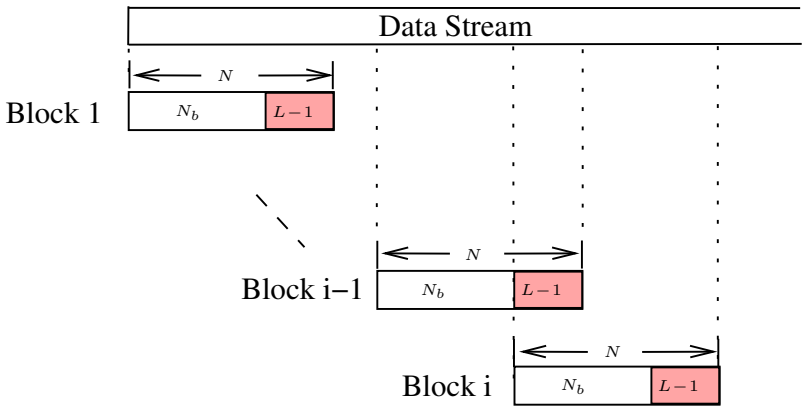

Figure 3.1. Block partition in the first iteration.

the first iteration is demonstrated in Fig. 3.1, where block i overlaps with block $i-1$ for $L-1$ symbols.

From Fig. 3.1, the IBI cancelation is performed as follows

$$\hat{\mathbf{y}}_k^i = \begin{cases} \mathbf{y}_k^i - \sum_{l=k}^{L-1} \hat{\mathbf{h}}^i(l)\check{\mathbf{x}}_{N_b-L+1+l}^{i-1} & k = 1, \ldots, L-1, \\ \mathbf{y}_k^i & k = L, \ldots, N. \end{cases} \tag{10}$$

where $\hat{\mathbf{h}}^i(l)$ is the estimated channel for the i-th block, and $\check{\mathbf{x}}_k^{i-1}$ is the k-th hard-decision symbol vector of the previous block with index $i-1$.

To perform the low-complexity detection, (9) is transformed into frequency domain by applying a size-N normalized DFT matrix, $\mathbf{F}_N$, on both sides. The frequency-domain model is given as

$$\hat{\mathbf{Y}}^i = \mathbf{H}^i\tilde{\mathbf{X}}^i + \mathbf{W}^i \tag{11}$$

where $\hat{\mathbf{Y}}^i = \mathbf{F}_N\hat{\mathbf{y}}^i$, $\tilde{\mathbf{X}}^i = \mathbf{F}_N\tilde{\mathbf{x}}^i$, $\mathbf{W}^i = \mathbf{F}_N\mathbf{w}^i$, and $\mathbf{H}^i = \mathbf{F}_N\mathbf{h}_{\text{cir}}^i\mathbf{F}_N^h$. The frequency-domain symbol vector $\tilde{\mathbf{X}}^i$ is estimated then transformed back into its time-domain counterpart inside the soft-in, soft-out FDE. Details are referred to [15]. Due to the

Doppler spread in UWA communications, the equalized symbols suffer phase rotations [13], so we perform phase estimation and compensation after the equalization. Significant performance gain can be achieved with the phase estimation and compensation operation. The soft output of the SC-FDE is computed with the phase-compensated symbol estimations. Details can be referred to [15, 16].

The channel decoder takes as input the soft output of the SC-FDE and feeds back new soft information to the SC-FDE for the next iteration.

3.2 EQUALIZATION IN THE SECOND ITERATION AND BEYOND

For the second iteration and beyond, the soft output in a previous iteration from the channel decoder is available for the SC-FDE. The soft feedback is usually in the form of log-likelihood ratio (LLR), with which the *a priori* probability, $P(x^i_{n,k} = \alpha)$, of a symbol, $x^i_{n,k}$, can be computed [16]. The value α is taken from the constellation set $\mathcal{S}$. With $P(x^i_{n,k} = \alpha)$, the *a priori* symbol estimation is computed as follows

$$\bar{x}^i_{n,k} = \sum_{\alpha \in \mathcal{S}} \alpha \cdot P(x^i_{n,k} = \alpha). \tag{12}$$

The soft symbol estimations can be used for CP reconstruction. Temporarily assuming that the IBI-canceled received signal $\hat{\mathbf{y}}^i$ is available, the CP reconstruction is performed as follows

$$\tilde{\mathbf{y}}^i_k = \begin{cases} \hat{\mathbf{y}}^i_k + \sum_{l=k}^{L-1} \mathbf{h}^i(l) \bar{\mathbf{x}}^i_{N+1-l} & k = 1, 2, \ldots, L-1, \\ \hat{\mathbf{y}}^i_k & k = L, \ldots, N. \end{cases} \tag{13}$$

where $\bar{\mathbf{x}}_k^i = [\bar{x}_{1,k}^i, \bar{x}_{2,k}^i, \ldots, \bar{x}_{N_t,k}^i]^T$ is the *a priori* soft symbol estimation vector. After CP reconstruction, the vector $\tilde{\mathbf{y}}^i$ is given as below

$$\tilde{\mathbf{y}}^i \approx \mathbf{h}_{\text{cir}}^i \mathbf{x}^i + \mathbf{v}^i \tag{14}$$

where approximation is used since there exists estimation error in $\bar{\mathbf{x}}_k^i$. The model in (14), is ready for low-complexity detection. It is noted that, the accuracy of $\bar{\mathbf{x}}_k^i$ increases with the iterations, so the detection with (14) approaches that for a block transmission with CP.

The IBI cancelation for the second iteration and beyond is similar to the first iteration, as shown in (10), except that the N_b in the subscript of $\check{\mathbf{x}}^{i-1}$ shall be changed to N. In other words, there is no need for overlapped block partition thus no loss in the detection efficiency since the second iteration, attributed to the CP reconstruction.

3.3 CHANNEL DECODING

A binary low-density parity-check (LDPC) channel code with coding rate 1/2 has been used in the ACOMM09 experiment. The codeword length can be 1024, 2048, or 4096. The decoding is performed with the log-domain Sum-Product Algorithm (SPA) proposed in [17]. Details are omitted here for brevity.

4 EXPERIMENTAL RESULTS

Single-carrier underwater communication experiment named ACOMM09, was conducted off the coastline of New Jersey in May 2009. The transmitter is a two-transducer array. On the transmitter side, bit-interleaved coded modulation (BICM) was used in the time domain and multiplexing was used in the space domain. A random interleaver was adopted, and the channel decoder is a rate 1/2 LDPC code. Different modulations of QPSK, 8PSK, and 16QAM were used. The transmission rate for a single transducer was 5 kilo symbols per second (ksps), and the carrier frequency was $f_c = 17$ kHz. Two set of receivers named ACDS2 and ACDS3, were deployed. Each receiver consisted of eight hydrophones with inter-hydrophone spacing being 2.06 m. The ACDS2 and ACDS3 were 2 km and 3 km away from the transmitter, respectively. Fixed communications with no transceiver relative motion, were launched.

In a filed trial transmission, the frames are combined with auxiliary signaling like linear frequency modulation (LFM) sequences and m-sequence, which are used for synchronization and channel probing [12]. We name the combined transmission entity as a packet. The structure of a transmitted packet in the ACOMM09 experiment, is shown in Fig. 4.1. From the figure, two frames are transmitted within one packet.

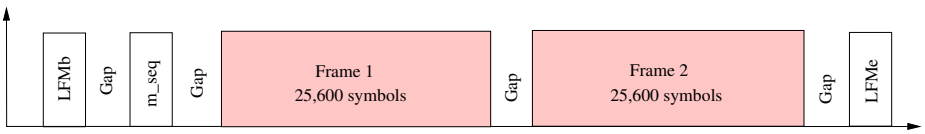

Figure 4.1. Packet structure for ACOMM09.

The frame size is $N_f = 25,600$, which is much larger than the block size used in a block transmission using CP [9,11,15]. Two LFM sequences named LFMb and LFMe

are padded at the head and tail of the packet. The two LFM sequences, each can be used for packet synchronization and can also be used simultaneously for measuring Doppler shift [13]. The m-sequence can be used for probing the scattering function of the channel [13].

During the experiment, the received packets were recorded in files for offline detection. In Fig. 4.2, the power spectrum of a recorded packet is plotted. A passband filtering has been applied on the time-domain signal so the spectrum curve is very smooth. It is clear the signal frequency component centers at the carrier frequency $f_c = 17$ kHz, and spans a range larger than 5 kHz due to the excess bandwidth of the pulse shaping filter.

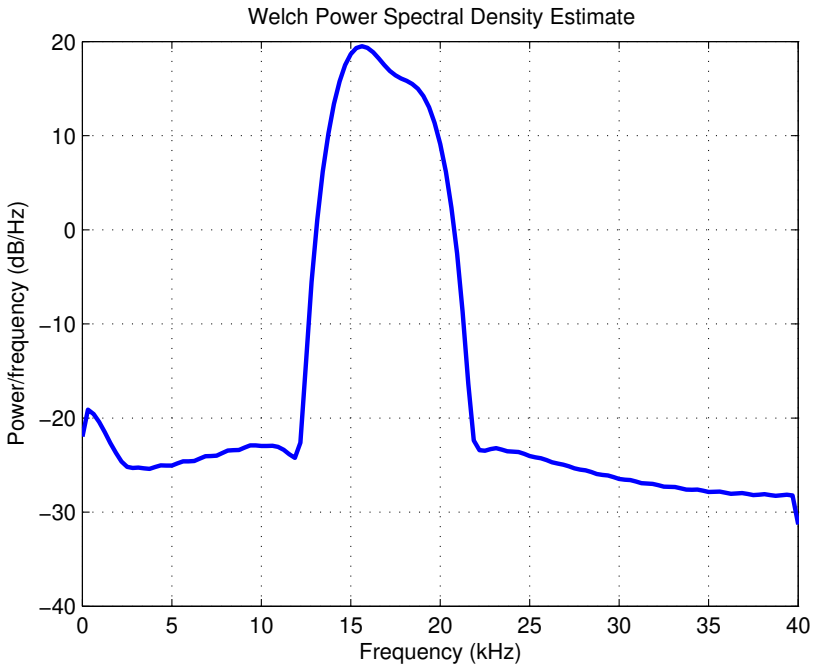

Figure 4.2. Power spectrum of a received packet.

Before a packet can be detected, synchronization is necessary. Synchronization is achieved by correlating the received packet with a local LFM reference sequence and

then locating the correlation peak. The correlation span also indicates the channel length. In Fig. 4.3, examples of the normalized LFM correlations for the ACDS2 and ACDS3 are respectively shown. In both subfigures, correlation peak can be easily observed and the span of the LFM correlation is about 20 ms which corresponds to a channel length of $L \approx \frac{20 \text{ ms}}{T_s} = 100$ in terms of the symbol period. The symbol period T_s is equal to 0.2 ms since the symbol rate is 5 ksps. The correlation peak is in the middle of the correlation span, so the CIRs are non-minimum phase.

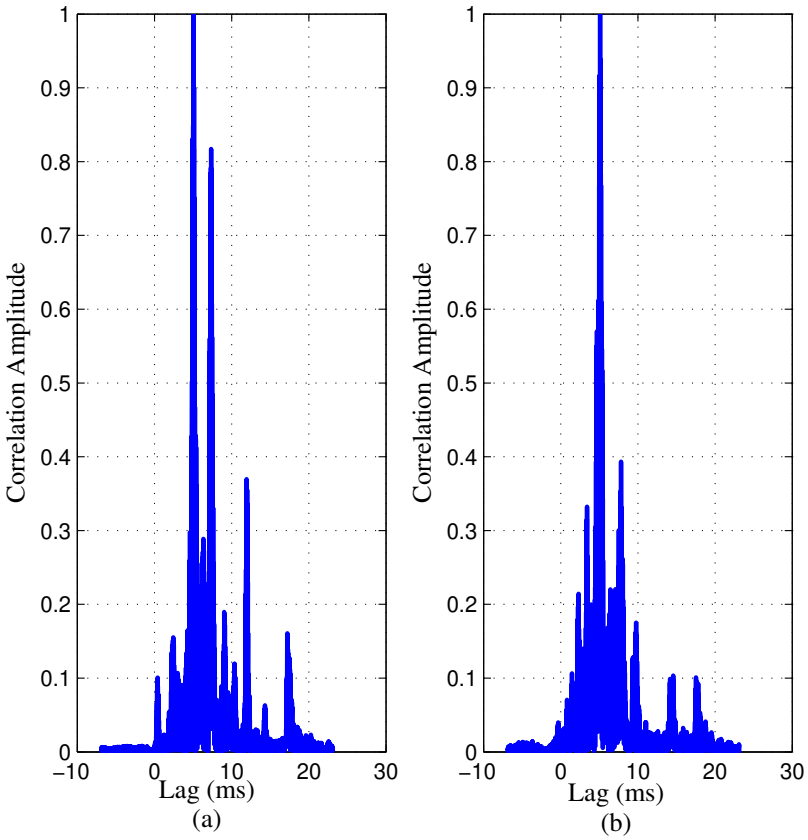

Figure 4.3. Examples of normalized LFMb correlations: (a). ACDS2, (b). ACDS3.

After synchronization, channel estimation is performed before equalization. The estimated MIMO channel for ACDS2 is shown in Fig. 4.4, where the energy of

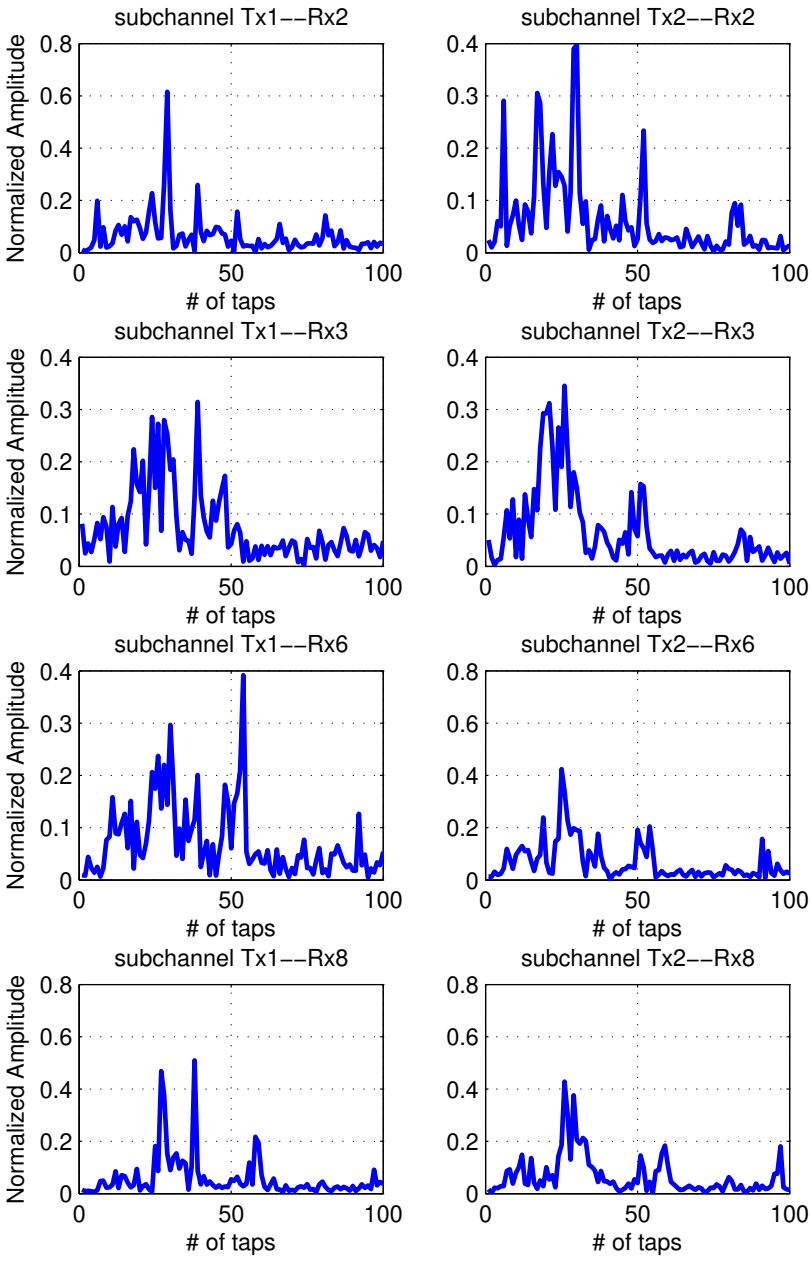

Figure 4.4. Estimated MIMO channel (ACDS2).

each subchannel has been normalized to one. The notations 'Tx' and 'Rx' denote a transducer and a hydrophone, respectively. Obviously, the subchannels are sparse and non-minimum phase, which is consistent with the observations in Fig. 4.3. In Fig. 4.5,

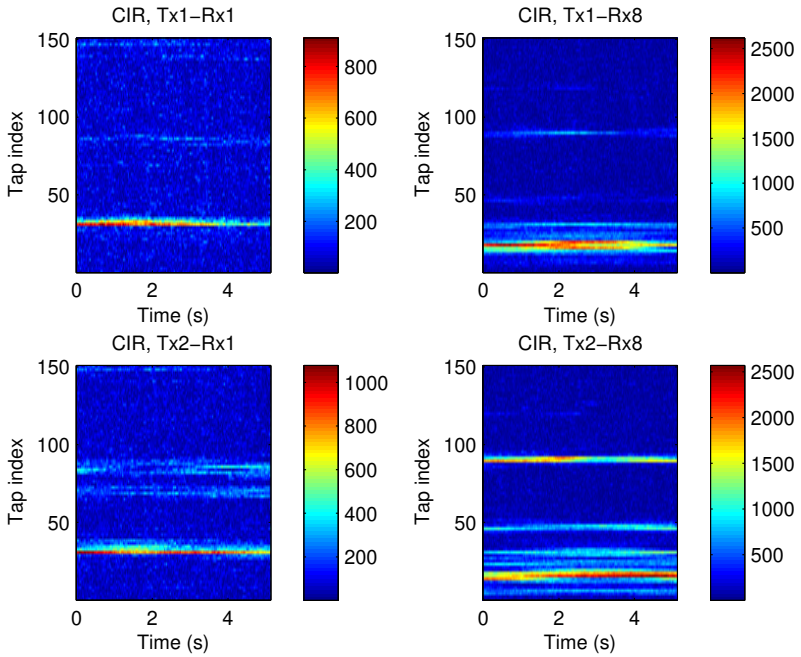

Figure 4.5. Demonstration of channel time variation within one frame.

the sequence of estimated channels of different blocks within a frame is demonstrated. For comparison purpose, the channel energy is not normalized. It is obvious that the channel varies over one frame.

As shown in [13], Doppler-spread-caused phase rotation exists in the equalized symbols for UWA communications, especially when the block size is large. A phase estimation and correction method for PSK modulation, is referred to [13]. In this paper, we also propose a phase estimation and compensation method for 16QAM modulation. For an equalized block with index i, the mean power of the estimated symbols corresponding to the n-th transducer is computed as follows

$$\varepsilon_n = \frac{1}{N_b} \sum_{k=1}^{N_b} |\hat{x}_{n,k}^i|^2 \tag{15}$$

Then, those equalized symbols with a modulus in the range $[1.1708\sqrt{\varepsilon_n}, 1.5125\sqrt{\varepsilon_n}]$ are selected for phase rotation estimation. The reason for selecting estimated symbols

with a large power is that they are less sensitive to additive noise. The idea for phase rotation estimation is to find the average difference between the phases of those selected symbol estimations and the phases of their hard-decision counterparts. The estimated phase rotation is then used for compensating all estimated symbols within a block. It is noted that the phase rotation estimation and compensation is performed for each transducer independently, since symbols from different transducer may undergo different phase corruption. In Fig. 4.6, an example of phase rotation estimation and compensation is shown. In the left subfigure, the phase rotation in the equalized symbols are clearly shown. The selected symbols for phase rotation estimation fall into the region between the two circles, and the four red dots (A, B, C, D) represent the hard decisions for those selected symbols. The phase-corrected symbol estimations are shown in the right subfigure.

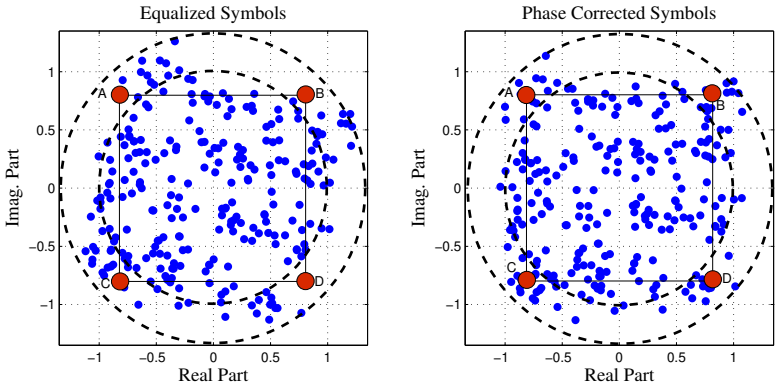

Figure 4.6. Demonstration of phase rotate estimation and compensation with 16QAM modulation.

The detection gain obtained from the phase compensation (PC) could be significant. In Table 4.1, detection results with and without phase compensation is listed for both ACDS2 and ACDS3. The result with 16QAM modulation is shown. Five packets are detected for ACDS2, and four packets are detected for ACDS3. The

N_{iter} in the table denotes the number of iterations for the turbo equalization. From the table, using PC consistently improves the performance. For packet 1 of either receiver, the error numbers are dramatically reduced and the performance increases with iterations by using PC. On the contrary, the results totally do not makes sense without using PC.

Before the experimental results are presented, we show the turbo detection process by scatter plotting the symbol estimations at the output of the soft-in, soft-out FDE and the LDPC channel decoder over multiple iterations. In Fig. 4.7, the 8PSK symbol estimations are demonstrated for ACDS2. Obviously, the symbol detection

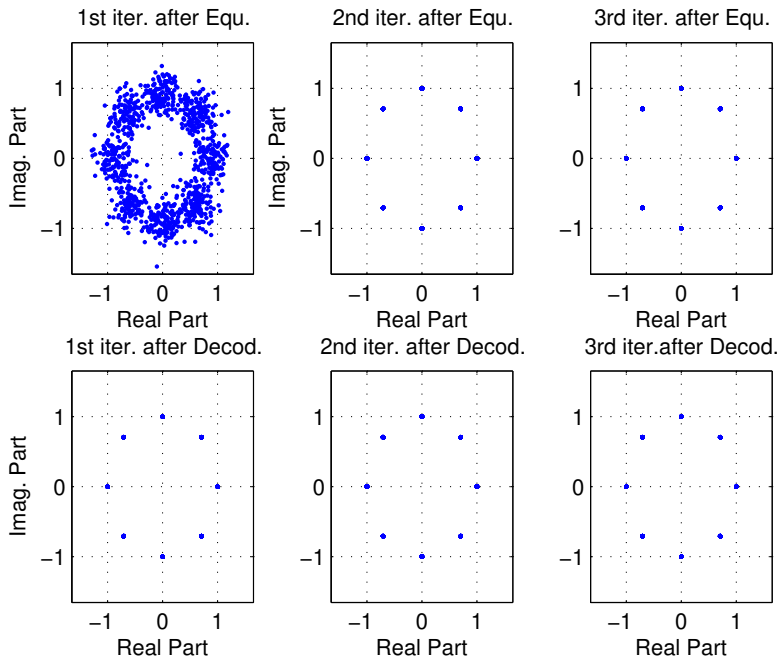

Figure 4.7. Demonstration of turbo equalization with 8PSK modulation (ACDS2).

at the output of the decoder is nearly perfect in the first iteration. In the second iteration, the output of the soft-in, soft-out FDE has no errors. The results for ACDS3 is shown in Fig. 4.8, where error-free detection is obtained in the third iteration. Both

Table 4.1. Number of Error Bits for 2×8 MIMO with 16QAM Modulation

	Packet index \ N_{iter}		1	2	3	4
ACDS2	1	With PC	421	97	27	10
		Without PC	64425	70470	73186	74641
	2	With PC	365	86	26	13
		Without PC	2574	1754	897	874
	3	With PC	314	59	9	4
		Without PC	1578	2547	3658	5987
	4	With PC	197	47	7	2
		Without PC	275	124	21	14
	5	With PC	0	0	0	0
		Without PC	356	117	57	31
	Packet index \ N_{iter}		1	2	3	4
ACDS3	1	With PC	645	87	37	10
		Without PC	58741	69541	71548	75412
	2	With PC	541	76	31	13
		Without PC	4412	5472	5874	6587
	3	With PC	361	55	27	12
		Without PC	1578	2547	3658	5987
	4	With PC	50	0	0	0
		Without PC	55	1	1	1

results have verified the powerful detection capability of turbo equalization. The results with 16QAM modulation is also included in Fig. 4.9 and Fig. 4.10 for the two receivers. The observations are similar to 8PSK case.

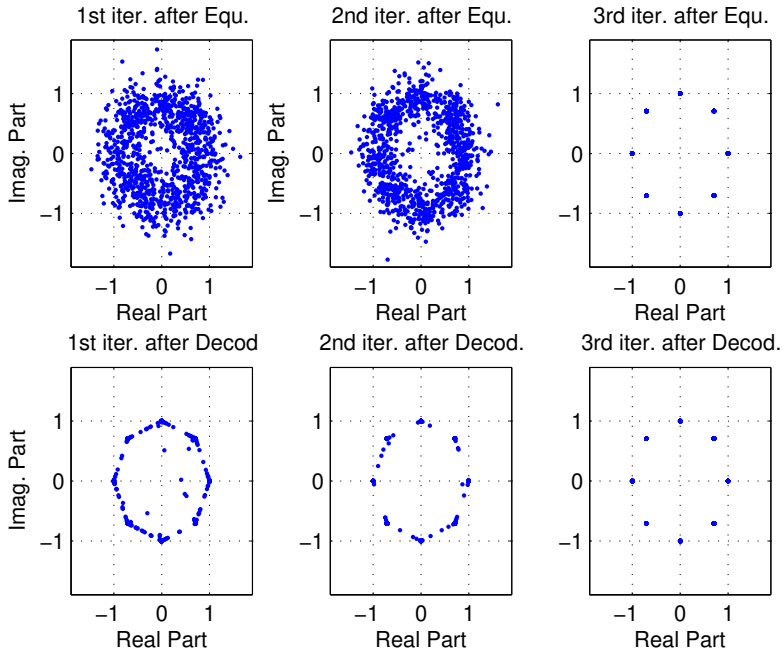

Figure 4.8. Demonstration of turbo equalization with 8PSK modulation (ACDS3).

For each frame, pilot blocks of size 512 are inserted periodically for every 5120 symbols. In total, there are five pilot blocks within each frame, resulting in a pilot overhead of 10%. The pilot block provides an initial channel estimation for detecting the first partitioned block following it, and decision-directed channel estimation is used for detecting remaining partitioned blocks. During the packet detection, the number of LDPC decoding iterations has been chosen as 15.

For ACDS2, 11 packets with QPSK modulation, 8 packets with 8PSK modulation, and 5 packets with 16QAM modulation are processed. For ACDS3, the number of detected packets are 11, 7, and 4, corresponding to the three modulations. By resorting to the channel scattering function estimated with the m-sequence [13], we find the channel coherence time as $T_c \approx 125$ ms, corresponding to a Doppler spread over the range $[-4, 4]$ Hz. Based on the channel coherence time, three different partition block sizes: $N = 227$, $N = 355$, and $N = 611$ (or $N_b = 128$, $N_b = 256$, and

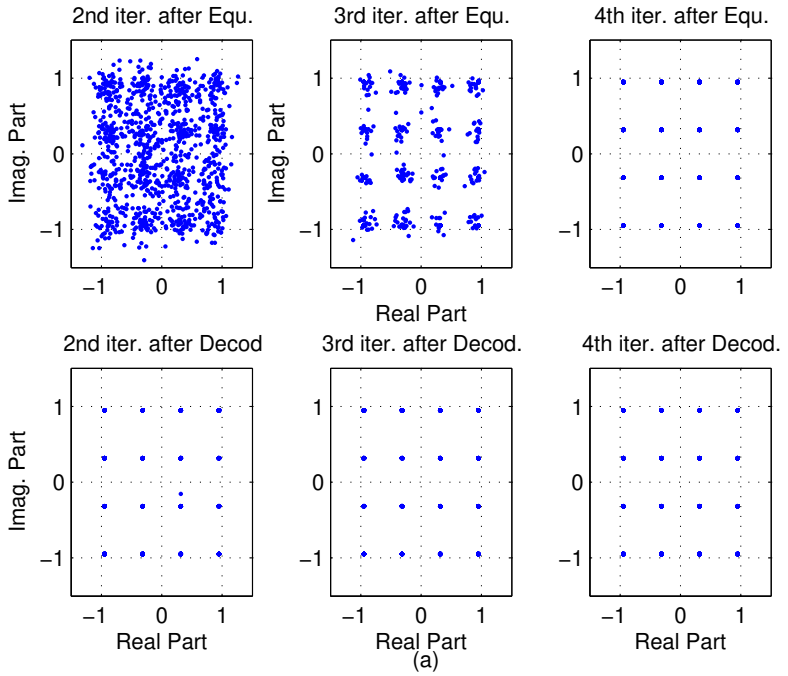

Figure 4.9. Demonstration of turbo equalization with 16QAM modulation (ACDS2).

$N_b = 512$), are chosen. The corresponding block time durations are 45.4 ms, 71 ms, and 122.2 ms. The bit error rate (BER) is used as a performance metric. The results with the three differnet partition block sizes are listed in Table 4.2 to Table 4.4.

From the tables, error-free detection can be obtained for QPSK modulation despite of the value of N_b, for both ACDS2 and ACDS3. Two or three iterations are sufficient for error-free detection. With 8PSK modulation, the ACDS2 achieves error-free detection when $N_b = 128$ and $N_b = 256$, and has a BER level of 10^{-4} with $N_b = 512$. The performance of ACDS3 is not as good as ACDS2, and error-free detection is not available regardless of the partitioned block size. With N_b equal to 128 or 256, the BER level is 10^{-6}. With N_b equal to 512, the BER level is 10^{-4}. For the 16QAM modulation, error-free detection is not achieved in all cases. The BER level ranges from 10^{-3} to 10^{-5} for ACDS2 and ACDS3. Based on all above observations, we drawn the following conclusions: first, using a smaller partitioning

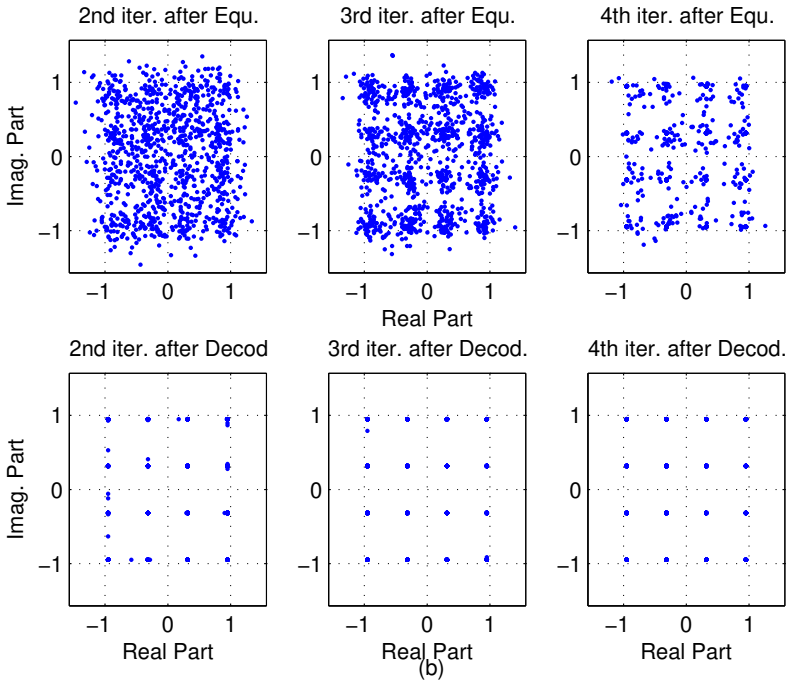

Figure 4.10. Demonstration of turbo equalization with 16QAM modulation (ACDS3).

block size corresponds to a higher detection performance. However, the detection efficiency is lower and the detection complexity is higher. Second, the performance decreases with the increase of the constellation size, which is as expected. Last, the overall performance of ACDS2 with a transmission range of 2 km is better than that of ACDS3 with a transmission range of 3 km.

Table 4.2. Detection Results for 2×8 MIMO, $N_b = 128$

Mod. \ N_{iter}		1	2	3	4
ACDS2	QPSK	6.2×10^{-5}	0	0	0
	8PSK	3.6×10^{-4}	1.8×10^{-4}	2.6×10^{-5}	0
	16QAM	1.8×10^{-3}	3.2×10^{-4}	1.4×10^{-5}	5.6×10^{-5}
ACDS3	QPSK	1.0×10^{-4}	0	0	0
	8PSK	4.4×10^{-4}	2.1×10^{-4}	4.4×10^{-5}	2.3×10^{-6}
	16QAM	3.0×10^{-3}	4.4×10^{-4}	2.3×10^{-5}	8.9×10^{-5}

Table 4.3. Detection Results for 2×8 MIMO, $N_b = 256$

Mod. \ N_{iter}		1	2	3	4
ACDS2	QPSK	1.6×10^{-4}	0	0	0
	8PSK	1.8×10^{-3}	3.1×10^{-4}	4.9×10^{-5}	0
	16QAM	3.2×10^{-3}	7.1×10^{-4}	1.7×10^{-4}	7.1×10^{-5}
ACDS3	QPSK	2.2×10^{-4}	4.4×10^{-6}	0	0
	8PSK	1.8×10^{-3}	3.9×10^{-4}	8.1×10^{-5}	2.3×10^{-6}
	16QAM	4.9×10^{-3}	6.7×10^{-4}	2.9×10^{-4}	1.1×10^{-4}

Table 4.4. Detection Results for 2×8 MIMO, $N_b = 512$

Mod. \ $N_{\text{iter.}}$		1	2	3	4
ACDS2	QPSK	2.8×10^{-4}	6.7×10^{-6}	0	0
	8PSK	1.1×10^{-2}	1.4×10^{-3}	2.5×10^{-4}	2.5×10^{-4}
	16QAM	2.5×10^{-2}	6.0×10^{-3}	6.3×10^{-4}	6.1×10^{-4}
ACDS3	QPSK	3.2×10^{-4}	1.8×10^{-5}	0	0
	8PSK	1.5×10^{-2}	1.8×10^{-3}	3.8×10^{-4}	3.8×10^{-4}
	16QAM	3.4×10^{-2}	8.1×10^{-3}	9.9×10^{-4}	9.8×10^{-4}

5 CONCLUSION

Low-complexity turbo detection for single-carrier MIMO UWA communication was proposed. Compared with conventional low-complexity frequency-domain detection, operation of the proposed scheme did not enforce a block transmission with CP, thus a high transmission efficiency was achieved. The proposed scheme partitioned the received continuous stream into blocks, and detected each block in the frequency domain by relying on IBI cancelation and CP reconstruction. To mitigate the phase rotation in the equalized symbols, a phase rotation estimation and compensation method was introduced and significantly improved the detection performance. The proposed low-complexity scheme was tested by field trial data measured in the ACOMM09 undersea communication experiment. Detection results showed a consistently good detection performance of the proposed scheme.

6 REFERENCES

[1] M. Stojanovic, J. Catipovic, and J. Proakis, "Phase-coherent digital communicaitons for underwater acoustic channels," *IEEE J. Ocean Eng.*, vol. 19, no. 1, pp.100-111, Jan. 1994.

[2] D. B. Kilfoyle and A. B. Baggeroer, "The state of the art in underwater acoustic telemetry," *IEEE J. Ocean Eng.*, vol. 25, no. 1, pp. 4-27, Jan. 2000.

[3] T. C. Yang, "Correlation-based decision-feedback equalizer for underwater acoustic communications," *IEEE J. Ocean Eng.*, vol. 30, no. 4, pp. 865-880, Oct. 2005.

[4] H. C. Song, P. Roux, W. S. Hodgkiss, W. A. Kuperman, T. Akai, and M. Stevenson, "Multiple-input-multiple-output coherent time reversal communications in a shallow-water acoustic channel," *IEEE J. Ocean. Eng.*, vol. 31, no. 1, pp. 170-187, Jan. 2006.

[5] B. S. Sharif, J. Neasham, O. R. Hinton, and A. E. Adams, "A computationally efficient Doppler compensation system for underwater acoustic communications," *IEEE J. Ocean Eng.*, vol. 25, no. 1, pp. 52-61, Jan. 2000.

[6] S. Roy, T. M. Duman, V. McDonald, and J. Proakis, "High rate communication for underwater acoustic channels using multiple transmitters and space-time coding: receiver structures and experimental results," *IEEE J. Ocean. Eng.*, vol. 32, no. 3, pp. 663-688, July, 2007.

[7] J. F. Sifferlen, H. C. Song, W. S. Hodgkiss, W. A. Kuperman, and J. M. Stevenson, "An iterative equalization and decoding approach for underwater acoustic communication," *IEEE J. Ocean Eng.*, vol. 33, no. 2, pp. 182-197, April 2008.

[8] R. Otnes and T. H. Eggen, "Underwater acoustic communications: long-term test of turbo equalization in shallow water," *IEEE J. Ocean Eng.*, vol. 33, no. 3, pp. 321-334, July 2008.

[9] B. Li, J. Huang, S. Zhou, K. Ball, M. Stojanovic, L. Freitag, and P. Willett, "MIMO-OFDM for high rate underwater acoustic communications," *IEEE J. Ocean Eng.*, vol. 34, no. 4, pp. 634-644, Oct. 2009.

[10] J. Zhang and Y. R. Zheng, "Bandwidth-efficient frequency-domain equalization for single carrier multiple-input multiple-output underwater acoustic communications," *J. Acoust. Soc. Am.*, vol. 128, pp. 2910-2919, July 2010.

[11] J. Huang, J.-Z. Huang, C. R. Berger, S. Zhou, and P. Willett, "Iterative sparse channel estimation and decoding for underwater MIMO-OFDM," *EURASIP Journal on Advances in Signal Processing*, vol. 2010, Article ID 460379, 11 pages, 2010.

[12] J. Tao, Y. R. Zheng, C. Xiao, T. C. Yang, "Robust MIMO underwater acoustic communications using turbo block decision-feedback equalization," *IEEE J. Ocean. Eng.*, vol. 35, no. 4, pp. 948-960, Oct. 2010.

[13] J. Tao, Y. R. Zheng, C. Xiao, T. C. Yang, and W. B. Yang, "Channel equalization for single carrier MIMO underwater acoustic communications," *EURASIP Journal on Advances in Signal Processing*, vol. 2010, Article ID 281769, 17 pages, 2010. doi:10.1155/2010/281769.

[14] J. Tao, J. Wu, Y. R. Zheng, and C. Xiao, "Enhanced MIMO LMMSE turbo equalization: algorithm, simulations, and undersea experimental results," *IEEE Trans. Signal Process.*, vol. 59, no. 8, pp. 3813-3823, Aug. 2011.

[15] L. Wang, J. Tao, C. Xiao, and T. C. Yang, "Low-Complexity Turbo detection for Single-Carrier MIMO Underwater Acoustic Communications," *Wireless Communications and Mobile Computing*, in press.

[16] M. Tüchler, A. C. Singer, and R. Koetter, "Minimum mean squared error equalization using a priori information," *IEEE Trans. Signal Process.*, vol. 50, no. 3, pp. 673-683, March 2002.

[17] W. E. Ryan, "An Introduction to LDPC Codes," in *CRC Handbook for Coding and Signal Processing for Recording Systems* (B. Vasic, ed.), CRC Press, 2004.

IV. Low Complexity Soft-Interference Cancelation Turbo Equalization for MIMO Systems with Multilevel Modulations

Jingxian Wu, Longbao Wang, and Chengshan Xiao

ABSTRACT—This paper presents a low complexity soft-interference cancellation equalizer (SICE) for the turbo detection of multiple-input multiple-output (MIMO) systems operating in time dispersive channels. The SICE contains three time-invariant linear filters: a feedforward filter, a causal feedback filter and an anti-causal feedback filter. The feedforward filter is designed to suppress the intersymbol interference (ISI) due to time dispersive channels and the multiplexing interference from multiple transmit antennas. The causal (or anti-causal) feedback filter is developed to remove the residual interference caused by the symbols transmitted before (or after) the symbol under detection. The performance of the proposed SICE is verified through both extrinsic information transfer chart (EXIT) analysis and computer simulations. The analytical and simulation results demonstrated that the inclusion of the anti-causal soft decision during SICE is critical to the system performance. The EXIT chart analysis shows that the SICE performance approaches the ideal matched filter bound as the iteration progresses.

1 INTRODUCTION

The constantly increasing demands for broadband high data rate communications necessitate the development of advanced communication transceivers that can aggressively reuse the space, time, and/or frequency resources. This usually results in severe interferences to the signals, such as multiplexing interference (MI) due to spatial multiplexing and intersymbol interference (ISI) due to channel time dispersion. There are a wealth of works in the literature devoted to detection techniques that can combat the negative impacts of MI and/or ISI through equalization and interference cancellation.

Many detection techniques follow the structure of a turbo equalizer [2]- [4], where a soft-input soft-output (SISO) equalizer iteratively exchanges soft information with a SISO channel decoder, separated by an interleaver. A large number of low complexity SISO equalizers have been proposed to tradeoff the complexity with performance. Decision feedback equalization (DFE) with either hard decisions [5] or soft decisions [6, 7] were proposed for turbo equalization. Many of the DFE filter coefficients are derived by using the assumption of perfect interference cancellation, which is usually not the case in practical systems. In [8], a soft feedback equalizer (SFE) is developed for binary modulated systems without the assumption of perfect interference cancellation, and it was later extended to systems with high level modulations [9]. All above works are developed for single-input single-output systems.

Most DFE algorithms perform interference cancellation only over the causal symbols, which are the symbols transmitted before the current symbol under detection [9]- [11]. However, the linear filtering will introduce residual interference from anti-casual symbols, or the symbols transmitted after the current symbol. For systems with high level modulations, the interference from anti-causal symbols becomes a serious performance limiting factor. It will be shown in this paper that ignoring the

anti-causal interference results in a non-diminishing performance gap between the soft decision feedback equalizer (SDFE) [9] and the systems with ideal interference cancellations.

In this paper, we propose a new low complexity soft interference cancellation equalizer for multiple-input multiple-output (MIMO) systems with high level modulations. The proposed SICE performs soft interference cancellation over both causal symbols and anti-causal symbols to close the performance gap with ideal interference cancellations. The SIC of the anti-causal symbols is enabled by the iterative structure, where the anti-causal soft decisions are calculated by utilizing the *a priori* soft input from the previous iteration. The inclusion of the anti-causal SIC is critical to the system performance. In addition, the coefficients of the SICE filters are calculated by analyzing the statistical properties of the causal and anti-causal soft decisions, and the filter development does not require the common assumption of ideal decision feedback that is essential for many existing works [5, 6, 7, 11].

Throughout this paper, we use the following nomenclature. Upper case boldface letters $\mathbf{A}$ are used to indicate matrices, lower case boldface letters $\mathbf{a}$ are used to for column vectors. The ith diagonal element of matrix $\mathbf{A}$ is denoted by $[\mathbf{A}]_i$. $E\{\cdot\}$ denotes mathematical expectation. $\mathcal{C}$ is the set of complex numbers and $\mathcal{C}^{m\times n}$ refers to complex-valued matrices with dimension m by n. In addition, a diagonal matrix with diagonal entries $a_1, \ldots, a_k$ is represented by $\mathrm{diag}(a_1, \cdots, a_k)$.

2 SYSTEM MODEL

Consider a MIMO communication system with N_t transmit antennas and N_r receive antennas. The i-th bit to be transmitted on the m-th antenna is $b_i^{(m)} \in \mathcal{B}$. The binary sequence on the m-th transmit antenna is encoded with a channel code, interleaved, and then mapped to modulation symbols. Let $\mathbf{c}_i^{(m)} = [c_{i1}^{(m)}, c_{i2}^{(m)}, \cdots, c_{ip}^{(m)}] \in \mathcal{B}^p$ be a block of p interleaved coded bits mapped to a modulation symbol $s_i^{(m)} \in \mathcal{S}$, where $\mathcal{S} = \{\chi_q\}_{q=1}^{Q}$ is the modulation constellation set with cardinality $Q = 2^p$.

The modulated symbols are transmitted over the time dispersive MIMO channels. The discrete-time channel impulse response between the m-th transmit antenna and the n-th receive antenna is represented by $\mathbf{h}^{(n,m)} = [h_0^{(n,m)}, \cdots, h_{L-1}^{(n,m)}]^T \in \mathcal{C}^L$, where L is the channel memory length.

Stacking the received samples from the N_r receive antennas at the time instant i as a column vector yields

$$\mathbf{r}_i = \sum_{l=0}^{L-1} \mathbf{H}_l \mathbf{s}_{i-l} + \mathbf{w}_i, \tag{1}$$

where $\mathbf{r}_i = [r_i^{(1)}, \cdots, r_i^{(N_r)}]^T$, $\mathbf{s}_i = [s_i^{(1)}, \cdots, s_i^{(N_t)}]^T$, and $\mathbf{w}_i = [w_i^{(1)}, \cdots, w_i^{(N_r)}]^T$ are the received sample vector, transmitted symbol vector, and additive white Gaussian noise (AWGN) vector at time instant i, respectively. The MIMO channel matrix $\mathbf{H}_l$ is

$$\mathbf{H}_l = \begin{bmatrix} h_l^{(1,1)} & \cdots & h_l^{(1,N_t)} \\ \vdots & \ddots & \vdots \\ h_l^{(N_r,1)} & \cdots & h_l^{(N_r,N_t)} \end{bmatrix} \in \mathcal{C}^{N_r \times N_t}, \tag{2}$$

The modulated symbols are grouped into blocks. During transmissions, a guard interval of length $L-1$ is inserted between consecutive blocks to avoid inter-block interferences.

A turbo equalizer performs detection of $\mathbf{s}_i$ by iteratively exchanging soft information between a SISO equalizer and a SISO decoder. For the MIMO system described in (2), the SISO equalizer needs to combat both ISI due to channel dispersion and MI due to spatial multiplexing.

3 SOFT INTERFERENCE CANCELATION EQUALIZER

A low complexity soft interference cancellation equalizer is proposed in this section to balance the tradeoff between equalization complexity and performance.

3.1 SICE STRUCTURE

The inputs to the SICE equalizer include the received data vectors, $\{\mathbf{r}_i\}$, and the *a priori* log-likelihood ratio (LLR),

$$\eta_{ij}^{(m)} = \log \frac{P(c_{ij}^{(m)} = 0)}{P(c_{ij}^{(m)} = 1)}. \tag{3}$$

During the first iteration, $\eta_{ij}^{(m)} = 0$, $\forall i$, j, and m. The soft output of the SICE is the extrinsic LLR $\lambda_{ij}^{(m)}$ for the coded bit $c_{ij}^{(m)}$, which is deinterleaved and then used as the input to the SISO channel decoder.

The SICE contains three linear filters. During the detection of $\mathbf{x}_i$, a feedforward filter, $\mathbb{F}$, is used to suppress both ISI and MI to the symbol vector $\mathbf{x}_i$; a causal feedback filter, $\mathbb{C}$, is designed to perform soft interference cancellation with respect to the residual interference from $\mathbf{x}_k$, for $k < i$; and an anti-causal feedback filter, $\mathbb{A}$, performs soft interference cancellation over residual interference caused by anti-causal symbols, $\mathbf{x}_k$, for $k > i$.

The feedforward filter can be modeled as a tapped-delay-line filter with N_1 anti-causal taps and N_2+1 causal taps, with the coefficient of the n-th tap, $\mathbf{F}_n$, being a $N_t \times N_r$ matrix, for $n = -N_1, \cdots, 0, \cdots, N_2$. The output of the feedforward filter, $\mathbf{v}_i \in \mathcal{C}^T$, can then be written as

$$\mathbf{v}_i = \sum_{n=-N_1}^{N_2} \mathbf{F}_n \mathbf{r}_{i-n} = \mathbb{F}\mathbf{y}_i, \tag{4}$$

where $\mathbb{F} = [\mathbf{F}_{N_2}, \mathbf{F}_{N_2-1} \cdots, \mathbf{F}_{-N_1}] \in \mathcal{C}^{N_t \times (N_1+N_2+1)N_r}$, and $\mathbf{y}_i = [\mathbf{r}_{i-N_2}^T, \mathbf{r}_{i-N_2+1}^T \cdots, \mathbf{r}_{i+N_1}^T]^T \in \mathcal{C}^{(N_1+N_2+1)N_r}$. From (2), the vector $\mathbf{y}_i$ can be expressed as

$$\mathbf{y}_i = \mathbb{H}\mathbf{x}_i + \mathbf{z}_i \tag{5}$$

where $\mathbf{x}_i = [\mathbf{s}_{i-N_3}^T, \cdots, \mathbf{s}_{i+N_1}^T]^T \in \mathcal{S}^{(N_1+N_3+1)N_t}$ with $N_3 = N_2 + L - 1$, and $\mathbf{z}_i = [\mathbf{w}_{i-N_2}^T, \mathbf{w}_{i-N_2+1}^T \cdots, \mathbf{w}_{i+N_1}^T]^T \in \mathcal{C}^{(N_1+N_2+1)N_r}$ are the symbol vector and noise vector, respectively. The extended channel matrix $\mathbb{H}$ is of size $(N_1+N_2+1)N_r \times (N_1+N_3+1)N_t$, and it can be represented as

$$\mathbb{H} = \begin{bmatrix} \mathbf{H}_{L-1} & \cdots & \mathbf{H}_0 & & \mathbf{0} \\ & \ddots & & \ddots & \\ \mathbf{0} & & \mathbf{H}_{L-1} & \cdots & \mathbf{H}_0 \end{bmatrix}. \tag{6}$$

Denote the causal and anti-causal soft decisions as $\hat{\mathbf{s}}_k \in \mathcal{C}^{N_t}$, for $k = i - N_3, \cdots, i-1$, and $\tilde{\mathbf{s}}_k \in \mathcal{C}^{N_t}$, for $k = i+1, \cdots, i+N_1$, respectively. The output of the causal and anti-causal feedback filters can be written as $\sum_{n=1}^{N_3} \mathbf{C}_n \hat{\mathbf{s}}_{i-n} = \mathbb{C}\hat{\mathbf{x}}_i$ and $\sum_{n=-N_1}^{-1} \mathbf{A}_n \tilde{\mathbf{s}}_{i-n} = \mathbb{A}\tilde{\mathbf{x}}_i$, respectively, where

$$\hat{\mathbf{x}}_i = [\hat{\mathbf{s}}_{i-N_3}^T, \cdots, \hat{\mathbf{s}}_{i-1}^T]^T \in \mathcal{C}^{N_3 N_t}, \tag{7}$$

$$\tilde{\mathbf{x}}_i = [\tilde{\mathbf{s}}_{i+1}^T, \cdots, \tilde{\mathbf{s}}_{i+N_1}^T]^T \in \mathcal{C}^{N_1 N_t}. \tag{8}$$

The soft decision vectors, $\hat{\mathbf{x}}_i$ and $\tilde{\mathbf{x}}_i$, can be calculated by combining soft information from the previous iteration and the current iteration, and details will be discussed in Section 4.1. Combining the feedforward and feedback filters yields

$$\boldsymbol{\xi}_i = \mathbb{F}\mathbf{y}_i - \mathbb{C}\hat{\mathbf{x}}_i - \mathbb{A}\tilde{\mathbf{x}}_i. \tag{9}$$

3.2 FILTER DESIGN

The calculation of the SICE filters is discussed in this subsection. During the derivation, with the interleaver inserted in the encoder and modulator and no space-time block code employed at the transmitter, it is assumed that the transmitted symbols are independent in both the space and time domains, *i.e.*, $E[s_i^{(m)}(s_j^{(n)})^*] = 0$, for $m \neq n$ or $i \neq j$. Also it is reasonable to extend the assumption to soft decisions, *i.e.*, $E[s_i^{(m)}(\hat{s}_j^{(n)})^*] = E[s_i^{(m)}(\tilde{s}_j^{(n)})^*] = E[\hat{s}_i^{(m)}(\tilde{s}_j^{(n)})^*] = 0$, for $m \neq n$ or $i \neq j$.

The coefficients of the feedforward and feedback filters are developed to minimize the mean square error (MSE)

$$\sigma_i^2 = E[\|\mathbb{F}\mathbf{y}_i - \mathbb{C}\hat{\mathbf{x}}_i - \mathbb{A}\tilde{\mathbf{x}}_i - \mathbf{s}_i\|^2]. \tag{10}$$

Since σ_i^2 is quadratic in $\mathbb{F}$, $\mathbb{C}$, and $\mathbb{A}$, the minimum MSE (MMSE) solutions of the three filters can be calculated by setting the gradient of σ_i^2 with respect to the filters to 0, and the results are

$$\mathbb{C} = \mathbb{F}\mathbb{H}\mathbf{R}_{x\hat{x}}\mathbf{R}_{\hat{x}\hat{x}}^{-1}, \tag{11}$$

$$\mathbb{A} = \mathbb{F}\mathbb{H}\mathbf{R}_{x\tilde{x}}\mathbf{R}_{\tilde{x}\tilde{x}}^{-1}, \tag{12}$$

$$\mathbb{F} = \mathbf{R}_{sx}\mathbb{H}^H\left[\sigma_w^2 + \mathbb{H}\left(\mathbf{R}_{xx} - \mathbf{\Phi}_{\hat{x}} - \mathbf{\Phi}_{\tilde{x}}\right)\mathbb{H}^H\right]^{-1}. \tag{13}$$

where $\mathbf{R}_{x\hat{x}} = E[\mathbf{x}_i\hat{\mathbf{x}}_i^H] \in \mathcal{C}^{NN_t \times N_3N_t}$ with $N = N_1 + N_3 + 1$, $\mathbf{R}_{x\tilde{x}} = E[\mathbf{x}_i\tilde{\mathbf{x}}_i^H] \in \mathcal{C}^{NN_t \times N_1N_t}$, $\mathbf{R}_{\hat{x}\hat{x}} = E[\hat{\mathbf{x}}_i\hat{\mathbf{x}}_i^H] \in \mathcal{C}^{N_3N_t \times N_3N_t}$, $\mathbf{R}_{\tilde{x}\tilde{x}} = E[\tilde{\mathbf{x}}_i\tilde{\mathbf{x}}_i^H] \in \mathcal{C}^{N_1N_t \times N_1N_t}$, $\mathbf{\Phi}_{\hat{x}} = \mathbf{R}_{x\hat{x}}\mathbf{R}_{\hat{x}\hat{x}}^{-1}\mathbf{R}_{x\hat{x}}^H$, and $\mathbf{\Phi}_{\tilde{x}} = \mathbf{R}_{x\tilde{x}}\mathbf{R}_{\tilde{x}\tilde{x}}^{-1}\mathbf{R}_{x\tilde{x}}^H$.

The evaluations of the filters in (13) - (18) require the knowledge of the correlation matrices between the transmitted symbol and the causal or anti-causal soft decisions, which in turn depend on their respective statistical properties. Details are given in the next section.

4 SOFT DECISIONS

4.1 CALCULATIONS OF THE SOFT DECISIONS

4.1.1 Anti-Causal Soft Decisions. The anti-causal soft decisions can be calculated by utilizing the *a priori* LLR, $\eta_{k,j}^{(m)}$, from the previous iterations. The anti-causal soft decision, $\tilde{s}_k^{(m)} = \sum_{q=1}^{Q} \chi_q P(s_k^{(m)}$
$= \chi_q)$, can be calculated as

$$\tilde{s}_k^{(m)} = \sum_{q=1}^{Q} \chi_q \prod_{j=1}^{p} \frac{1}{2} \left[1 + d_{q,j} \tanh \left(\eta_{k,j}^{(m)} / 2 \right) \right], \tag{14}$$

where $d_{q,j} = 1 - 2c_{q,j}$ is the bipolar representation of the coded bit $c_{q,j}$, and it is assumed that the binary sequence $[c_{q,1}, \cdots, c_{q,p}]$ is mappled to $\chi_q \in \mathcal{S}$.

4.1.2 Causal Soft Decisions. The causal soft decisions can be calculated by utilizing the output of the SICE, which can be modeled as a random vector. We have the following results regarding the mean and auto-correlation function of ξ_i at the output of the SICE.

Proposition 1. *Under the assumption that the symbols are independent in both the space and time domains, the output of the SICE given in* (10) *can be modeled as a zero-mean random vector with the auto-correlation function given by*

$$\mathbf{R}_{\xi\xi} = E(\boldsymbol{\xi}_i \boldsymbol{\xi}_i^H) = \sum_{l=0}^{L-1} \mathbf{F}_{-l} \mathbf{H}_l \tag{15}$$

Proof. The proof is in Appendix A. □

Since $\boldsymbol{\xi}_i$ is random, it is assumed that $\boldsymbol{\xi}_i$ can be modeled as the output of a Gaussian channel. The m-th element of $\boldsymbol{\xi}_i$ can be alternatively expressed as [8]

$$\xi_{i,m} = g_{i,m} s_{i,m} + u_{i,m}, \tag{16}$$

where $g_{i,m}$ is a constant and $u_{i,m}$ is zero-mean complex Gaussian distributed with variance σ_m^2.

Corollary 1. *With the equivalent Gaussian channel model given in* (23)*, we have* $g_{i,m} = \sum_{l=0}^{L-1} \mathbf{f}_{-l,m} \mathbf{h}_{l,m}$*, with* $\mathbf{f}_{l,m}$ *being the* m*-th row of* $\mathbf{F}_l$ *and* $\mathbf{h}_{l,m}$ *the* m*-th column of* $\mathbf{H}_l$*, and* $\sigma_m^2 = g_{i,m}(1 - g_{i,m})$*.*

Proof. The proof is in Appendix B. □

Following the model in (23), the extrinsic LLR, $\lambda_{i,j}^{(m)} = \log \frac{P(\xi_{i,m}|c_{i,j}^{(m)}=0)}{P(\xi_{i,m}|c_{i,j}^{(m)}=1)}$, can be calculated as

$$\lambda_{i,j}^{(m)} = \log \frac{\sum_{\chi_o \in \mathcal{S}_j^0} \exp\left[-\rho_{i,m}(\chi_o)\right]}{\sum_{\chi_o \in \mathcal{S}_j^1} \exp\left[-\rho_{i,m}(\chi_o)\right]}, \tag{17}$$

where $\mathcal{S}_j^b \subset \mathcal{S}$ contains the symbol χ with the j-th mapped bit being $b \in \{0, 1\}$, and $\rho_{i,m}(\chi_o) = \frac{|\xi_{i,m} - g_{i,m}\chi_o|^2}{g_{i,m}(1-g_{i,m})}$.

The causal soft decisions are calculated by utilizing the full LLR $L_{k,j}^{(m)} = \lambda_{k,j}^{(m)} + \eta_{k,j}^{(m)}$. Similar to (20), the causal soft decisions can then be calculated by using the full LLR as

$$\hat{s}_k^{(m)} = \sum_{q=1}^{Q} \chi_q \prod_{j=1}^{p} \frac{1}{2} \left[1 + d_{q,j} \tanh\left(L_{k,j}^{(m)}/2\right)\right]. \tag{18}$$

4.2 STATISTICAL PROPERTIES OF THE SOFT DECISIONS

As shown in (13), (14), and (18), the formulation of the filters requires the cross-correlation matrices, $\mathbf{R}_{x\hat{x}}$ and $\mathbf{R}_{x\tilde{x}}$, and the auto-correlation matrices, $\mathbf{R}_{\hat{x}\hat{x}}$ and $\mathbf{R}_{\tilde{x}\tilde{x}}$.

With the space-time independence assumption, we can express the cross-correlation matrices, $\mathbf{R}_{x\hat{x}}$ and $\mathbf{R}_{x\tilde{x}}$, as

$$\mathbf{R}_{x\hat{x}} = \begin{bmatrix} \mathbf{R}_{s\hat{s}}^T & \mathbf{0}_{(N_1+1)N_t \times N_3 N_t}^T \end{bmatrix}^T \tag{19a}$$

$$\mathbf{R}_{x\tilde{x}} = \begin{bmatrix} \mathbf{0}_{(N_3+1)N_t \times N_1 N_t}^T & \mathbf{R}_{s\tilde{s}}^T \end{bmatrix}^T \tag{19b}$$

where $\mathbf{R}_{s\hat{s}} \in \mathcal{C}^{N_3 N_t \times N_3 N_t}$ and $\mathbf{R}_{s\tilde{s}} \in \mathcal{C}^{N_1 N_t \times N_1 N_t}$ are diagonal matrices defined as

$$\mathbf{R}_{s\hat{s}} = \text{diag}\left[\alpha_{s\hat{s}}^{(1)}, \cdots, \alpha_{s\hat{s}}^{(N_t)} | \cdots | \alpha_{s\hat{s}}^{(1)}, \cdots, \alpha_{s\hat{s}}^{(N_t)}\right] \tag{20a}$$

$$\mathbf{R}_{s\tilde{s}} = \text{diag}\left[\alpha_{s\tilde{s}}^{(1)}, \cdots, \alpha_{s\tilde{s}}^{(N_t)} | \cdots | \alpha_{s\tilde{s}}^{(1)}, \cdots, \alpha_{s\tilde{s}}^{(N_t)}\right] \tag{20b}$$

with

$$\alpha_{s\hat{s}}^{(m)} = E[s_i^{(m)} \hat{s}_i^{(m)*}] = \frac{1}{Q} \sum_{q=1}^{Q} \chi_q E[\hat{s}_i^{(m)*} | s_i^{(m)} = \chi_q] \tag{21a}$$

$$\alpha_{s\tilde{s}}^{(m)} = E[s_i^{(m)} \tilde{s}_i^{(m)*}] = \frac{1}{Q} \sum_{q=1}^{Q} \chi_q E[\tilde{s}_i^{(m)*} | s_i^{(m)} = \chi_q], \tag{21b}$$

where $P(s_i^{(m)}) = \frac{1}{Q}$ is used in the above equations.

The auto-correlation matrices, $\mathbf{R}_{\hat{x}\hat{x}} \in \mathcal{C}^{N_3 N_t \times N_3 N_t}$ and $\mathbf{R}_{\tilde{x}\tilde{x}} \in \mathcal{C}^{N_1 N_t \times N_1 N_t}$, are diagonal matrices expressed as

$$\mathbf{R}_{\hat{x}\hat{x}} = \text{diag}\left[\alpha_{\hat{s}\hat{s}}^{(1)}, \cdots, \alpha_{\hat{s}\hat{s}}^{(N_t)} | \cdots | \alpha_{\hat{s}\hat{s}}^{(1)}, \cdots, \alpha_{\hat{s}\hat{s}}^{(N_t)}\right], \tag{22a}$$

$$\mathbf{R}_{\tilde{x}\tilde{x}} = \text{diag}\left[\alpha_{\tilde{s}\tilde{s}}^{(1)}, \cdots, \alpha_{\tilde{s}\tilde{s}}^{(N_t)} | \cdots | \alpha_{\tilde{s}\tilde{s}}^{(1)}, \cdots, \alpha_{\tilde{s}\tilde{s}}^{(N_t)}\right], \tag{22b}$$

where

$$\alpha_{\hat{s}\hat{s}}^{(m)} = E\left[|\hat{s}_i^{(m)}|^2\right] = E\left[|\hat{s}_i^{(m)}|^2 \middle| s_i^{(m)} = \chi_q\right] \tag{23a}$$

$$\alpha_{\tilde{s}\tilde{s}}^{(m)} = E\left[|\tilde{s}_i^{(m)}|^2\right] = E\left[|\tilde{s}_i^{(m)}|^2 \middle| s_i^{(m)} = \chi_q\right] \tag{23b}$$

From (31) and (33), the correlation coefficients, $\alpha_{s\hat{s}}^{(m)}$, $\alpha_{s\tilde{s}}^{(m)}$, $\alpha_{\hat{s}\hat{s}}^{(m)}$, and $\alpha_{\tilde{s}\tilde{s}}^{(m)}$, depend on the first and second conditional moments of $\hat{s}_i^{(m)}$ and $\tilde{s}_i^{(m)}$.

4.2.1 Conditional Moments of the Anti-Causal Soft Decisions $\tilde{s}_i^{(m)}$. To facilitate the calculation of the conditional moments, we adopt the assumption that the *a priori* LLR, $\eta_{i,j}^{(m)}$, can be modeled as coming from an equivalent AWGN channel with signal-to-noise ratio (SNR) $\gamma_m/2$ [20]

$$\eta_{i,j}^{(m)} = d_{i,j}^{(m)}\gamma_m + v_{i,j}^{(m)}, \tag{24}$$

where $v_{i,j}^{(m)} \sim \mathcal{N}(0, 2\gamma_m)$. The value of γ_m can be estimated from the *a priori* LLR with the maximum-likelihood estimation [8].

From (20) and (34), we have

$$E\left[\tilde{s}_i^{(m)} | s_i^{(m)} \in \chi_o\right] = \sum_{q=1}^{Q} \chi_q \prod_{j=1}^{p} \frac{1}{2} \times \left\{1 + d_{q,j} E\left[\tanh\left(\eta_{i,j}^{(m)}/2\right) \middle| \chi_o\right]\right\}, \tag{25}$$

where the expectation is performed with respect to $\eta_{i,j}^{(m)}$, and $\eta_{i,j}^{(m)} \sim \mathcal{N}(d_{o,j}^{(m)}\gamma_m, 2\gamma_m)$, with $d_{o,j}^{(m)}$ being the bipolar representation of the j-th bit of the vector mapped to $\chi_o \in \mathcal{S}$.

Similarly, the conditional second moment of $\tilde{s}_i^{(m)}$ is

$$\begin{aligned} E\left[|\tilde{s}_i^{(m)}|^2 | s_i^{(m)} = \chi_o\right] = \sum_{q_1=1}^{Q}\sum_{q_2=1}^{Q} \chi_{q_1}\chi_{q_2}^* \prod_{j=1}^{p} \frac{1}{4} \times \\ \left\{1 + \tilde{c}_{q_1,j}\tilde{c}_{q_2,j} E\left[\tanh^2\left(\eta_{i,j}^{(m)}/2\right)|\chi_o\right] + \right. \\ \left. (\tilde{c}_{q_1,j} + \tilde{c}_{q_2,j}) E\left[\tanh\left(\eta_{i,j}^{(m)}/2\right)|\chi_o\right]\right\} \end{aligned} \tag{26}$$

The expectations, $E\left[\tanh\left(\eta_{i,j}^{(m)}/2\right)\middle|\chi_o\right]$ and $E\left[\tanh^2\left(\eta_{i,j}^{(m)}/2\right)\middle|\chi_o\right]$, can be evaluated numerically offline and tabulated as functions of γ_m.

4.2.2 Conditional Moments of the Causal Soft Decisions $\hat{s}_i^{(m)}$. The causal soft decision $\hat{s}_i^{(m)}$ is a function of $L_{i,j}^{(m)} = \lambda_{i,j}^{(m)} + \eta_{i,j}^{(m)}$. Therefore, the conditional moments, $E\left[\hat{s}_i^{(m)} | s_i^{(m)} = \chi_o\right]$ and $E\left[|\hat{s}_i^{(m)}|^2 | s_i^{(m)} = \chi_o\right]$ can be calculated by replacing $\eta_{i,j}^{(m)}$ with $\eta_{i,j}^{(m)} + \lambda_{i,j}^{(m)}$ in (36) and (37), respectively. The evaluations of the second order statistics require the knowledge of the following two quantities

$$E\left[\tanh\left(\eta_{i,j}^{(m)}/2 + \lambda_{i,j}^{(m)}/2\right)|\chi_o\right], \tag{27a}$$

$$E\left[\tanh^2\left(\eta_{i,j}^{(m)}/2 + \lambda_{i,j}^{(m)}/2\right)|\chi_o\right], \tag{27b}$$

The conditional pdf of $p(\lambda_{i,j}^{(m)}|\chi_o)$ can be evaluated numerically by using (27). The first and second order moments of $\tanh\left(\eta_{i,j}^{(m)}/2 + \lambda_{i,j}^{(m)}/2\right)$ can then be numerically caulated by using (38), the Gaussian pdf of $\eta_{i,j}^{(m)}$, and the pdf of $\lambda_{i,j}^{(m)}$.

Once the results in (38) are obtained, then the conditional moments of $\hat{s}_i^{(m)}$ can be obtained by replacing $\eta_{i,j}^{(m)}$ with $\eta_{i,j}^{(m)} + \lambda_{i,j}^{(m)}$ in (36) and (37).

The evaluations of the conditional moments, $\alpha_{\hat{s}\hat{s}}^{(m)}$ and $\alpha_{\tilde{s}\tilde{s}}^{(m)}$, require the pdf of the filter output $\xi_{i,m}$, which in turn depends on $g_{i,m}$ and the feedforward filter $\mathbb{F}$. On the other hand, the calculation of $\mathbb{F}$ requires the knowledge of $\alpha_{\hat{s}\hat{s}}^{(m)}$ and $\alpha_{\tilde{s}\tilde{s}}^{(m)}$. We address this problem by using a linear MMSE at the first iteration to initialize the values of $\alpha_{\hat{s}\hat{s}}^{(m)}$ and $\alpha_{\tilde{s}\tilde{s}}^{(m)}$, and the proposed SICE is employed starting from the second iterations.

5 SIMULATION RESULTS

The EXIT chart and bit error rate (BER) of the proposed turbo SICE receiver are evaluated in this section with simulations. Simulations are performed for a 2×2 MIMO system with 5 channel taps as

$$\begin{aligned} \mathbf{h}^{(1,1)} &= [-0.21, -0.5, 0.72, 0.36, 0.21] \\ \mathbf{h}^{(1,2)} &= [0.407, 0.815, 0.407, 0, 0] \\ \mathbf{h}^{(2,1)} &= [0.227, 0.460, 0.688, 0.460, 0.227] \\ \mathbf{h}^{(2,2)} &= [0.5, 0.5, 0.5, 0.5, 0.5]. \end{aligned} \tag{28}$$

It should be noted that the channels are normalized to unit energy during the simulations. The transmitted binary bits are encoded by a rate $R = 1/2$ convolutional code with generator polynomial $G = [7, 5]_8$ followed by a size 10560 random interleaver. The BER performance of systems with the proposed SICE receiver will be compared to those with the approximate-MMSE-LE receivers [2] and SDFE receivers [9]. For all the equalizers, we have $N_1 = 9$ and $N_2 = 5$.

Fig. 5.3 shows the EXIT chart for systems with the same maximum *a posteriori* (MAP) decoder but different SISO equalizers. The horizontal (vertical) axis is the mutual information at the input (output) of the equalizer. The mutual information transfer curves for the equalizers are obtained by measuring the mutual information input at the second transmit antenna, and the mutual information output at the second receive antenna. Since the output of the second receive antenna depends on the input at both transmit antennas, the curve is obtained by averaging over all possible inputs at the first transmit antenna. The SICE and the MAP decoder curves form a wider tunnel than those formed with the SDFE or the approximate-MMSE-LE. This verifies the faster convergence of the SICE-based receiver. More importantly, as

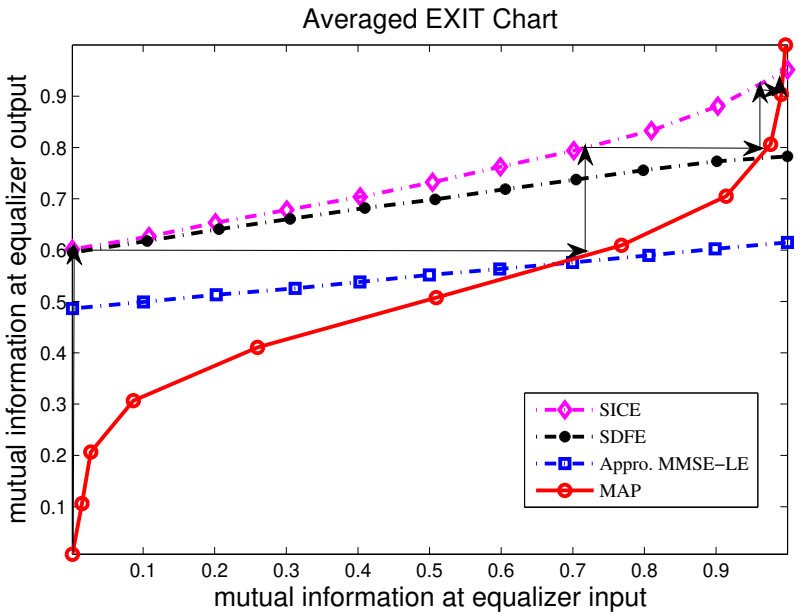

Figure 5.1. Average Projected EXIT chart for Tx2 with 8PSK Constellation and convolution coding (SNR=18db)

the iteration progresses, the SICE can almost reach the ideal output with the output mutual information being 0.95 when the input mutual information is 1. On the other hand, the highest output mutual information that can be achieved by the SDFE and the MMSE-LE is only 0.79 and 0.60, respectively. This means that, even with ideal soft information at the input, the SDFE or MMSE-LE can never produce ideal soft information at their respective outputs. The performance loss of SDFE is mainly due to the overlook of the anti-casual interference, which limits the quality of the soft information at the output of the SDFE. On the other hand, the proposed SICE can almost achieve the ideal matched filter bound as long as the quality of the soft information at the input is good enough, which can be obtained with more iterations.

Figs. 6.1, 6.2 and 6.3 show the BER performance of the three different equalizers with QPSK, 8PSK, and 16QAM modulations, respectively. The block length

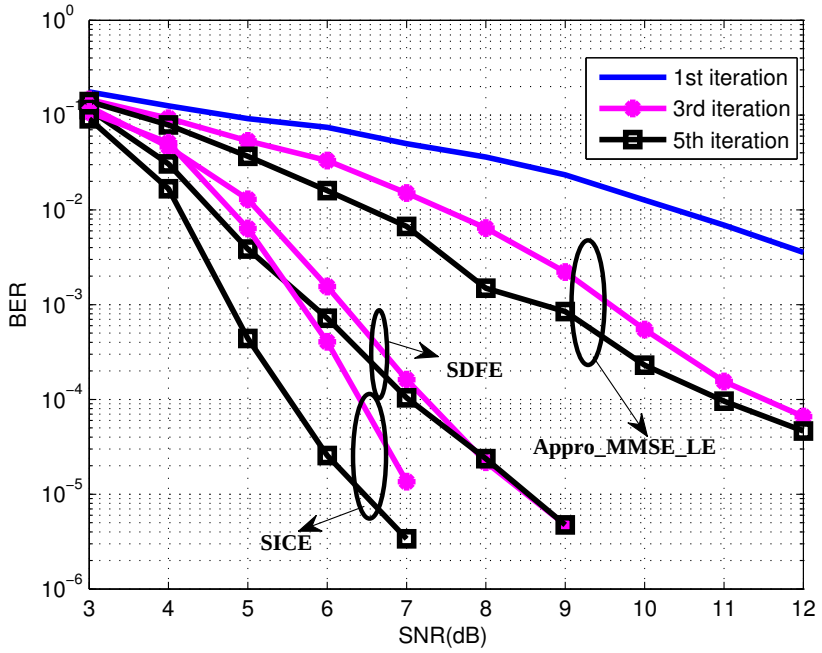

Figure 5.2. QPSK BER performance with convolutional coding.

is 1024 symbols for all modulation schemes. In the first iteration, all three equalizers have the same performance due to the lack of *a priori* information. After the first iteration, the SICE achieves significant performance gains over the other two equalizers for all system configurations, and the performance improvement increases for higher constellation sizes. At the BER $= 3 \times 10^{-5}$ and after the fifth iteration, the SICE outperforms the SDFE by 1.8 dB, 2.5 dB, and 3.0 dB, for systems with QPSK, 8PSK, and 16QAM modulations, respectively. The performance improvement over the approximate-MMSE-LE is much bigger. For example, at BER $= 10^{-2}$, the SICE outperforms the approximate-MMSE-LE by 4.8 dB after the fifth iteration with 16QAM modulation.

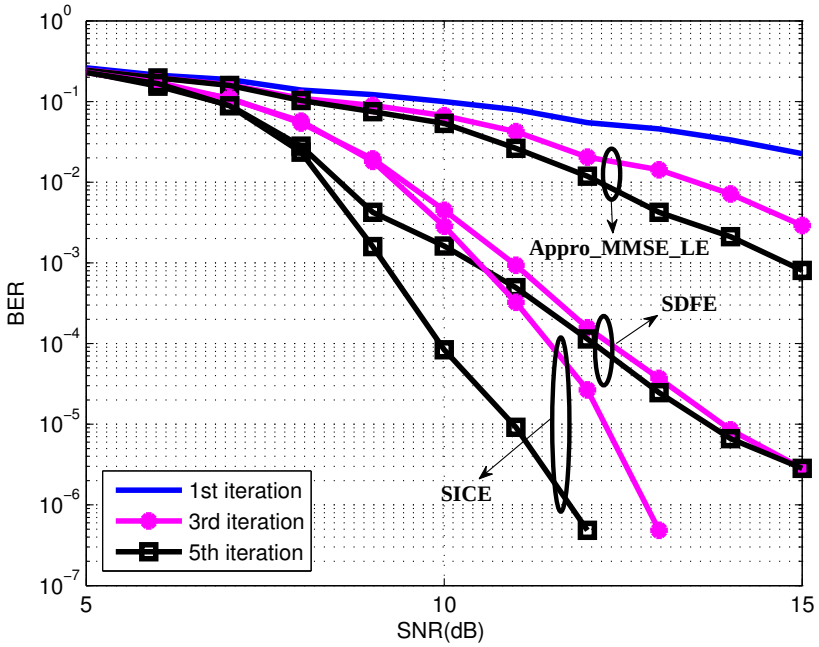

Figure 5.3. 8PSK BER performance with convolutional coding.

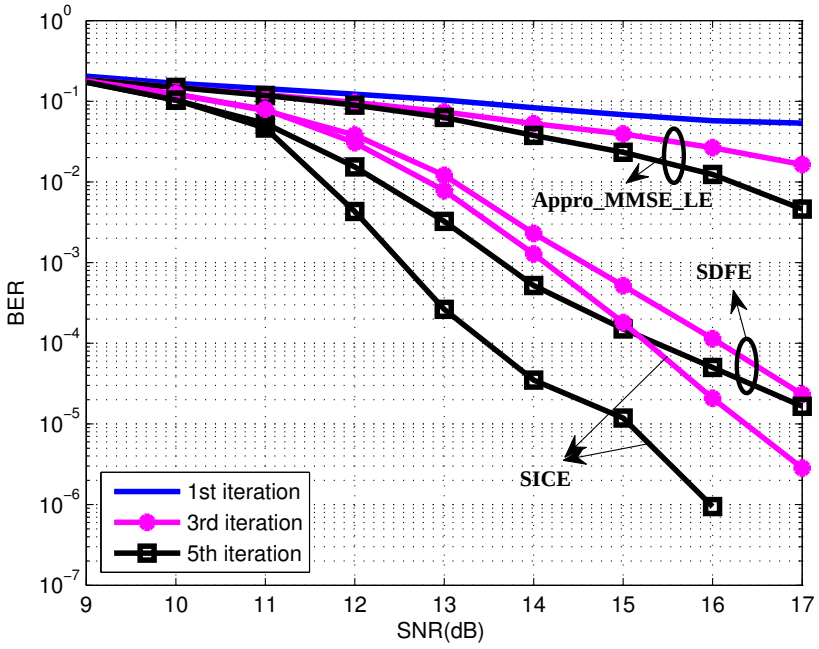

Figure 5.4. 16QAM BER performance with convolutional coding.

6 CONCLUSION

A soft interference cancellation equalizer has been proposed for turbo equalization of MIMO systems operating in time dispersive channels. The soft interference cancellation was achieved by subtracting soft decisions of both causal and anti-causal interfering symbols. It has been demonstrated through both EXIT chart analysis and computer simulations that the anti-causal soft decisions are critical to the equalizer performance. Due to the inclusion of anti-causal soft decisions, the proposed SICE achieved considerable performance gains over the approximate-MMSE-LE and SDFE, in terms of both convergence speed and BER. The EXIT chart analysis demonstrated that the SICE performance could approach the matched filter bound with ideal *a priori* input, yet the performance of SDFE is severely limited by the interference from the anti-causal symbols regardless of the quality of the soft input or the number of iterations.

7 PROOF OF PROPOSITION 1

From (10), it is straightforward that $E[\xi_i] = \mathbf{0}_{N_t}$. The auto-correlation function can be alternatively represented as

$$\mathbf{R}_{\xi\xi} = E[\boldsymbol{\xi}_i \mathbf{y}_i^H]\mathbb{F}^H - E[\boldsymbol{\xi}_i \hat{\mathbf{x}}_i^H]\mathbb{C}^H - E[\xi_i \tilde{\mathbf{x}}_i^H]\mathbb{A}^H \tag{29}$$

From (13), it can be easily shown that $E[\xi_i \hat{\mathbf{x}}_i^H] = \mathbf{0}_{N_t \times N_3 N_t}$ and $E[\boldsymbol{\xi}_i \tilde{\mathbf{x}}_i^H] = \mathbf{0}_{N_t \times N_1 N_t}$.

The feedforward filter $\mathbb{F}$ is obtained by setting $\frac{\partial \sigma_e^2}{\partial \mathbb{F}_i^H} = 2E\left[(\boldsymbol{\xi}_i - \mathbf{s_i})\mathbf{y}_i^H\right] = 0$, which results in $E[\boldsymbol{\xi}_i \mathbf{y}_i^H] = E[\mathbf{s}_i \mathbf{y}_i^H] = \mathbf{R}_{sx}\mathbb{H}^H$. It can be easily shown that

$$\mathbf{R}_{sx} = E[\mathbf{s}_i \mathbf{x}_i^H] = [\mathbf{0}_{N_t \times N_3 N_t}, \mathbf{I}_{N_t}, \mathbf{0}_{N_t \times N_1 N_t}] \in \mathcal{C}^{N_t \times N N_t},$$

where $\mathbf{0}_{M \times N}$ is a size $M \times N$ all-zero matrix. Combining the above results with (22) yields (21).

8 PROOF OF COROLLARY 1

From (23), $E(\xi_{i,m}s^*_{i,m}) = g_{i,m}$. From (10), we have

$$E(\xi_{i,m}s^*_{i,m}) = \mathbb{F}_m \mathbb{H} E(\mathbf{x}_i s^*_{i,m}) = \sum_{l=0}^{L-1} \mathbf{f}_{-l,m}\mathbf{h}_{l,m}, \tag{30}$$

where $\mathbb{F}_m$ is the m-th row of $\mathbb{F}$.

From Proposition 1, $E(|\xi_{i,m}|^2) = g_{i,m}$. Therefore $g_{i,m}$ is a real number. From (23), we have

$$E(|\xi_{i,m}|^2) = g^2_{i,m} + \sigma^2_m. \tag{31}$$

Combining the above results yields $\sigma^2_m = g_{i,m}(1 - g_{i,m})$.

9 REFERENCES

[1] M. T*ü*chler, A. C. Singer, and R. Koetter, "Minimum mean square error equalization using a priori information," in *IEEE Trans. Signal Processing*, vol.50, pp.673-683, Mar. 2002.

[2] M. T*ü*chler, R. Koetter, and A. C. Singer, "Turbo equalization: Principles and new results," *IEEE Trans. Commun*, vol. 50, pp.754-767, May. 2002.

[3] A. Dejonghe and L. Vanderdorpe, "Turob equalization for multilevel modulation: An efficient low-complexity scheme," in *Proc. IEEE Int. Conf. Commun.*, vol.3, pp.1863-1867, 2002.

[4] D. Williamson, R. A. Kennedy, and G. W. Pulford, "Block decision feedback equalization," IEEE Trans. Commun., vol. 40, pp. 255-264, Feb., 1992.

[5] Z. Wu and J. Cioffi, "Low complexity iterative decoding with Decision-Aided Equalization for magnetic recording channels," *IEEE J. Select. Areas Commun.*, vol.19, pp.699-708, Apr. 2001.

[6] J. Wu and Y. R. Zheng, "Low complexity soft-input soft-output block decision feedback equalization," *IEEE J. Select. Areas Commun.*, vol. 26, pp.281-289, Feb. 2008.

[7] R. R. Lopes and J. R. Barry, "The soft-feedback equalizer for turbo equalization of highly dispersive channels," *IEEE Trans. Commun*, vol.54, pp. 783-788, Jan. 2006.

[8] H. Lou and C. Xiao, "Soft-decision feedback trubo equalization for multilevel modulations," *IEEE Trans. Signal Processing*, vol.59, pp. 186-195, Jan. 2011.

[9] A. Rafati, H. Lou, and C. Xiao, "Low-complexity soft-decision feedback turbo equalization for MIMO systems with multilevel modulations," *IEEE Trans. Veh. Technol.*, vol. 60, pp. 3218-3227, Sept. 2011.

[10] J. Tao, J. Wu, and Y. R. Zheng, "Reliability-based turbo detection," *IEEE Trans. Wireless Commun.*, vol. 10, pp. 2352-2361, July 2011.

[11] S ten Brink "Convergence behavior of iteratively decoded parallel concatenated codes", *IEEE Trans. Commun.,* vol.49, pp. 1727-1737, Oct. 2001.

V. Low Complexity Soft-Interference Cancelation Turbo Equalization for MIMO Systems with Multilevel Modulations

Jingxian Wu, Longbao Wang, and Chengshan Xiao

ABSTRACT—This paper presents a low complexity soft-interference cancelation equalizer (SICE) for the turbo detection of multi-input multi-output (MIMO) systems operating in time dispersive channels. The SICE contains three time-invariant linear filters: a feedforward filter, a causal feedback filter, and an anti-causal feedback filter. The feedforward filter is designed to suppress the intersymbol interference (ISI) due to channel time dispersion and the multiplexing interference (MI) from multiple transmit antennas. The causal (or anti-causal) feedback filter is developed to remove the residual interference caused by the symbols transmitted before (or after) the symbol under detection. The anti-causal soft decision is the *a priori* mean calculated by using the *a priori* information from the previous iteration, and the causal soft decision is in the form of the *a posteriori* mean calculated by combining both the extrinsic SICE output of the current iteration and the *a priori* information from the previous iteration. The statistical properties of the soft decisions are analyzed, and results are used to design the filter coefficients. The performance of the proposed SICE is verified through both extrinsic information transfer chart (EXIT) analysis and computer simulations. The EXIT chart analysis shows that, due to the inclusion of the anti-causal soft decision, the SICE performance approaches the ideal matched filter bound as the iteration progresses. On the other hand, for conventional equalizers without anti-causal interference cancelation, there is always a non-diminishing gap between their performance and the matched filter bound, even with ideal *a priori* information at the equalizer inputs. Consequently, the proposed SICE achieves significant performance gains over conventional equalizers, in terms of both convergence speed and bit error rate.

1 INTRODUCTION

The constantly increasing demands for broadband high data rate communications necessitate the development of advanced communication transceivers that can aggressively reuse the space, time, and/or frequency resources. This usually results in severe interferences among the transmitted signals. For example, spatial multiplexing employed by multiple-input multiple-output (MIMO) systems leads to multiplexing interference (MI) among the data streams transmitted over different antennas in the space domain. Transmitting broadband data over a channel with coherence bandwidth less than the signal bandwidth leads to a time dispersive channel, which causes intersymbol interference (ISI) in the time domain. There are a wealth of works in the literature devoted to the development of detection techniques that can combat the negative impacts of MI and/or ISI through equalization and interference cancelation [1]- [15].

Many of the detection techniques follow the structure of a turbo equalizer [16]- [18], where a soft-input soft-output (SISO) equalizer iteratively exchanges soft information with a SISO channel decoder, separated by an interleaver. The turbo equalization has attracted considerable attentions due to its superior performance over non-iterative receivers. In addition, the rapid advancement of high speed digital circuits has made it possible for the low cost and efficient implementations of real time turbo equalizers. The optimum performance of turbo equalization can be achieved by employing the maximum *a posteriori* (MAP) algorithm [19] for both the SISO equalizer and SISO channel decoder. However, the complexity of the MAP equalizer grows exponentially with the channel length, modulation level, and the number of transmit antennas. The complexity is prohibitive for systems employing high level modulations.

A large number of low complexity SISO equalizers have been proposed to tradeoff the complexity with performance. A linear minimum mean squared error (MMSE) equalizer was proposed in [2]- [4] for turbo equalization, where the linear filter coefficients are calculated by using the *a priori* information at the equalizer input and are updated for each symbol. The complexity of the MMSE with time-varying coefficients can be reduced by using time-invariant coefficients for an entire block, at the cost of performance loss. One of the main performance limiting factors of MMSE is the residual interference at the output of the linear filter, especially for high level modulations. The residual interference of MMSE can be partly removed by means of decision feedback equalization (DFE) with either hard decisions [5] or soft decisions [6, 7]. Many of the DFE filter coefficients are derived by using the assumption of perfect interference cancelation, which is usually not the case in practical systems. In [8], a soft feedback equalizer (SFE) is developed without the assumption of perfect interference cancelation. Instead, the filter coefficients are developed by analyzing the statistical properties of the soft decisions and residual interference. The equalizer developed in [8] can only work for systems with binary modulations. It was later extended to system with high level modulations [9]. All the above works are developed for single-input single-output systems. Low complexity soft decision feedback equalizer (SDFE) [10] or reliability-based turbo detection [11] are proposed for MIMO systems, where the equalization needs to deal with both ISI and MI due to spatial multiplexing. All above works use time domain equalization. The complexity can be further reduced by employing single-carrier frequency domain equalization (SC-FDE) [12] and [13]. The low complexity of SC-FDE is usually achieved at the cost of performance loss due to the effects of noise enhancement [14] caused by fading compensation in the frequency domain during the FDE process.

Most DFE algorithms perform interference cancelation only over the causal symbols, which are the symbols transmitted before the current symbol under detection

[9]- [13]. However, the linear filtering will introduce residual interference from anti-casual symbols, or the symbols transmitted after the current symbol. For systems with high level modulations, the interference from anti-causal symbols becomes a serious performance limiting factor. It will be shown in this paper that ignoring the anti-causal interference results in a non-diminishing performance gap between the SDFE and the systems with ideal interference cancelations, even if the SDFE has ideal *a priori* input and operates at very high signal-to-noise ratio (SNR).

In this paper, we propose a new low complexity soft interference cancelation equalizer (SICE) for MIMO systems with high level modulations. In a MIMO system with time dispersive channels, the equalizer needs to deal with both ISI due to channel time dispersion and MI from data streams transmitted at different antennas. The proposed SICE performs soft interference cancelation over both causal symbols and anti-causal symbols to close the performance gap with ideal interference cancelations. The soft interference cancelation (SIC) over the causal symbols is performed through decision feedback of symbols detected in the current iteration. The SIC of the anti-causal symbols is enabled by the iterative structure, with which the soft decisions of the anti-causal soft decisions are calculated by utilizing the *a priori* soft input from the previous iteration. The inclusion of the anti-causal SIC is critical to the system performance. With the assistance of extrinsic information transfer (EXIT) chart [20], it is shown that the performance of SICE after sufficient number of iterations can converge to the ideal matched filter bound, which is obtained from ideal interference cancelation.

In addition, the coefficients of the SICE filters are calculated by analyzing the statistical properties of the causal and anti-causal soft decisions, such as their auto-correlations and cross-correlations with the ideal symbols. Consequently, the filter development does not require the common assumption of ideal decision feedback that

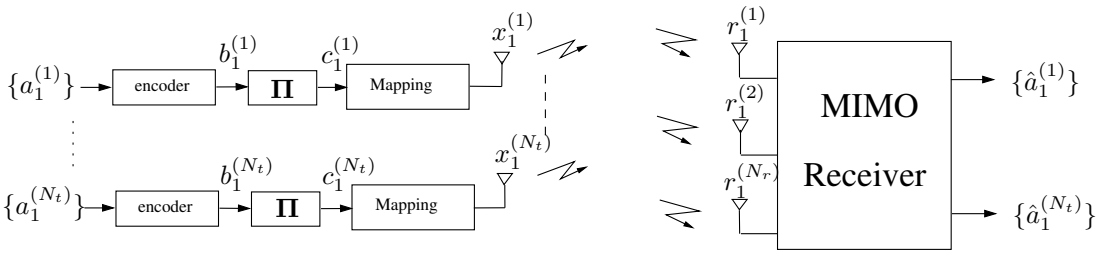

Figure 1.1. Block diagram of the Transmitter and Receiver in MIMO channel model.

is essential for many existing works [5,6,7,11]. Both EXIT chart analysis and simulation results demonstrate that the proposed SICE can achieve significant performance gains and faster convergence over existing turbo equalization schemes.

Throughout this paper, we use the following nomenclatures. Upper case boldface letters are used to indicate matrices, lower case boldface letters are used for column vectors. The ith diagonal element of matrix $\mathbf{A}$ is denoted by $[\mathbf{A}]_i$. $E\{\cdot\}$ denotes mathematical expectation. $\mathcal{C}$ is the set of complex numbers, and $\mathcal{B} = \{0, 1\}$. $\mathcal{C}^{m\times n}$ refers to complex-valued matrices with dimension m by n. In addition, a diagonal matrix with diagonal entries $a_1, \ldots, a_k$ is represented by $\text{diag}(a_1, \cdots, a_k)$.

2 SYSTEM MODEL

The block diagram of a MIMO communication system with N_t transmit antennas and N_r receive antennas is shown in Fig. 1.1. The j-th bit to be transmitted on the m-th antenna is $b_j^{(m)} \in \mathcal{B}$. The binary sequence on the m-th transmit antenna is encoded with a channel code, interleaved, and then mapped to modulation symbols. Let $\mathbf{c}_i^{(m)} = [c_{i1}^{(m)}, c_{i2}^{(m)}, \cdots, c_{ip}^{(m)}] \in \mathcal{B}^p$ be a block of p interleaved coded bits mapped to a modulation symbol $s_i^{(m)} \in \mathcal{S}$, where $\mathcal{S} = \{\chi_q\}_{q=1}^{Q}$ is the modulation constellation set with cardinality $Q = 2^p$.

The modulated symbols are transmitted over the time dispersive MIMO channels. The discrete-time channel impulse response between the m-th transmit antenna and n-th receive antenna is represented by $\mathbf{h}^{(n,m)} = [h_0^{(n,m)}, \cdots, h_{L-1}^{(n,m)}]^T \in \mathcal{C}^L$, where L is the channel memory length. The discrete-time baseband signal corresponding to the i-th symbol observed by the n-th receive antenna can then be written as

$$r_i^{(n)} = \sum_{m=1}^{N_t} \sum_{l=0}^{L-1} h_l^{(n,m)} s_{i-l}^{(m)} + w_i^{(n)}, \tag{1}$$

where $w_i^{(n)}$ is the additive white Gaussian noise (AWGN) with variance σ_w^2. The modulated symbols are grouped into blocks. During transmissions, a guard interval of length $L-1$ is inserted between consecutive blocks to avoid interference between consecutive blocks. It should be noted that there is still ISI among symbols in the same block.

Stacking the received samples from the N_r receive antennas as a column vector yields

$$\mathbf{r}_i = \sum_{l=0}^{L-1} \mathbf{H}_l \mathbf{s}_{i-l} + \mathbf{w}_i, \tag{2}$$

where $\mathbf{r}_i = [r_i^{(1)}, \cdots, r_i^{(N_r)}]^T \in \mathcal{C}^{N_r}$, $\mathbf{s}_i = [s_i^{(1)}, \cdots, s_i^{(N_t)}]^T \in \mathcal{S}^{N_t}$, and $\mathbf{w}_i = [w_i^{(1)}, \cdots, w_i^{(N_r)}]^T \in \mathcal{C}^{N_r}$ are the received sample vector, transmitted symbol vector, and AWGN vector, respectively. The MIMO channel matrix $\mathbf{H}_l$, for $l = 0, \cdots, L-1$, can be written as

$$\mathbf{H}_l = \begin{bmatrix} h_l^{(1,1)} & \cdots & h_l^{(1,N_t)} \\ \vdots & \ddots & \vdots \\ h_l^{(N_r,1)} & \cdots & h_l^{(N_r,N_t)} \end{bmatrix} \in \mathcal{C}^{N_r \times N_t}. \tag{3}$$

A turbo detector includes a SISO equalizer and a SISO channel decoder, which iteratively exchange soft information. For the MIMO system described in (2), the SISO equalizer needs to combat both ISI and MI. The soft output of the SISO equalizer is interleaved, and used as the soft input to the SISO channel decoder. Similarly, the output of the channel decoder is deinterleaved, and used as the soft input to the SISO equalizer.

The optimum equalization can be achieved by employing the MAP equalizer, which has a complexity that is on the order of $\mathcal{O}(Q^{N_t+L})$. The complexity is prohibitive for practical systems with highly dispersive channels, large number of transmit antennas, and/or high modulation level.

3 SOFT INTERFERENCE CANCELATION EQUALIZER

A low complexity soft interference cancelation equalizer is proposed in this section.

3.1 SICE STRUCTURE

The block diagram of the proposed SICE for MIMO systems is shown in Figure 3.1. The inputs to the SICE equalizer include the sequence of the received data vectors, $\{\mathbf{r}_i\}$, and the *a priori* log-likelihood ratio (LLR),

$$\eta_{ij}^{(m)} = \log \frac{P(c_{ij}^{(m)} = 0)}{P(c_{ij}^{(m)} = 1)}. \tag{4}$$

During the first iteration, $\eta_{ij}^{(m)} = 0$, $\forall i$, j, and m. The soft output of the SICE is the extrinsic LLR, $\lambda_{ij}^{(m)}$ for the coded bit $c_{ij}^{(m)}$, which is interleaved and then used as the input to the SISO channel decoder.

The SICE contains three linear filters. During the detection of $\mathbf{s}_i$, a feedforward filter, $\mathbb{F}$, is used to suppress both ISI and MI to the symbol vector $\mathbf{s}_i$; a causal feedback filter, $\mathbb{C}$, is designed to perform SIC with respect to the residual interference from $\mathbf{s}_k$, for $k < i$; and an anti-causal feedback filter, $\mathbb{A}$, performs SIC over residual interference caused by anti-causal symbols, $\mathbf{s}_k$, for $k > i$.

The feedforward filter can be modeled as a tapped-delay-line filter with N_1 anti-causal taps and N_2+1 causal taps, with the coefficient of the n-th tap, $\mathbf{F}_n$, being a $N_t \times N_r$ matrix, for $n = -N_1, \cdots, 0, \cdots, N_2$. The output of the feedforward filter, $\mathbf{v}_i \in \mathcal{C}^T$, can then be written as

$$\mathbf{v}_i = \sum_{n=-N_1}^{N_2} \mathbf{F}_n \mathbf{r}_{i-n} = \mathbb{F}\mathbf{y}_i, \tag{5}$$

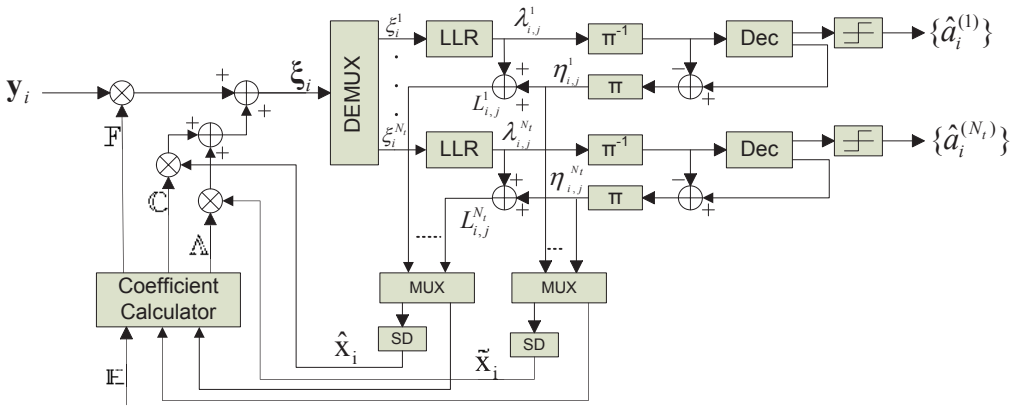

Figure 3.1. Block diagram of the SICE receiver.

where $\mathbb{F} = [\mathbf{F}_{N_2}, \mathbf{F}_{N_2-1} \cdots, \mathbf{F}_{-N_1}] \in \mathcal{C}^{N_t \times (N_1+N_2+1)N_r}$, and $\mathbf{y}_i = [\mathbf{r}_{i-N_2}^T, \mathbf{r}_{i-N_2+1}^T, \cdots, \mathbf{r}_{i+N_1}^T]^T \in \mathcal{C}^{(N_1+N_2+1)N_r}$. From the system model in (2), the vector $\mathbf{y}_i$ can be expressed as

$$\mathbf{y}_i = \mathbb{H}\mathbf{x}_i + \mathbf{z}_i \tag{6}$$

where $\mathbf{x}_i = [\mathbf{s}_{i-N_3}^T, \cdots, \mathbf{s}_{i+N_1}^T]^T \in \mathcal{S}^{(N_1+N_3+1)N_t}$ with $N_3 = N_2 + L - 1$, and $\mathbf{z}_i = [\mathbf{w}_{i-N_2}^T, \mathbf{w}_{i-N_2+1}^T \cdots, \mathbf{w}_{i+N_1}^T]^T \in \mathcal{C}^{(N_1+N_2+1)N_r}$ are the symbol vector and noise vector, respectively. The extended channel matrix $\mathbb{H}$ is of size $(N_1+N_2+1)N_r \times (N_1+N_3+1)N_t$, and it can be represented as

$$\mathbb{H} = \begin{bmatrix} \mathbf{H}_{L-1} & \cdots & \mathbf{H}_0 & & \mathbf{0} \\ & \ddots & & \ddots & \\ \mathbf{0} & & \mathbf{H}_{L-1} & \cdots & \mathbf{H}_0 \end{bmatrix}. \tag{7}$$

The output of the feedforward filter contains residual interference from both the causal symbols, $\mathbf{s}_k$, for $k = i - N_3, \cdots, i-1$, and the anti-causal ones, $\mathbf{s}_k$, for

$k = i+1, \cdots, i+N_1$. We propose to remove the residual interference by using the corresponding causal and anti-causal soft decisions from both the current and previous iterations with the help of the two feedback filters, $\mathbb{C}$ and $\mathbb{A}$. It should be noted that the SDFE in [9]- [11] only utilizes the causal soft decisions with $k < i$, yet it is clear from (5) and (6) that the output of the feedforward filter, $\mathbf{v}_i$, depends on both the causal and anti-casual components. We will show through both analysis and simulations that the anti-causal interferences are not negligible and they have significant impacts on the performance of the turbo detection, especially at later iterations.

Denote the causal and anti-causal soft decisions as $\hat{\mathbf{s}}_k \in \mathcal{C}^{N_t}$, for $k = i - N_3, \cdots, i-1$, and $\tilde{\mathbf{s}}_k \in \mathcal{C}^{N_t}$, for $k = i+1, \cdots, i+N_1$, respectively. Then the output of the two feedback filters can be written as $\sum_{n=1}^{N_3} \mathbf{C}_n \hat{\mathbf{s}}_{i-n} = \mathbb{C}\hat{\mathbf{x}}_i$ and $\sum_{n=-N_1}^{-1} \mathbf{A}_n \tilde{\mathbf{s}}_{i-n} = \mathbb{A}\tilde{\mathbf{x}}_i$, respectively, where $\mathbb{C} = [\mathbf{C}_{N_3}, \mathbf{C}_{N_3-1}, \cdots, \mathbf{C}_1] \in \mathcal{C}^{N_t \times N_3 N_t}$, $\mathbb{A} = [\mathbf{A}_{-1}, \mathbf{A}_{-2}, \cdots, \mathbf{A}_{-N_1}] \in \mathcal{C}^{N_t \times N_1 N_t}$, with the $N_t \times N_r$ matrices $\mathbf{C}_n$ and $\mathbf{A}_n$ being the tap coefficient matrices, and

$$\hat{\mathbf{x}}_i = [\hat{\mathbf{s}}_{i-N_3}^T, \cdots, \hat{\mathbf{s}}_{i-1}^T]^T \in \mathcal{C}^{N_3 N_t}, \tag{8}$$

$$\tilde{\mathbf{x}}_i = [\tilde{\mathbf{s}}_{i+1}^T, \cdots, \tilde{\mathbf{s}}_{i+N_1}^T]^T \in \mathcal{C}^{N_1 N_t}. \tag{9}$$

The soft decision vectors, $\hat{\mathbf{x}}_i$ and $\tilde{\mathbf{x}}_i$, can be calculated by combining soft information from the previous iteration and the current iteration, and details will be discussed in Section 4.1.

Combining the feedforward and feedback filters yields

$$\boldsymbol{\xi}_i = \mathbb{F}\mathbf{y}_i - \mathbb{C}\hat{\mathbf{x}}_i - \mathbb{A}\tilde{\mathbf{x}}_i. \tag{10}$$

3.2 FILTER DESIGN

The calculation of the SICE filters is discussed in this subsection. During the derivation, it is assumed that the transmitted symbols are independent in both the space and time domains, *i.e.*, $E[s_i^{(m)}(s_j^{(n)})^*] = 0$, for $m \neq n$ or $i \neq j$. Even though the coded bits are correlated in the time domain due to channel coding, the modulated symbols are generally uncorrelated with interleaver inserted between the channel encoder and modulator. There is no spatial correlation either at the absence of space time coding. Since the soft decisions are usually very close to their true values, it is reasonable to extend the assumption to the soft decisions, *i.e.*, $E[s_i^{(m)}(\hat{s}_j^{(n)})^*] = E[s_i^{(m)}(\tilde{s}_j^{(n)})^*] = E[\hat{s}_i^{(m)}(\tilde{s}_j^{(n)})^*] = 0$, for $m \neq n$ or $i \neq j$.

The coefficients of the feedforward and feedback filters are developed to minimize the mean squared error (MSE)

$$\sigma_i^2 = E[\|\mathbb{F}\mathbf{y}_i - \mathbb{C}\hat{\mathbf{x}}_i - \mathbb{A}\tilde{\mathbf{x}}_i - \mathbf{s}_i\|^2]. \tag{11}$$

Since σ_i^2 is quadratic in $\mathbb{F}$, $\mathbb{C}$, and $\mathbb{A}$, the MMSE solutions of the three filters can be calculated by setting the gradient of σ_i^2 with respect to the filters to 0. Performing partial differentiations of σ_i^2 with respect to $\mathbb{F}$, $\mathbb{C}$, and $\mathbb{A}$ yields

$$\frac{\partial \sigma_i^2}{\partial \mathbb{F}^H} = 2E\left[(\mathbb{F}\mathbf{y}_i - \mathbb{C}\hat{\mathbf{x}}_i - \mathbb{A}\tilde{\mathbf{x}}_i - \mathbf{s}_i)\,\mathbf{y}_i^H\right], \tag{12a}$$

$$\frac{\partial \sigma_i^2}{\partial \mathbb{C}^H} = -2E\left[(\mathbb{F}\mathbf{y}_i - \mathbb{C}\hat{\mathbf{x}}_i - \mathbb{A}\tilde{\mathbf{x}}_i - \mathbf{s}_i)\,\hat{\mathbf{x}}_i^H\right], \tag{12b}$$

$$\frac{\partial \sigma_i^2}{\partial \mathbb{A}^H} = -2E\left[(\mathbb{F}\mathbf{y}_i - \mathbb{C}\hat{\mathbf{x}}_i - \mathbb{A}\tilde{\mathbf{x}}_i - \mathbf{s}_i)\,\tilde{\mathbf{x}}_i^H\right]. \tag{12c}$$

We first discuss the calculations of the causal and non-causal feedback filters, $\mathbb{C}$ and $\mathbb{A}$. Setting (12b) and (12c) to 0 yields

$$\mathbb{C} = \mathbb{F}\mathbb{H}\mathbf{R}_{x\hat{x}}\mathbf{R}_{\hat{x}\hat{x}}^{-1}, \tag{13}$$

$$\mathbb{A} = \mathbb{F}\mathbb{H}\mathbf{R}_{x\tilde{x}}\mathbf{R}_{\tilde{x}\tilde{x}}^{-1}, \tag{14}$$

where the assumption of symbol-level space-time independence is used in the above equations, and

$$\mathbf{R}_{x\hat{x}} = E[\mathbf{x}_i \hat{\mathbf{x}}_i^H] \in \mathcal{C}^{NN_t \times N_3 N_t}, \tag{15a}$$

$$\mathbf{R}_{x\tilde{x}} = E[\mathbf{x}_i \tilde{\mathbf{x}}_i^H] \in \mathcal{C}^{NN_t \times N_1 N_t}, \tag{15b}$$

$$\mathbf{R}_{\hat{x}\hat{x}} = E[\hat{\mathbf{x}}_i \hat{\mathbf{x}}_i^H] \in \mathcal{C}^{N_3 N_t \times N_3 N_t}, \tag{15c}$$

$$\mathbf{R}_{\tilde{x}\tilde{x}} = E[\tilde{\mathbf{x}}_i \tilde{\mathbf{x}}_i^H] \in \mathcal{C}^{N_1 N_t \times N_1 N_t}. \tag{15d}$$

where $N = N_1 + N_3 + 1$.

In (13) and (14), the filters $\mathbb{C}$ and $\mathbb{A}$ are expressed as functions of the feedforward filter $\mathbb{F}$. Setting (12a) to 0 yields

$$\mathbb{F}\mathbb{H}\mathbf{R}_{xx}\mathbb{H}^H - \mathbb{C}\mathbf{R}_{x\hat{x}}^H\mathbb{H}^H - \mathbb{A}\mathbf{R}_{x\tilde{x}}^H\mathbb{H}^H = \mathbf{R}_{sx}\mathbb{H}^H, \tag{16}$$

where $\mathbf{R}_{xx} = E[\mathbf{x}_i \mathbf{x}_i^H] = \mathbf{I}_{NN_t}$ is a size $NN_t \times NN_t$ identity matrix, and $\mathbf{R}_{sx} \in \mathcal{C}^{N_t \times NN_t}$ is

$$\mathbf{R}_{sx} = E[\mathbf{s}_i \mathbf{x}_i^H] = [\mathbf{0}_{N_t \times N_3 N_t}, \mathbf{I}_{N_t}, \mathbf{0}_{N_t \times N_1 N_t}] \in \mathcal{C}^{N_t \times NN_t} \tag{17}$$

where $\mathbf{0}_{M \times N}$ is a size $M \times N$ all-zero matrix.

Substituting (13) and (14) into (16) leads to

$$\mathbb{F} = \mathbf{R}_{sx}\mathbb{H}^H \left[\sigma_w^2 \mathbf{I}_{(N_1+N_2+1)N_r} + \mathbb{H}\left(\mathbf{R}_{xx} - \mathbf{\Phi}_{\hat{x}} - \mathbf{\Phi}_{\tilde{x}}\right)\mathbb{H}^H\right]^{-1}. \tag{18}$$

where $\mathbf{\Phi}_{\hat{x}} = \mathbf{R}_{x\hat{x}}\mathbf{R}_{\hat{x}\hat{x}}^{-1}\mathbf{R}_{x\hat{x}}^H$, $\mathbf{\Phi}_{\tilde{x}} = \mathbf{R}_{x\tilde{x}}\mathbf{R}_{\tilde{x}\tilde{x}}^{-1}\mathbf{R}_{x\tilde{x}}^H$.

The evaluations of the filters in (13), (14), and (18) require the knowledge of the correlation matrices in (15), which in turn depend on the statistical properties of

the causal and anti-causal soft decisions. The calculations of the soft decisions and their statistical properties are presented in the next section.

4 SOFT DECISIONS

The causal and anti-causal soft decisions play a critical role in the design and performance of the proposed SICE. In this section, we first discuss the calculation of the soft decisions by using both the *a priori* LLR at the equalizer input and the extrinsic LLR at the equalizer output. Then the first and second order statistics of the soft decisions are obtained, and the results are used to construct the feedforward and feedback filters of the SICE.

4.1 CALCULATIONS OF THE SOFT DECISIONS

During the detection of $s_i^{(m)}$, the anti-causal soft decisions, $\tilde{s}_k^{(m)}$, for $k > i$, can be calculated by using the *a priori* LLR, $\eta_{k,j}^{(m)}$. The extrinsic LLR, $\lambda_{k,j}^{(m)}$, for $k > i$, at the output of the SICE is not yet available during the detection of $s_i^{(m)}$.

4.1.1 Anti-causal Soft Decisions. The anti-causal soft decisions can be calculated by utilizing the *a priori* LLR from the previous iterations. The *a priori* probability $P(s_k^{(m)} = \chi_q)$, for $k > i$ can then be calculated from the *a priori* LLR as

$$P(s_k^{(m)} = \chi_q) = \prod_{j=1}^{p} \frac{1}{2} \left[1 + d_{q,j} \tanh\left(\eta_{k,j}^{(m)}/2\right)\right], \tag{19}$$

where it is assumed that the binary sequence $[c_{q,1}, \cdots, c_{q,p}]$ is mapped to $\chi_q \in \mathcal{S}$, and $d_{q,j} = 1 - 2c_{q,j}$ is the bipolar representation of the coded bit $c_{q,j}$.

The anti-causal soft decision, $\tilde{s}_k^{(m)} = \sum_{q=1}^{Q} \chi_q P(s_k^{(m)} = \chi_q)$, can then be calculated as

$$\tilde{s}_k^{(m)} = \sum_{q=1}^{Q} \chi_q \prod_{j=1}^{p} \frac{1}{2} \left[1 + \tilde{d}_{q,j} \tanh\left(\eta_{k,j}^{(m)}/2\right)\right]. \tag{20}$$

4.1.2 Causal Soft Decisions. The causal soft decisions can be calculated by utilizing the output of the SICE, which can be modeled as a random vector. With

the filters given in (13), (14), and (18), we have the following results regarding the mean and auto-correlation function of $\boldsymbol{\xi}_i$ at the output of the SICE.

Proposition 1. *Under the assumption that the symbols (including both the original symbols and soft decisions) are independent in both the space and time domains, the output of the SICE given in* (10) *is a zero-mean random vector with the auto-correlation function given by*

$$\mathbf{R}_{\xi\xi} = E(\boldsymbol{\xi}_i \boldsymbol{\xi}_i^H) = \sum_{l=0}^{L-1} \mathbf{F}_{-l} \mathbf{H}_l \tag{21}$$

Proof. From (10), it is straightforward that $E[\boldsymbol{\xi}_i] = \mathbf{0}_{N_t}$. The auto-correlation function can be alternatively represented as

$$\mathbf{R}_{\xi\xi} = E[\boldsymbol{\xi}_i \mathbf{y}_i^H]\mathbb{F}^H - E[\boldsymbol{\xi}_i \hat{\mathbf{x}}_i^H]\mathbb{C}^H - E[\boldsymbol{\xi}_i \tilde{\mathbf{x}}_i^H]\mathbb{A}^H \tag{22}$$

From (13), it can be easily shown that $E[\boldsymbol{\xi}_i \hat{\mathbf{x}}_i^H] = \mathbf{0}_{N_t \times N_3 N_t}$ and $E[\boldsymbol{\xi}_i \tilde{\mathbf{x}}_i^H] = \mathbf{0}_{N_t \times N_1 N_t}$.

From (16), we have $E[\boldsymbol{\xi}_i \mathbf{y}_i^H] = E[\mathbf{s}_i \mathbf{y}_i^H] = \mathbf{R}_{sx}\mathbb{H}^H$. Combining the above results with (17) and (22) yields (21). □

Since $\boldsymbol{\xi}_i$ is random, it is assumed that $\boldsymbol{\xi}_i$ can be modeled as the output of a Gaussian channel. The m-th element of $\boldsymbol{\xi}_i$ can be alternatively expressed as [8]

$$\xi_{i,m} = g_{i,m} s_{i,m} + u_{i,m}, \tag{23}$$

where $g_{i,m}$ is a constant and $u_{i,m}$ is zero-mean Gaussian distributed with variance σ_m^2.

We have the following corollary regarding the values of $g_{i,m}$ and σ_m^2.

Corollary 2. *With the equivalent Gaussian channel model given in* (23)*, we have* $g_{i,m} = \sum_{l=0}^{L-1} \mathbf{f}_{-l,m} \mathbf{h}_{l,m}$*, with* $\mathbf{f}_{l,m}$ *being the* m*-th row of* $\mathbf{F}_l$ *and* $\mathbf{h}_{l,m}$ *the* m*-th column of* $\mathbf{H}_l$*, and* $\sigma_m^2 = g_{i,m}(1 - g_{i,m})$.

Proof. From (23), $E(\xi_{i,m}s^*_{i,m}) = g_{i,m}$. From (10), we have

$$E(\xi_{i,m}s^*_{i,m}) = \mathbb{F}_m \mathbb{H} E(\mathbf{x}_i s^*_{i,m}) = \sum_{l=0}^{L-1} \mathbf{f}_{-l,m}\mathbf{h}_{l,m}, \tag{24}$$

where $\mathbb{F}_m$ is the m-th row of $\mathbb{F}$.

From Proposition 1, $E(|\xi_{i,m}|^2) = g_{i,m}$. Therefore $g_{i,m}$ is a real number. From (23), we have

$$E(|\xi_{i,m}|^2) = g^2_{i,m} + \sigma^2_m. \tag{25}$$

Combining the above results yields $\sigma^2_m = g_{i,m}(1 - g_{i,m})$. □

We can then write the conditional probability density function (pdf) of $\xi_{i,m}$ as

$$p(\xi_{i,m}|s_{i,m}) = \frac{1}{\pi g_{i,m}(g_{i,m}-1)} \exp\left[-\frac{|\xi_{i,m} - g_{i,m}s_{i,m}|^2}{g_{i,m}(1-g_{i,m})}\right]. \tag{26}$$

The extrinsic LLR, $\lambda^{(m)}_{i,j} = \log \frac{P(\xi_{i,m}|c^{(m)}_{i,j}=0)}{P(\xi_{i,m}|c^{(m)}_{i,j}=1)}$, can be calculated as

$$\lambda^{(m)}_{i,j} = \log \frac{\sum_{\chi_o \in \mathcal{S}^0_j} \exp\left[-\rho_{i,m}(\chi_o)\right]}{\sum_{\chi_o \in \mathcal{S}^1_j} \exp\left[-\rho_{i,m}(\chi_o)\right]}, \tag{27}$$

where $\mathcal{S}^b_j \subset \mathcal{S}$ contains the symbols χ with the j-th mapped bit being $b \in \{0,1\}$, and $\rho_{i,m}(\chi_o) = \frac{|\xi_{i,m} - g_{i,m}\chi_o|^2}{g_{i,m}(1-g_{i,m})}$. Using the simplification provided in [15], $\lambda^{(m)}_{i,j}$ can be solved as Table 4.1 with the corresponding Gray mapping. However, The calculation of the extrinsic LLR requires the knowledge of $g_{i,m}$, which in turn depends on the statistical properties of the soft decisions as in (13), (14), and (18). The statistical properties of the soft decisions are discussed in the next subsection.

The causal and anti-causal soft decisions can be calculated by utilizing the combination of the extrinsic LLR, $\lambda^{(m)}_{i,j}$, and the *a priori* LLR, $\eta^{(m)}_{i,j}$. During the detection of the i-th symbol, both the *a priori* LLR, $\eta^{(m)}_{k,j}$ from the previous iteration,

Table 4.1. LLR simplifications for different constellations

QPSK:
- $\lambda_{i,1}^{(m)} \approx 2\sqrt{2}\mathrm{Re}\{\xi_i^{(m)}\}/(1-g_{i,m})$.
- $\lambda_{i,2}^{(m)} \approx 2\sqrt{2}\mathrm{Im}\{\xi_i^{(m)}\}/(1-g_{i,m})$.

8PSK:
- $\lambda_{i,1}^{(m)} \approx -4\sin(7\pi/8)\mathrm{Im}\{\xi_i^{(m)}\}/\left(1-g_{i,m}\right)$.
- $\lambda_{i,2}^{(m)} \approx -4\sin(7\pi/8)\mathrm{Re}\{\xi_i^{(m)}\}/\left(1-g_{i,m}\right)$.
- $\lambda_{i,3}^{(m)} \approx 1.0824(|\mathrm{Re}\{\xi_i^{(m)}\}| - |\mathrm{Im}\{\xi_i^{(m)}\}|)/\left(1-g_{i,m}\right)$.

16QAM:
- $\lambda_{i,1}^{(m)} \approx -4\mathrm{Re}\{\xi_i^{(m)}\}/(\sqrt{10}\,(1-g_{i,m}))$.
- $\lambda_{i,2}^{(m)} \approx (8g_{i,m} - 4\sqrt{10}|\mathrm{Re}\{\xi_i^{(m)}\}|)/(10\,(1-g_{i,m}))$.
- $\lambda_{i,3}^{(m)} \approx -4\mathrm{Im}\{\xi_i^{(m)}\}/(\sqrt{10}((1-g_{i,m}))$.
- $\lambda_{i,4}^{(m)} \approx (8g_{i,m} - 4\sqrt{10}|\mathrm{Im}\{\xi_i^{(m)}\}|)/(10\,(1-g_{i,m}))$.

and the extrinsic LLR $\lambda_{k,j}^{(m)}$ from the current iteration, $\forall k < i$, and they can be combined into the full LLR as $L_{k,j}^{(m)} = \lambda_{k,j}^{(m)} + \eta_{k,j}^{(m)}$.

Similar to (20), the causal soft decisions can then be calculated by using the full LLR as

$$\hat{s}_k^{(m)} = \sum_{q=1}^{Q} \chi_q \prod_{j=1}^{p} \frac{1}{2}\left[1 + d_{q,j}\tanh\left(L_{k,j}^{(m)}/2\right)\right]. \tag{28}$$

4.2 STATISTICAL PROPERTIES OF THE SOFT DECISIONS

As shown in (13), (14), and (18), the formulation of the filters require the cross-correlation matrices, $\mathbf{R}_{x\hat{x}}$ and $\mathbf{R}_{x\tilde{x}}$, and the auto-correlation matrices, $\mathbf{R}_{\hat{x}\hat{x}}$ and $\mathbf{R}_{\tilde{x}\tilde{x}}$.

With the space-time independence assumption, we can express the cross-correlation matrices, $\mathbf{R}_{x\hat{x}}$ and $\mathbf{R}_{x\tilde{x}}$ in (15), as

$$\mathbf{R}_{x\hat{x}} = \left[\begin{array}{cc} \mathbf{R}_{s\hat{s}}^T & \mathbf{0}_{(N_1+1)N_t \times N_3 N_t}^T \end{array} \right]^T \tag{29a}$$

$$\mathbf{R}_{x\tilde{x}} = \left[\begin{array}{cc} \mathbf{0}_{(N_3+1)N_t \times N_1 N_t}^T & \mathbf{R}_{s\tilde{s}}^T \end{array} \right]^T \tag{29b}$$

where $\mathbf{R}_{s\hat{s}} \in \mathcal{C}^{N_3 N_t \times N_3 N_t}$ and $\mathbf{R}_{s\tilde{s}} \in \mathcal{C}^{N_1 N_t \times N_1 N_t}$ are diagonal matrices defined as

$$\mathbf{R}_{s\hat{s}} = \text{diag}\left[\alpha_{s\hat{s}}^{(1)}, \cdots, \alpha_{s\hat{s}}^{(N_t)} | \cdots | \alpha_{s\hat{s}}^{(1)}, \cdots, \alpha_{s\hat{s}}^{(N_t)}\right] \tag{30a}$$

$$\mathbf{R}_{s\tilde{s}} = \text{diag}\left[\alpha_{s\tilde{s}}^{(1)}, \cdots, \alpha_{s\tilde{s}}^{(N_t)} | \cdots | \alpha_{s\tilde{s}}^{(1)}, \cdots, \alpha_{s\tilde{s}}^{(N_t)}\right] \tag{30b}$$

with

$$\alpha_{s\hat{s}}^{(m)} = E[s_i^{(m)} \hat{s}_i^{(m)*}] = \frac{1}{Q} \sum_{q=1}^{Q} \chi_q E[\hat{s}_i^{(m)*} | s_i^{(m)} = \chi_q] \tag{31a}$$

$$\alpha_{s\tilde{s}}^{(m)} = E[s_i^{(m)} \tilde{s}_i^{(m)*}] = \frac{1}{Q} \sum_{q=1}^{Q} \chi_q E[\tilde{s}_i^{(m)*} | s_i^{(m)} = \chi_q], \tag{31b}$$

where $P(s_i^{(m)}) = \frac{1}{Q}$ is used in the above equations.

The auto-correlation matrices, $\mathbf{R}_{\hat{x}\hat{x}} \in \mathcal{C}^{N_3 N_t \times N_3 N_t}$ and $\mathbf{R}_{\tilde{x}\tilde{x}} \in \mathcal{C}^{N_1 N_t \times N_1 N_t}$, are diagonal matrices, and they can be expressed as

$$\mathbf{R}_{\hat{x}\hat{x}} = \text{diag}\left[\alpha_{\hat{s}\hat{s}}^{(1)}, \cdots, \alpha_{\hat{s}\hat{s}}^{(N_t)} | \cdots | \alpha_{\hat{s}\hat{s}}^{(1)}, \cdots, \alpha_{\hat{s}\hat{s}}^{(N_t)}\right], \tag{32a}$$

$$\mathbf{R}_{\tilde{x}\tilde{x}} = \text{diag}\left[\alpha_{\tilde{s}\tilde{s}}^{(1)}, \cdots, \alpha_{\tilde{s}\tilde{s}}^{(N_t)} | \cdots | \alpha_{\tilde{s}\tilde{s}}^{(1)}, \cdots, \alpha_{\tilde{s}\tilde{s}}^{(N_t)}\right], \tag{32b}$$

where

$$\alpha_{\hat{s}\hat{s}}^{(m)} = E\left[|\hat{s}_i^{(m)}|^2\right] = E\left[|\hat{s}_i^{(m)}|^2 \middle| s_i^{(m)} = \chi_q\right] \tag{33a}$$

$$\alpha_{\tilde{s}\tilde{s}}^{(m)} = E\left[|\tilde{s}_i^{(m)}|^2\right] = E\left[|\tilde{s}_i^{(m)}|^2 \middle| s_i^{(m)} = \chi_q\right] \tag{33b}$$

As in (31) and (33), the correlation coefficients, $\alpha_{s\hat{s}}^{(m)}$, $\alpha_{s\tilde{s}}^{(m)}$, $\alpha_{\hat{s}\tilde{s}}^{(m)}$, and $\alpha_{\tilde{s}\tilde{s}}^{(m)}$, depend on the first and second conditional moments of $\hat{s}_i^{(m)}$ and $\tilde{s}_i^{(m)}$.

4.2.1 Conditional Moments of the Anti-causal Soft Decisions $\tilde{s}_i^{(m)}$. To facilitate the calculation of the conditional moments, we adopt the assumption that the *a priori* LLR, $\eta_{i,j}^{(m)}$, can be modeled as coming from an equivalent AWGN channel with SNR $\gamma_m/2$ [20]

$$\eta_{i,j}^{(m)} = d_{i,j}^{(m)}\gamma_m + v_{i,j}^{(m)}, \tag{34}$$

where $v_{i,j}^{(m)} \sim \mathcal{N}(0, 2\gamma_m)$. The value of γ_m can be estimated from the *a priori* LLR with the maximum-likelihood estimation as [8]

$$\hat{\gamma}_m = \sqrt{1 + \frac{1}{pN}\sum_{i=1}^{N}\sum_{j=1}^{p}|\eta_{i,j}^{(m)}|^2} - 1. \tag{35}$$

Since the anti-causal soft decision $\tilde{s}_i^{(m)}$ is a function of $\eta_{i,j}^{(m)}$ as in (20), $\tilde{s}_i^{(m)}$ can also be modeled as a random variable. The conditional expectation of $\tilde{s}_i^{(m)}$ can then be calculated as

$$E\left[\tilde{s}_i^{(m)}|s_i^{(m)} = \chi_o\right] = \sum_{q=1}^{Q}\chi_q\prod_{j=1}^{p}\frac{1}{2}\left\{1 + d_{q,j}E\left[\tanh\left(\eta_{i,j}^{(m)}/2\right)\middle|\,\chi_o\right]\right\}, \tag{36}$$

where the expectation is performed with respect to $\eta_{i,j}^{(m)}$, and $\eta_{i,j}^{(m)} \sim \mathcal{N}(d_{o,j}^{(m)}\gamma_m, 2\gamma_m)$, with $d_{o,j}^{(m)}$ being the bipolar representation of the j-th bit of the vector mapped to $\chi_o \in \mathcal{S}$. The space-time independence of the interleaved coded bits are used in the above equation.

Similarly, the conditional second moment of $\tilde{s}_i^{(m)}$ can be calculated as

$$E\left[|\tilde{s}_i^{(m)}|^2|s_i^{(m)}=\chi_o\right]=\sum_{q_1=1}^{Q}\sum_{q_2=1}^{Q}\chi_{q_1}\chi_{q_2}^{*}\prod_{j=1}^{p}\frac{1}{4}\left\{1+\tilde{d}_{q_1,j}\tilde{d}_{q_2,j}E\left[\tanh^2\left(\eta_{i,j}^{(m)}/2\right)|\chi_o\right]+(\tilde{d}_{q_1,j}+\tilde{d}_{q_2,j})E\left[\tanh\left(\eta_{i,j}^{(m)}/2\right)|\chi_o\right]\right\} \quad (37)$$

The expectations, $E\left[\tanh\left(\eta_{i,j}^{(m)}/2\right)\middle|\,\chi_o\right]$ and $E\left[\tanh^2\left(\eta_{i,j}^{(m)}/2\right)\middle|\,\chi_o\right]$, in (36) and (37) elude closed-form expressions. However, they can be easily evaluated numerically offline and tabulated as functions of γ_m.

4.2.2 Conditional Moments of the Causal Soft Decisions $\hat{s}_i^{(m)}$. The causal soft decision $\hat{s}_i^{(m)}$ is a function of $L_{i,j}^{(m)}=\lambda_{i,j}^{(m)}+\eta_{i,j}^{(m)}$. Therefore, the second order statistics of $\hat{s}_i^{(m)}$ depends on the statistical properties of both $\lambda_{i,j}^{(m)}$ and $\eta_{i,j}^{(m)}$.

The conditional moments, $E\left[\hat{s}_i^{(m)}|s_i^{(m)}=\chi_o\right]$ and $E\left[|\hat{s}_i^{(m)}|^2|s_i^{(m)}=\chi_o\right]$ can be calculated by replacing $\eta_{i,j}^{(m)}$ with $\eta_{i,j}^{(m)}+\lambda_{i,j}^{(m)}$ in (36) and (37), respectively.

Therefore, the evaluations of the second order statistics require the knowledge of the following two quantities

$$E\left[\tanh\left(\eta_{i,j}^{(m)}/2+\lambda_{i,j}^{(m)}/2\right)|\chi_o\right], \quad (38a)$$

$$E\left[\tanh^2\left(\eta_{i,j}^{(m)}/2+\lambda_{i,j}^{(m)}/2\right)|\chi_o\right], \quad (38b)$$

where both $\eta_{i,j}^{(m)}\sim\mathcal{N}(d_{o,j}^{(m)}\gamma_m,\gamma_m/2)$ and $\lambda_{i,j}^{(m)}$ are random variables. The extrinsic LLR $\lambda_{i,j}^{(m)}$ is a function of the filter output $\xi_{i,m}$, which is modeled as a Gaussian random variable as described in (26). The conditional pdf of $p(\lambda_{i,j}^{(m)}|\chi_o)$ can be evaluated numerically by combining (26) and (27). The first and second order moments of $\tanh\left(\eta_{i,j}^{(m)}/2+\lambda_{i,j}^{(m)}/2\right)$ can then be numerically calculated by using (38), the Gaussian pdf of $\eta_{i,j}^{(m)}$, and the pdf of $\lambda_{i,j}^{(m)}$.

Once the results in (38) are obtained, then the conditional moments of $\hat{s}_i^{(m)}$ can be obtained by replacing $\eta_{i,j}^{(m)}$ with $\eta_{i,j}^{(m)}+\lambda_{i,j}^{(m)}$ in (36) and (37).

The evaluations of the conditional moments, $\alpha_{\hat{s}\hat{s}}^{(m)}$ and $\alpha_{\tilde{s}\tilde{s}}^{(m)}$, requires the pdf of the filter output $\xi_{i,m}$, which in turn depends on $g_{i,m}$ and the feedforward filter $\mathbb{F}$. On the other hand, the calculation of $\mathbb{F}$ requires the knowledge of $\alpha_{\hat{s}\hat{s}}^{(m)}$ and $\alpha_{\tilde{s}\tilde{s}}^{(m)}$. We address this problem by using a linear MMSE at the first iteration to initialize the values of $\alpha_{\hat{s}\hat{s}}^{(m)}$ and $\alpha_{\tilde{s}\tilde{s}}^{(m)}$, and the proposed SICE is employed starting from the second iterations.

The detailed procedure of the proposed SICE is summarized in Table II.

4.3 SPECIAL CASES

4.3.1 $\eta_{k,j}^{(m)} \to 0$ and $\lambda_{k,j}^{(m)} \to 0$. Since $\tanh(0) = 0$, it can be seen from (19) and (20) that $\tilde{s}_k^{(m)} = \frac{1}{Q}\sum_{q=1}^{Q} \chi_q = 0$ due to the constellation symmetry. Similarly, $\hat{s}_k^{(m)} = 0$ from (28). As a result, $\mathbf{R}_{x\hat{x}}$ and $\mathbf{R}_{x\tilde{x}}$ are all-zero matrices. In this case, $\mathbb{C}$ in (13) and $\mathbb{A}$ in (14) are all-zero matrices, and $\mathbb{F}$ in (18) degrades to $\mathbf{R}_{sx}\mathbb{H}^H \left[\sigma_w^2 \mathbf{I}_{(N_1+N_2+1)N_r} + \mathbb{H}\mathbb{H}^H\right]^{-1}$. Therefore, the SICE degrades to a linear MMSE receiver. This corresponds to the initial iteration, when neither causal nor anti-causal soft decisions are available. **4.3.2 $\eta_{k,j}^{(m)} \to 0$ and $\lambda_{k,j}^{(m)} \to \infty$.** In this case, the anti-causal soft decisions $\tilde{s}_k^{(m)} = 0$ as in the previous case, and $\mathbf{R}_{x\tilde{x}}$ and $\mathbb{A}$ are all-zero matrices. Since $\lambda_{k,j}^{(m)} \to \infty$, the SICE has the ideal output, i.e., $\hat{s}_k^{(m)} = s_k^{(m)}$. As a result, there is perfect cancelation of the causal symbols. On the other hand, there will always be residual interference from the anti-causal symbols. Consequently, the performance will suffer from the residual anti-causal interference, even at later iterations when the SICE has very accurate outputs. This case corresponds to the SDFE in [10], where the interference from the anti-causal symbols is not considered.

4.3.3 $\eta_{k,j}^{(m)} \to \infty$ and $\lambda_{k,j}^{(m)} \to \infty$. When both the *a priori* and extrinsic information are infinity, this means the SICE has ideal knowledge of the symbols at the input, $\tilde{s}_k^{(m)} = s_k^{(m)}$ and it can produce an ideal estimate of the transmitted symbols, $\hat{s}_k^{(m)} = s_k^{(m)}$. Therefore, both the anti-causal and causal interference can be

Table 4.2. SICE Turbo Detection Algorithm

THE FIRST ITERATION:
- Set $\mathbb{F} = \mathbf{R}_{sx}\mathbb{H}^H[\sigma_w^2\mathbf{I}_{(N_1+N_2+1)N_r} + \mathbb{H}\mathbb{H}^H]^{-1}$, $\mathbb{C} = \mathbf{0}_{N_t\times N_3N_t}$, $\mathbb{A} = \mathbf{0}_{N_t\times N_tN_1}$ and
  $\eta_{i,j} = L_{i,j} = 0\ \forall i,j$
- Calculate $\boldsymbol{\xi}_i$ using equation (10)
- For $m = 1 : N_t$
  - Calculate $g_{i,m}$ with Corollary 2
  - Calculate $\lambda_{i,j}^{(m)}$ using Table 4.1
  - Input $\lambda_{i,j}^{(m)}$ to channel decoder, and obtain $\eta_{i,j}^{(m)}$ at the output of the channel decoder.
- End

THE k–th **ITERATION** ($k > 1$)**:**
- For $m = 1 : N_t$
  - With the assumption in eqn. (34), calculate the conditional moments of the anti-causal soft decisions $\alpha_{s\tilde{s}}^m$ and $\alpha_{\tilde{s}\tilde{s}}^m$ using (31), (33), (36), and (37)
  - With $g_{i,m}$ and the distribution of $\eta_{i,j}^{(m)}$ from the previous iteration, numerically calculate the conditional moments of the causal soft decisions $\alpha_{s\hat{s}}^{(m)}$ and $\alpha_{\hat{s}\hat{s}}^{(m)}$ using (31), (33), (36), (37), and (38)
- End
- Calculate $\mathbb{C}$, $\mathbb{A}$ and $\mathbb{F}$ using eqns. (13), (14) and (18) with $\mathbf{R}_{x\hat{x}}$, $\mathbf{R}_{x\tilde{x}}$, $\mathbf{R}_{\hat{x}\hat{x}}$ and $\mathbf{R}_{\tilde{x}\tilde{x}}$
- Calculate the anti-causal soft decision, $\tilde{s}_k^{(m)}$ from $\eta_{k,j}^{(m)}$ using eqn. (20) and initialize the causal soft Decisions $\hat{\mathbf{x}}_i$=$\mathbf{0}_{N_3N_t\times 1}$
- Calculate $g_{i,m}$ with Corollary 2.
- For i=1 : Block length
  - Update $\tilde{\mathbf{x}}_i$ and calculate $\boldsymbol{\xi}_i$ using eqn. (10)
  - Calculate $\lambda_{i,j}^{(m)}$ using Table 4.1 and update $\hat{\mathbf{x}}_i$ through $L_{i,j}^{(m)}$ using eqn. (20)
- End
- For $m = 1 : N_t$
  - Input $\lambda_{i,j}^{(m)}$ to channel decoder, and obtain $\eta_{i,j}^{(m)}$ at the output of the channel decoder.
- End

perfectly removed. As a result, the proposed SICE degrades to a matched filter. This performance can actually be approached during later iterations with the proposed SICE equalizer, when the soft information becomes more and more reliable.

5 CONVERGENCE ANALYSIS VIA EXIT CHART

The EXIT chart analysis of the proposed SICE is studied in this section. In turbo detection, the SICE iteratively exchanges soft information with the channel decoder. The EXIT chart demonstrates the evolution of the soft information as the iteration progresses. It provides insights on the convergence behavior of the SICE-based turbo detection.

In the EXIT chart analysis, the quality of the soft information is measured by using the mutual information between a coded bit and the corresponding LLR of the bit. The mutual information, $\mathcal{I}_{\mathrm{I}}$, between the bit, $d \in \{-1, 1\}$, and the *a priori* LLR, η, at the SICE input can be written as [20]

$$\mathcal{I}_{\mathrm{I}} = \frac{1}{2} \sum_{d \in \{\pm 1\}} \int_{-\infty}^{\infty} p_{\eta|d}(l|d) \log_2 \left(\frac{2 p_{\eta|d}(l|d)}{p_{\eta|d}(l|-1) + p_{\eta|d}(l|+1)} \right) dl \tag{39}$$

where $p_{\eta|d}(l|d)$ is the pdf of the *a priori* LLR conditioned on the coded bit d. $\mathcal{I}_{\mathrm{I}} = 0$ means no *a priori* information and $\mathcal{I}_{\mathrm{I}} = 1$ means ideal *a priori* information. Similarly, the mutual information, $\mathcal{I}_{\mathrm{O}}$, between the coded bit, d, and the extrinsic LLR, λ, at the output of the SICE is defined in a similar manner by replacing $p_{\eta|d}(l|d)$ with $p_{\lambda|d}(l|d)$ in (39), where $p_{\lambda|d}(l|d)$ is the conditional pdf of the extrinsic LLR λ.

For the *a priori* LLR at the SICE input, the LLR $\eta_{i,j}^{(m)}$ conditioned on the coded bit $d_{i,j}^{(m)}$ is modeled as a Gaussian random variable with mean $d_{i,j}^{(m)}$ and variance $2\gamma_m$ as shown in (34). The extrinsic LLR, $\lambda_{i,j}^{(m)}$, at the output of the SICE is a function of the filter output, $\xi_{i,m}$, which in turn is modeled as a Gaussian random variable as described in (26). During the EXIT chart analysis, the conditional pdf of the extrinsic information is evaluated numerically through histogram.

During the EXIT chart analysis, the SICE or decoder is viewed as a mutual information transfer device. Given *a priori* mutual information $\mathcal{I}_{\mathrm{I}}$ at the input, the

equalizer generates a new extrinsic mutual information $\mathcal{I}_{\mathrm{O}}$ at the output, with $\mathcal{I}_{\mathrm{O}} > \mathcal{I}_{\mathrm{I}}$ in general.

For a MIMO system, the analysis of the mutual information transfer function of the SICE is more complicated because there are N_t mutually interfering data streams. Due to the mutual interference, we cannot simply divide the system into N_t independent mutual information transfer devices, because the extrinsic output of one data stream depends on the *a priori* inputs of all the data streams. The mutual information transfer function should be represented as a function with N_t-dimensional signals at both the input and output as, $[\mathcal{I}_{\mathrm{O}1}, \cdots, \mathcal{I}_{\mathrm{O}M}]^T = \mathbf{T}([\mathcal{I}_{\mathrm{I}1}, \cdots, \mathcal{I}_{\mathrm{I}M}]^T)$, where $\mathbf{T} : [0,1]^{N_t} \rightarrow [0,1]^{N_t}$ is the mutual information transfer function, and $\mathcal{I}_{\mathrm{I}m}$ and $\mathcal{I}_{\mathrm{O}m}$ are, respectively, the input and output mutual information of the m-th data stream. When $N_t = 1$, the mutual information transfer can be represented with a single curve as in the conventional EXIT chart analysis. When $N_t = 2$, the mutual information transfer for each output is in the form of a two-dimension surface. When $N_t > 2$, it would be impossible to visualize the mutual information transfer. In this case, we can still show part of the information transfer by projecting the function onto an one- or two-dimension space.

The EXIT chart analysis is performed for a 2×2 MIMO system with 5 channel taps as

$$\begin{aligned} h_{1,1} &= [-0.21, -0.5, 0.72, 0.36, 0.21] \\ h_{1,2} &= [0.407, 0.815, 0.407, 0, 0] \\ h_{2,1} &= [0.227, 0.460, 0.688, 0.460, 0.227] \\ h_{2,2} &= [0.5, 0.5, 0.5, 0.5, 0.5] \end{aligned} \tag{40}$$

where $h_{1,1}$, $h_{1,2}$ and $h_{2,1}$ are similar to the ones provided in [21] with little revision. It should be noted that the channels are normalized to unit energy during the simulations. The EXIT chart is evaluated for various modulation schemes, such as 8PSK and 16QAM, with both convolutional and low-density parity-check (LDPC) coding schemes under different SNR values. With the convolutional encoder, the transmitted binary bits are encoded by a rate $R = 1/2$ convolutional encoder with a generator polynomial $G = [7, 5]_8$. For the LDPC code, the code rate is $R = 1/2$. Since the block length is 1024 Q-ary modulation symbols, the size of the parity check matrix is $512 \log_2 Q \times 1024 \log_2 Q$, with 4 ones on each row, and 2 ones on each column. The parity check matrix of the regular LDPC is generated with the scheme presented in [23]. A size 21,120 random interleaver is used after the channel encoder.

Fig. 5.1 shows the three-dimension EXIT chart for the second transmitted data stream with 8PSK modulation. In the EXIT chart, the mutual information transfer functions of various equalizers and the mutual information transfer function of the channel decoder are placed in the same figure, with the horizonal axis representing the inputs to the equalizers ($\mathcal{I}_{\mathrm{I}i}^{\mathrm{E}}$) or the output of the decoder ($\mathcal{I}_{\mathrm{O}i}^{\mathrm{D}}$), for $i = 1, 2$, and the vertical axis representing the output of the equalizers ($\mathcal{I}_{\mathrm{O2}}^{\mathrm{E}}$) or the input to the decoder ($\mathcal{I}_{\mathrm{I2}}^{\mathrm{D}}$) related to the data stream from the second transmit antenna. MAP channel decoding is used for all systems, and the mutual information transfer function of the channel decoder, denoted as MAP in the figure, is the same for all data streams. As can be seen from the figure, the two-dimension surface of the SICE is generally above that of the SDFE [10], and the approximate MMSE linear equalizer (MMSE-LE) [2] has the lowest mutual information transfer surface. This means for given two dimensional input mutual information, the output mutual information of the SICE is larger than those produced by the SDFE or linear MMSE. As a result, the proposed SICE converges faster than the other two equalization schemes. The

result can also be verified through the results in Fig. 5.2, which shows the projection of the three dimensional EXIT chart onto the $\mathcal{I}_{\mathrm{I2}}^{\mathrm{E}}$-$\mathcal{I}_{\mathrm{O2}}^{\mathrm{E}}$ plane.

To better visualize the behaviors of the various equalizers, Fig. 5.3 shows the one-dimension mutual information transfer curve by averaging $\mathcal{I}_{\mathrm{O2}}^{\mathrm{E}}$ over all the input values of $\mathcal{I}_{\mathrm{I1}}^{\mathrm{E}}$, i.e., $\bar{\mathcal{I}}_{\mathrm{O2}}^{\mathrm{E}} = \int_0^1 T_2(\mathcal{I}_{\mathrm{I1}}^{\mathrm{E}}, \mathcal{I}_{\mathrm{I2}}^{\mathrm{E}}) d\mathcal{I}_{\mathrm{I1}}^{\mathrm{E}}$. The average output mutual information, $\bar{\mathcal{I}}_{\mathrm{O2}}^{\mathrm{E}}$, is shown as a function of $\mathcal{I}_{\mathrm{I2}}^{\mathrm{E}}$ in Fig. 5.3. The SICE and the MAP decoder curves form a wider tunnel than those formed with the SDFE or the approximate MMSE-LE. The arrowed black traces in the figure demonstrate the mutual information evolution of the turbo equalizer with SICE. The vertical trace represents the mutual information improvement contributed by the equalizer, and horizontal trace corresponds to the contribution from the MAP decoder. As indicated in the figure, the SICE converges in 4 iterations. More importantly, as the iteration progresses, the SICE can almost reach the ideal output with $\bar{\mathcal{I}}_{\mathrm{O2}}^{\mathrm{E}} = 0.95$ when the input $\mathcal{I}_{\mathrm{I2}}^{\mathrm{E}} = 1$. On the other hand, the highest mutual information that can be achieved by the SDFE and the MMSE-LE is only 0.79 and 0.60, respectively. This means that, even with ideal soft information at the input, the SDFE or MMSE-LE can never produce ideal soft information at their respective outputs, regardless of the number of iterations. The performance loss of SDFE is mainly due to the overlook of the anti-casual interference, which limits the quality of the soft information at the output of the SDFE. On the other hand, the proposed SICE can almost achieve the ideal matched filter bound as long as the quality of the soft information at the input is good enough, which can be obtained with more iterations. A similar observation is also obtained for systems with 16QAM modulation and LDPC code as shown in Fig. 5.4, where the LDPC decoding is performed with the log-domain sum-product algorithm [22].

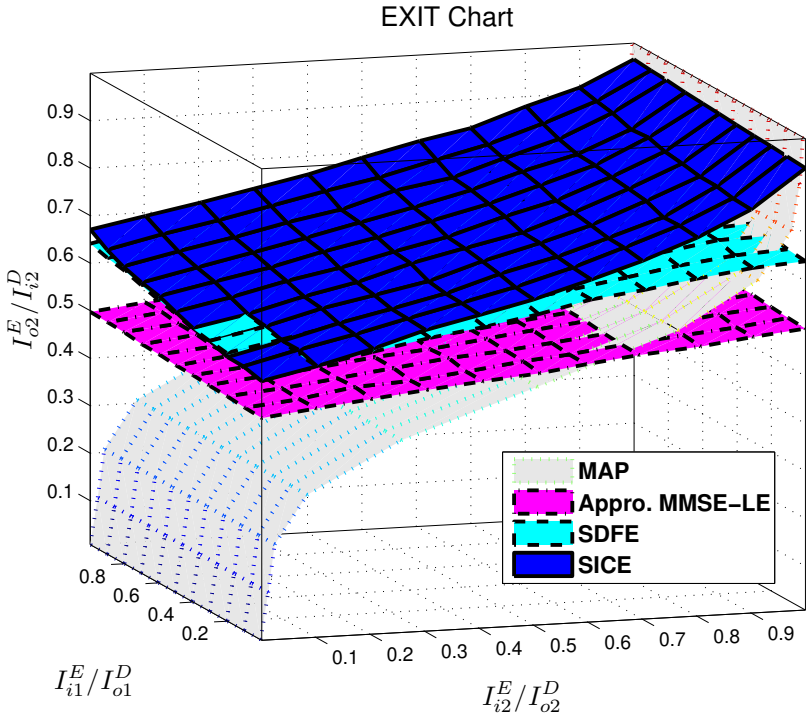

Figure 5.1. EXIT chart for Tx 2 with 8PSK constellation and convolutional code (SNR=18 dB).

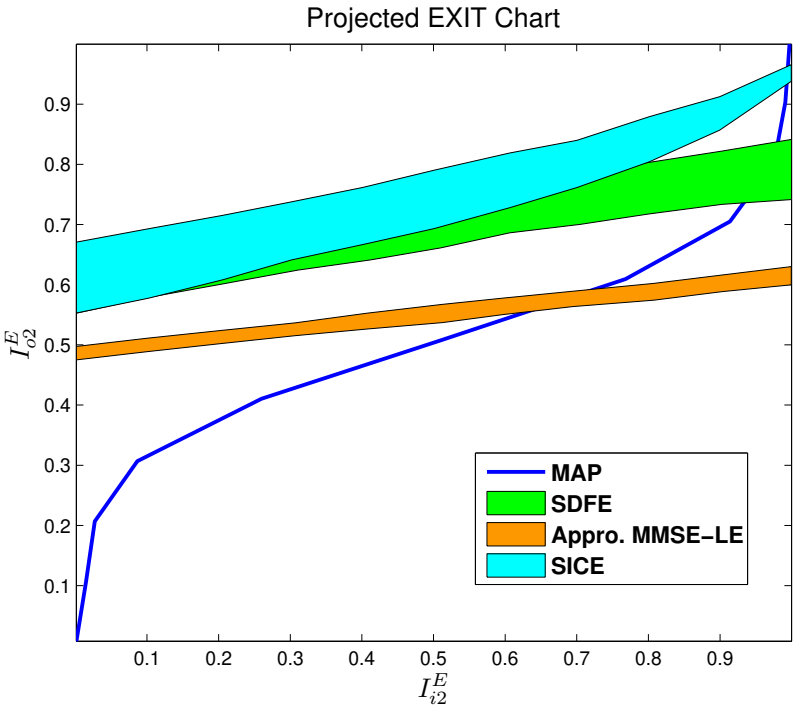

Figure 5.2. Projected EXIT chart for Tx 2 with 8PSK constellation and convolutional code (SNR=18 dB).

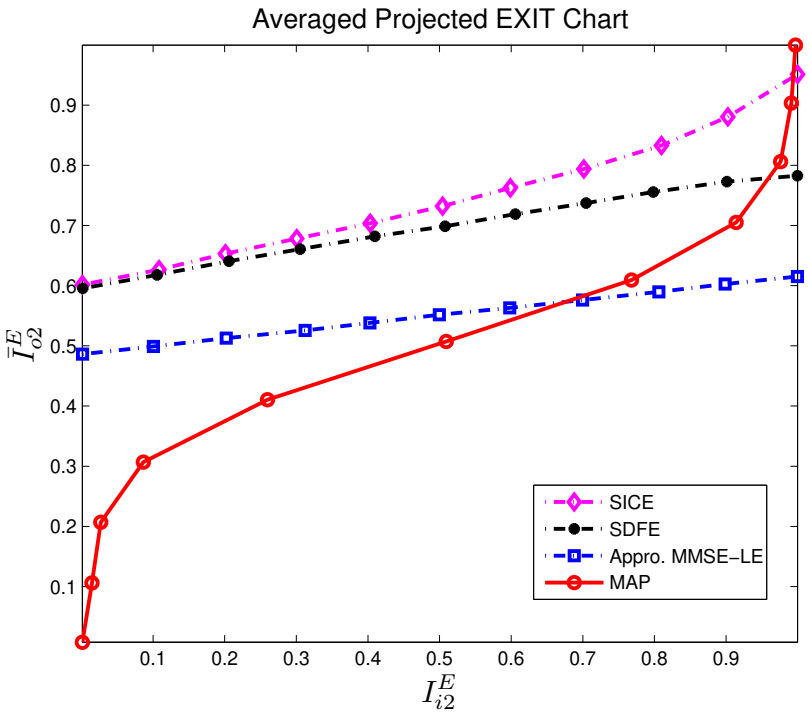

Figure 5.3. Average projected EXIT chart for Tx 2 with 8PSK constellation and convolutional code (SNR=18dB).

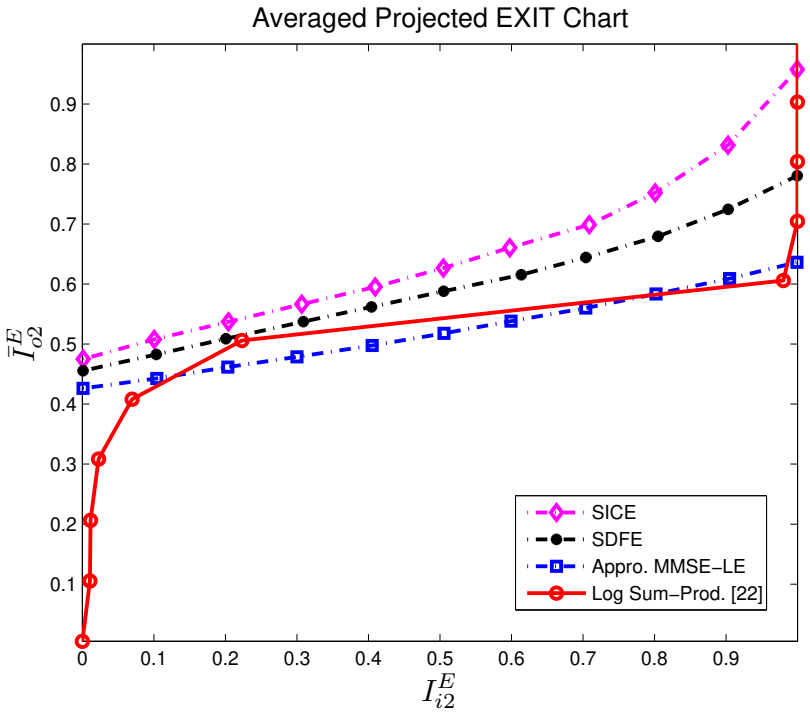

Figure 5.4. Average projected EXIT chart for Tx 2 with 16QAM Constellation and LDPC code (SNR = 20 dB).

6 SIMULATION RESULTS

The bit error rate (BER) performance of the proposed turbo SICE receiver is evaluated in this section with simulations. The MIMO channels used in the simulations are the same as the ones used during the EXIT chart analysis. The BER performance of systems with the proposed SICE receiver will be compared to those with the approximate MMSE-LE receivers [2] and SDFE receivers [10]. For all the equalizers, we have $N_1 = 9$ and $N_2 = 5$.

For systems with convolutional codes, Figs. 6.1, 6.2, and 6.3 show the BER performance of three different equalizers with QPSK, 8PSK, and 16QAM modulations, respectively. The frame length is 1024 symbols for all modulation schemes. In the first iteration, all three equalizers have the same performance due to the lack of *a priori* information. After the first iteration, the SICE achieves significant performance gains over the other two equalizers for all system configurations, and the performance improvement increases for higher constellation sizes. At the BER $= 3 \times 10^{-5}$ and after the fifth iteration, the SICE outperforms the SDFE by 1.8 dB, 2.5 dB, and 3.0 dB, for systems with QPSK, 8PSK, and 16QAM modulations, respectively. The performance improvement over the approximate MMSE-LE is much bigger. For example, at BER $= 10^{-2}$, the SICE outperforms the approximate MMSE-LE by 4.8 dB after the fifth iteration with 16QAM modulation.

The BER performance of systems with LDPC codes are shown in Figs. 6.4, 6.5 and 6.6, for systems with QPSK, 8PSK and 16QAM modulations, respectively. The transmitted binary bits are encoded by an LDPC code with a code rate $R = 1/2$. The LDPC decoding is performed with the log-domain sum-product algorithm [22]. The block length is chosen as 1024 symbols for all three modulations. So the binary codeword lengthes for QPSK, 8PSK and 16QAM are 2048, 3072 and 4096, respectively. Before mapping the coded bits into different constellation sets, they

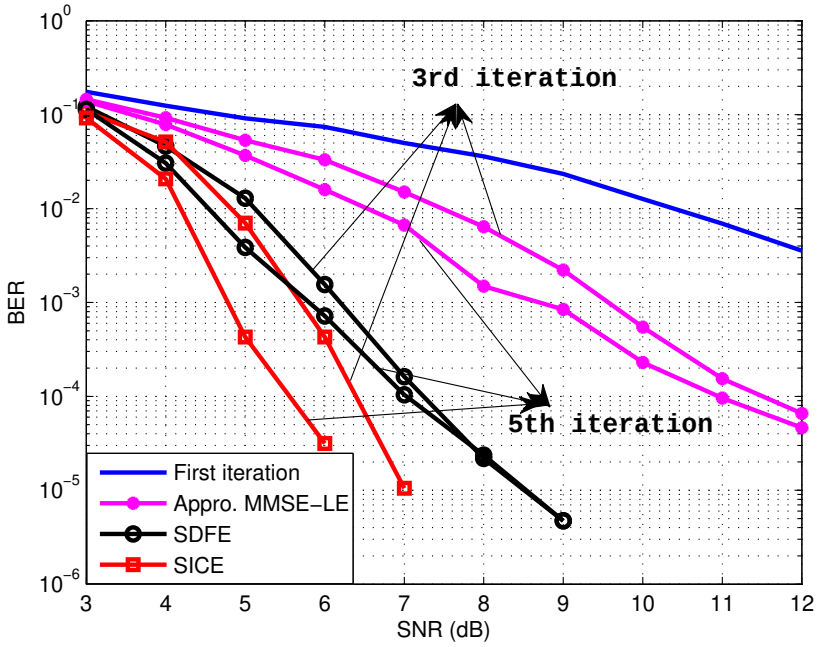

Figure 6.1. QPSK BER performance with convolutional code.

are passed through random interleavers with size equal to the codeword length for each modulation. Similar to the results for systems with convolutional codes, SICE with LDPC codes achieve significant performance gains over the other two equalizers, especially for systems with higher modulation levels. For all modulation schemes, the SICE performance after the 3rd iteration is better than the SDFE performance after the 5th iteration, and this verifies the fast convergence of the SICE algorithm. For systems with 16QAM at BER = 10^{-4}, after the 5th iteration, the SICE outperforms the SDFE and approximate LE-MMSE by 1.9 dB and 4.1 dB, respectively.

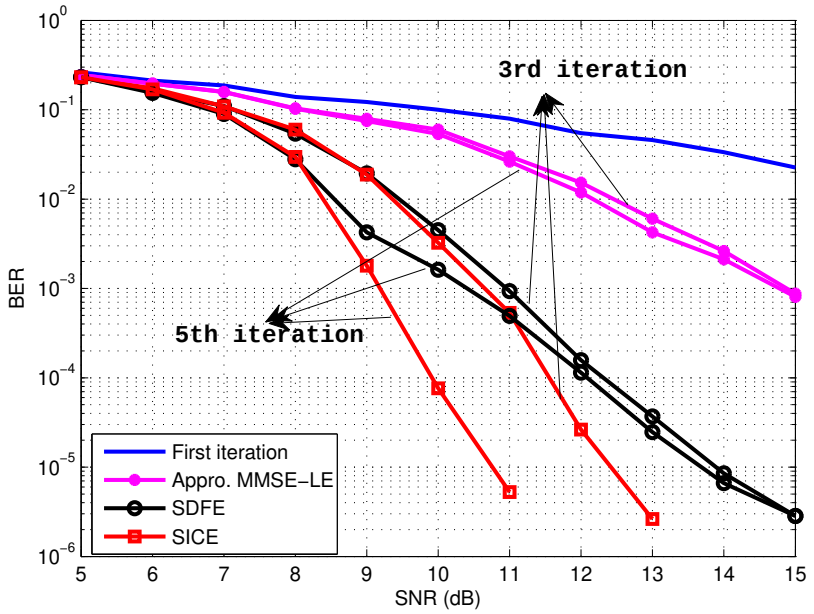

Figure 6.2. 8PSK BER performance with convolutional code.

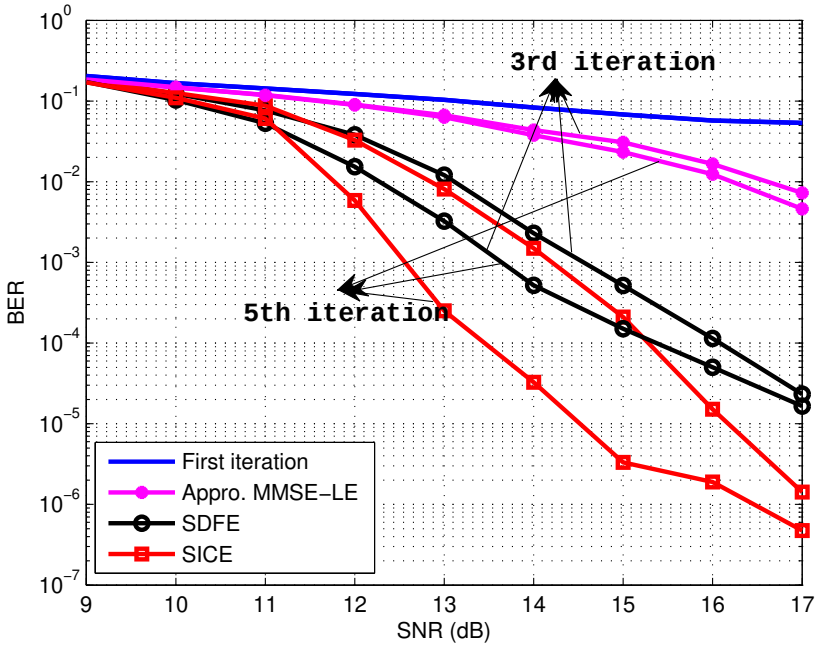

Figure 6.3. 16QAM BER performance with convolutional code.

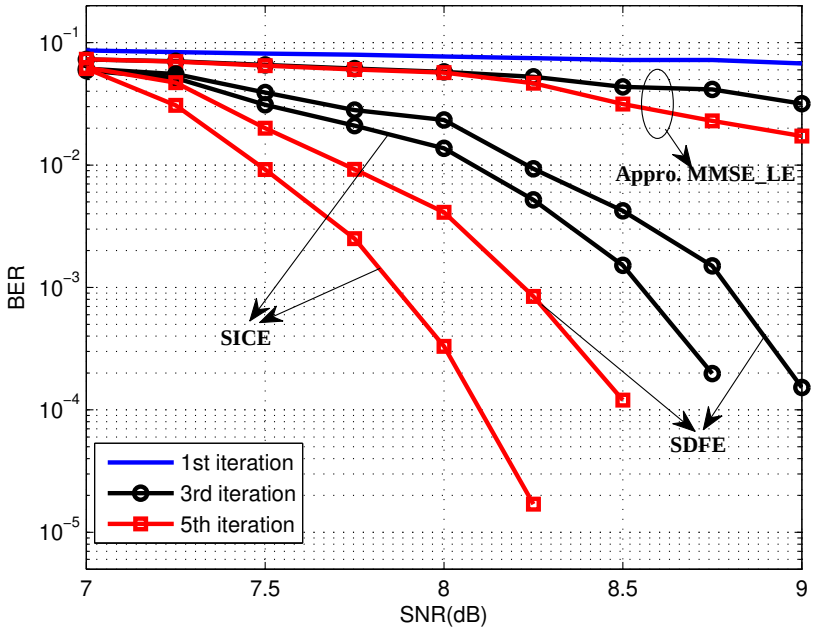

Figure 6.4. QPSK BER performance with LDPC code.

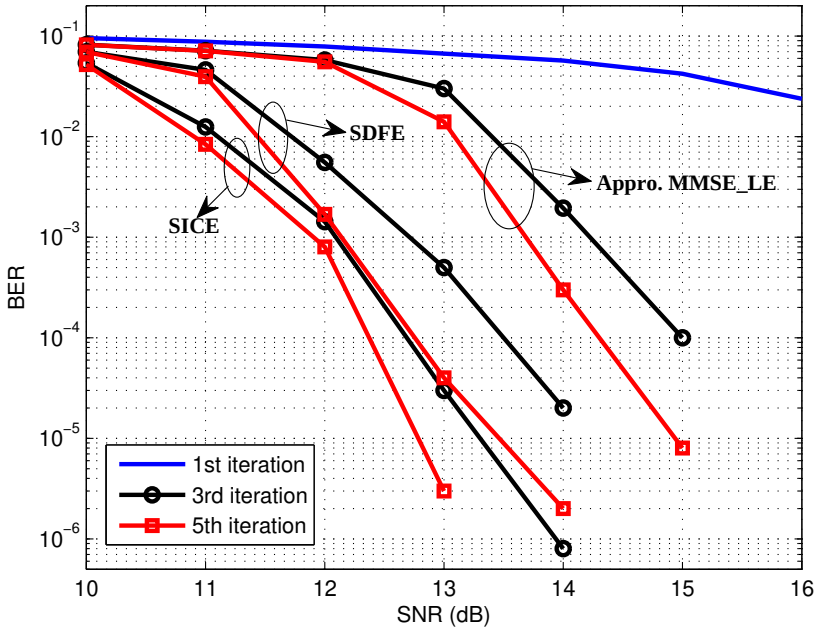

Figure 6.5. 8PSK BER performance with LDPC code.

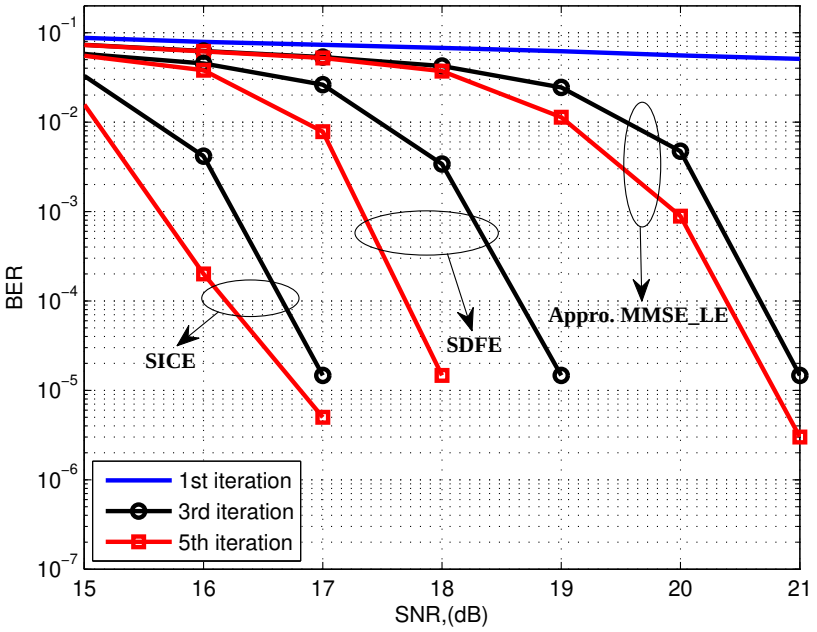

Figure 6.6. 16QAM BER performance with LDPC code.

7 CONCLUSIONS

A soft interference cancelation equalizer has been proposed for turbo equalization of MIMO systems operating in time dispersive channels. The soft interference cancelation was achieved by subtracting soft decisions of both causal and anti-causal interfering symbols. The soft decisions of the anti-causal symbols were obtained by using the *a priori* input at the SICE, and those of the causal symbols were calculated by combining the *a priori* soft input with the extrinsic output of the equalizer. The time-invariant feedforward and feedback filters of the SICE were developed by analyzing the first and second order statistics of the soft decisions. It has been demonstrated through both EXIT chart analysis and computer simulations that the anti-causal soft decisions are critical to the equalizer performance. Due to the inclusion of the anti-causal soft decisions, the proposed SICE achieved considerable performance gains over the MMSE-LE and SDFE, in terms of both convergence speed and BER. The EXIT chart analysis demonstrated that the SICE performance could approach the matched filter bound with ideal *a priori* input, yet the performance of SDFE is severely limited by the interference from the anti-causal symbols regardless of the quality of the soft input or the number of iterations.

ACKNOWLEDGMENT

The authors are grateful to Dr. Huang Lou for helpful discussions.

8 REFERENCES

[1] T. Abe, S. Tomisato, and T. Matsumoto, "A MIMO turbo equalizer for frequency-selective channels with unknown interference," *IEEE Trans. Veh. Technol.*, vol. 52, pp. 476-482, May. 2003.

[2] M. T*ü*chler, A. C. Singer, and R. Koetter, "Minimum mean square error equalization using a priori information," in *IEEE Trans. Signal Processing*, vol.50, pp.673-683, Mar. 2002.

[3] M. T*ü*chler, R. Koetter, and A. C. Singer, "Turbo equalization: Principles and new results," *IEEE Trans. Commun*, vol. 50, pp.754-767, May. 2002.

[4] A. Dejonghe and L. Vanderdorpe, "Turob equalization for multilevel modulation: An efficient low-complexity scheme," in *Proc. IEEE Int. Conf. Commun.*, vol.3, pp.1863-1867, 2002.

[5] D. Williamson, R. A. Kennedy, and G. W. Pulford, "Block decision feedback equalization," IEEE Trans. Commun., vol. 40, pp. 255-264, Feb., 1992.

[6] Z. Wu and J. Cioffi, "Low complexity iterative decoding with Decision-Aided Equalization for magnetic recording channels," *IEEE J. Select. Areas Commun.*, vol.19, pp.699-708, Apr. 2001.

[7] J. Wu and Y. R. Zheng, "Low complexity soft-input soft-output block decision feedback equalization," *IEEE J. Select. Areas Commun.*, vol. 26, pp.281-289, Feb. 2008.

[8] R. R. Lopes and J. R. Barry, "The soft-feedback equalizer for turbo equalization of highly dispersive channels," *IEEE Trans. Commun*, vol.54, pp. 783-788, Jan. 2006.

[9] H. Lou and C. Xiao, "Soft-decision feedback trubo equalization for multilevel modulations," *IEEE Trans. Signal Processing*, vol.59, pp. 186-195, Jan. 2011.

[10] A. Rafati, H. Lou, and C. Xiao, "Low-complexity soft-decision feedback turbo equalization for MIMO systems with multilevel modulations," *IEEE Trans. Veh. Technol.*, vol. 60, pp. 3218-3227, Sept. 2011.

[11] J. Tao, J. Wu, and Y. R. Zheng, "Reliability-based turbo detection," *IEEE Trans. Wireless Commun.*, vol. 10, pp. 2352-2361, July 2011.

[12] M. Tuchler and J. Hagenauer, "Turbo equalization using frequency domain equalizers, in *Proc. Allerton Conf.*, Monticello, IL, pp. 12341243, Oct. 2000.

[13] K. Kansanen and T. Matsumoto, "An analytical method for MMSE MIMO turbo equalizer EXIT chart computation," *IEEE Trans. Wireless Commun.*, vol. 6, pp. 59-63, Jan. 2007.

[14] , D. Falconer, S. L. Ariyavisitakul, A. Benyamin-Seeyar, and B. Eidson, "Frequency domain equalization for single-carrier broadband wireless systems," *IEEE Commun. Mag.*, pp. 58-66, Apr. 2002.

[15] P. Vila *et al.*, "Reduced-complexity M-ary decoders for turbo-equalization," in *2nd Int. Symb. Turbo Codes and Related Topics*, Brest, France, Sept.4-7, 2000.

[16] C. Berrou, "Near optimum error correcting coding and decoding:Turbo codes," *IEEE Trans. Commun*, vol. 44, pp.1261-1271, Oct. 1996.

[17] J. Hagenauer, "The turbo principle: tutorial introduction and state of the art," in *Proc. Int. Symp. Turbo Codeds and Related Topics,*, Brest, France, pp. 1-11, Sept. 1997.

[18] C. Douillard, M. J*ézé*quel, C. Berrou, A. Picart, P. Didier, and A. Glavieux, "Iterative correction of intersymbol interference: Turbo-equalization," *Eur. Trans. Telecommun.,* vol. 6, pp. 507-511, Sept.-Oct. 1995.

[19] L.R. Bahl, J. Cocke, F. Jelinek, and J. Raviv, "Optimal decoding of linear codes for minimizing symbol error rate," IEEE Trans. Inform. Theory, vol. IT-20, pp. 284-287, Mar. 1974.

[20] S ten Brink "Convergence behavior of iteratively decoded parallel concatenated codes", *IEEE Trans. Commun.,* vol.49, pp. 1727-1737, Oct. 2001.

[21] J. Proakis "Digital Communications", 3rd ed. Singapore: McGraw-Hill, 1995.

[22] W. E. Ryan, "An introduction to LDPC Codes", in *CRC handbook for Coding and Signal Processing for Magnetic Recording Systems* (B. Vasic and E. M. Kurtas, ed.), Ch36, CRC Press, Boca Raton, FL, 2004.

[23] https://sites.google.com/site/bsnugroho/ldpc May,1,2013

SECTION

2 CONCLUSIONS

This dissertation investigates turbo equalization with multiple-input multiple-output (MIMO) fading channels for radio frequency and underwater acoustic communications in both frequency domain and time domain. With the aid of zero padding (ZP) or cyclic prefix (CP) inserted between consecutive data blocks, a low complexity frequency domain turbo equalization is first proposed for MIMO systems and its performance is tested by processing the collected data in real-world UWA communications experiments.

On the other hand, high speed communication system demands efficient spectrum usage and power consumption. CP or ZP is not transmitted as auxiliary information, which in turn introduces the inter-block interference (IBI). We proposed an IBI cancelation and CP reconstruction algorithm to re-arrange the channel matrix into a block diagonal one. The modified FDTE can effectively detects continuous data stream for high speed UWA communications, and the results from the UWA communications experiments has verified its performance in terms of bit error rate (BER) and convergence speed.

In the time domain, a low complexity soft interference cancelation (SIC) turbo equalization for MIMO systems with high level modulation is proposed. The extrinsic information transfer (EXIT) chart has demonstrated the proposed SIC turbo equalizer can theoretically reach the bound set by the ideal matched filter, while the conventional linear or nonlinear turbo equalizers cannot reach. Also, the Monte Carlo simulations has shown that SIC turbo equalizer achieves a lower error floor as well as a more rapid convergence speed comparing with conventional turbo equalizers.

3 PUBLICATIONS

[1] J. Wu, L. Wang and C. Xiao, , "Low Complexity Soft-Interference Cancelation Turbo Equalization for MIMO Systems with Multilevel Modulations," submitted to *IEEE Trans. Veh. Technol.*.

[2] L. Wang, J. Tao, C. Xiao and T. C. Yang, "Low-complexity turbo detection for single-carrier low-density parity check-coded multiple-input multiple-output underwater acoustic communications," *Wireless Communications and Mobile Computing*, vol. 13, pp. 439-450 March 2013.

[3] J. Wu, L. Wang and C. Xiao, "Low Complexity Soft-Interference cancellation Turbo Equalization for MIMO Systems with Multilevel Modulations," accepted by *IEEE Global Commun. Conf. (Globecom)*, Atlanta, GA, USA, Dec. 2013.

[4] L. Wang, J. Tao and Y. R. Zheng, "Single-carrier frequency-domain turbo equalization without cyclic prefix or zero padding for underwater acoustic communications", *J. Acout. Soc. Am.*, vol. 132, pp. 3809-3817, 2012.

[5] L. Wang, J. Tao and Y. R. Zheng, 'Frequency-domain turbo equalization with No-CP for Single-Carrier MIMO Underwater Acoustic Communications", accepted by *MTS/IEEE Oceans 2011*, Kona, Hawaii, Sept., 2011.

[6] L. Wang, J. Tao, C. Xiao and T. C. Yang, "Frequency-domain turbo detection for LDPC-coded single-carrier MIMO Underwater Acoustic Communications," accepted by *MTS/IEEE Oceans 2010*, Seattle, WA, Sept., 2010

REFERENCES

[1] G. J. Foschini and M. J. Gans, "On limits of wireless communications in a fading environment when using multiple antennas," *Wireless Personal Commun.*, vol. 6, pp.311-335, 1998.

[2] J. Proakis, Digital Communications, 4th ed., McGraw-Hill, 2000

[3] S. Haykin, Communications Systems, 3nd ed., New York: Wiley, 1994.

[4] C. Douillard et al., "Iterative correction of intersymbol interference: Turbo Equalization," *European Trans. Telcomm.*, vol.6, pp.507-511, Sept.-Oct. 1995.

[5] M. Tchler, A. C. Singer, and R. Koetter, "Minimum mean squared error equalization using a priori information," *IEEE Trans. Signal Process.*, vol. 50, pp.673-683, Mar. 2002.

[6] M. Tchler, R. Koetter, and A. C. Singer, "Turbo equalization: Principles and new results," *IEEE Trans. Commun.*, vol.50, no. 5, pp. 754-767, Mar. 2006.

[7] R. R. Lopes, and J. R. Barry, "The soft-feedback equalizer for turbo equalization of highly dispersive channels," *IEEE Trans. Commun.*, vol.54, no. 5, pp. 783-788, Mar. 2006.

VITA

Longbao Wang was born July 28, 1986. He received his B.S degree in Electronics and Information Engineering from Huazhong University of Science and Technology, China, in 2009. He began his Ph.D study in August 2009 at the Department of Electrical and Computer Engineering at Missouri University of Science and Technology (formerly: University of Missouri-Rolla), USA. His research interests include turbo equalization, wireless communications and signal processing. He is expected to receive his Ph.D. degree in Electrical Engineering from Missouri University of Science and Technology in May 2014.